NORTHWESTERN UNIVERSITY

The Hertz-VPM Polarimeter and Applications of Multiwavelength
Polarimetry

A DISSERTATION

SUBMITTED TO THE GRADUATE SCHOOL
IN PARTIAL FULFILLMENT OF THE REQUIREMENTS

for the degree

DOCTOR OF PHILOSOPHY

Field of Physics and Astronomy

By

Megan M. Krejny

EVANSTON, ILLINOIS

December 2008

ABSTRACT

The Hertz-VPM Polarimeter and Applications of Multiwavelength Polarimetry

Megan M. Krejny

We present initial results from Hertz/VPM, the first submillimeter polarimeter employing the dual Variable-delay Polarization Modulator (dual-VPM). This device differs from previously used polarization modulators in that it operates in translation rather than mechanical rotation. We discuss the basic theory behind this device, and its potential advantages over the commonly used half wave plate (HWP). The dual-VPM was tested both at the Submillimeter Telescope Observatory (SMTO) and in the lab. In each case we present a detailed description of the setup. We discovered that properties of the VPM wire grids (diameter and spacing) caused behavior that differs from theoretical predictions for ideal wire grid performance. Modifying the polarimeter settings to compensate for this behavior, we found that the dual-VPM system is robust, operating with high efficiency and low instrumental polarization. This device is well suited for air and space-borne applications, and is also advantageous for multi-wavelength polarimetry applications.

One such application concerns submillimeter spectropolarimetry of T Tauri Star (TTS) disks, to probe the grains in this environment. We present $350\,\mu$m polarimetry of the

circumstellar disk of DG Tau. Comparison with a previous measurement made at $850\,\mu$m suggests that there is considerable structure in the submillimeter polarization spectrum. We also discuss theoretical models for polarized emission from TTS disks, both simple toy models developed at Northwestern and a more sophisticated model published more recently by J. Cho and A. Lazarian. The data do not agree with this more recent model, but it is plausible that this could be due to the larger mass of the DG Tau disk in comparison to the model disk.

Acknowledgements

This thesis is the culmination of seven years of hard work, not only from myself, but also of my collaborators. First, I wish to thank the SHARP collaboration, which includes Roger Hildebrand, Larry Kirby, Michael Attard, Martin Houde, Darren Dowell, Hiroko Shinnaga, Jaqueline Davidson, John Vaillancourt, and Lerothodi Leeuw. I appreciate their assistance in data collection and analysis, and I am proud to have worked alongside them to maintain and operate SHARP at the CSO.

Likewise, many people were involved in the design, construction and testing of the Hertz/VPM polarimeter. I thank Chris Walker and his group at the University of Arizona (Christian d'Aubigny, Craig Kulesa, and Dathon Golish) for the optics bench design and access to the SMTO. At NASA/GSFC, George Voellmer, Mike Jackson, and Harvey Moseley were primarily responsible for the design and construction of the VPMs, and Ed Wollack contributed significantly to the E/M analysis of the device. Bob Loewenstein proved invaluable as our Hertz data acquisition software guru. To see everything come together (and work with relatively minor incident) in such a short time was truly remarkable and set a standard of excellence that I hope to repeat in the future.

I am happy to have met many excellent graduate students and postdocs at Northwestern. I thank Tristan Matthews for both his data analysis of DG Tau and the many shifts he pulled during operation of the Hertz/VPM at Northwestern. Hua-bai Li was not only responsible for the design of the SHARP instrument, but also is a good friend and

colleague. And, I appreciated his instruction in Chinese (xie xie ni). I wish to thank all of my officemates for both the insightful physics discussions and the fun social atmosphere that I have experienced. I thank Lou Jisonna, Dave Joffe, and Ismail Uman for their moral support, especially during my first two years of school. And special thanks to Soko Matsumura for her help writing the section on planet formation.

I also wish to thank some of the people I met while a student at Ohio University. To Victoria Soghomonian, for her guidance as my advisor and camaraderie as a fellow woman in physics, and to David Drabold for his encouragement to pursue a graduate degree. Thanks to Dave Jordan, a fellow physicist who has served as a friend and mentor since my time working at TRIUMF. I also wish to thank Arthur Smith; my one summer working in his lab was the foundation of my love of instrumentation.

I wish to especially thank David Chuss for his guidance and supervision, both as a fellow graduate student and as my advisor at NASA/GSFC. From helping me with homework during my first year courses to coauthoring with me on my first refereed publication, Dave has been not only a knowledgeable colleague, but one who gives generously of his time and friendship.

No graduate student can exist without an advisor, and I was very lucky to have Giles Novak as mine. He has instructed me how to be a good instrumentalist, has instilled in me a love and pride for my work, and continues to instruct me in the art of patience (which I hope to master someday). Giles has welcomed me into his family, both professionally and personally. For this and much more, I am extremely grateful.

During my time in Chicago, I have made many friends who have provided endless encouragement as I pursued my PhD. Thanks to Derek Wu, who saw me through the

various ups and downs of graduate school, and to David Foster, for keeping me focused in my final year of preparations. Thanks to Jen Fleming, Kerry Greminger and Joe Langman for cheering me on throughout the process. I especially wish to thank Liz and Joe Mason, not only for their constant friendship, but also for showing me through example that laughter is always possible, even when circumstances appear otherwise.

Finally, I thank my family for their continuous love and support. I thank Michele for nurturing my budding interest in astronomy with numerous trips to public observing nights in the park, and never letting me give up on my dreams. I thank my sister Meredith, who, perhaps without knowing it, motivated me to strive for excellence in all that I do. Most of all, I thank my parents Bill and Eileen, for letting me choose my own path in life, and supporting me no matter where that path may lead.

Table of Contents

List of Tables

List of Figures

CHAPTER 1

Introduction

It has been almost 60 years since the discovery of the polarization of starlight by magnetically aligned dust grains (Hiltner, 1949; Hall, 1949; Chandrasekhar & Fermi, 1953). Since then, astronomical polarimetry has become a valuable and well-established tool to study a wide variety of astrophysical sources, from nearby star-forming regions to the radiation linked to the formation of our universe. Polarized submillimeter and FIR light from thermally emitting aligned dust grains, both in the interstellar medium (ISM) and around stars, allows us to map the plane-of-sky magnetic field in these regions (Cudlip et al., 1982; Hildebrand et al., 1984). In star-forming regions, light along the line of sight is emitted by dust grains at different temperatures; to separate cooler dust contributions from the warmer dust, e.g., near protostars, observations at multiple wavelengths are required. At radio wavelengths, polarized light has allowed us to view the central engines of active galactic nuclei. Astronomical polarimetry is also of great interest in cosmology. Measuring the polarization of the CMB could provide an opportunity to study the universe during its first $\sim 10^{-32}$ seconds after the Big Bang, when the universe is thought to have gone through an inflationary epoch at an energy scale $\sim$12 orders of magnitude above those accessible to terrestrial particle accelerators.

Observations of star forming regions require study of radiation in the far infrared through millimeter wavelengths. For these regions, the dust grains are small ($< 1\,\mu$m), and polarized light is created by magnetically aligned, thermally emitting dust grains. The

magnetic field maps created provide clues to whether magnetic field support is significant in preventing star collapse.

Another topic of interest is to learn what happens at later stages; that is, how planets form in protostellar disks. We believe that the first step in planet formation is coagulation of dust grains in the disk. In the past two decades, surveys have been compiled of T Tauri Stars, protostars denoted for their large infrared excesses due to surrounding dust disks. Plotting the spectral energy distributions (SEDs) of these disks and looking at the slope of the curve at submillimeter and millimeter wavelengths has provided strong evidence for the existence of large grains. However, fits to the spectra that determine grain size are based on models with inherent degeneracies.

Since submillimeter polarization of astronomical objects was first measured almost three decades ago, the field has benefited substantially from increasing telescope size, larger arrays, and increased optical efficiency. In addition, decreases in bolometer noise have, for the past decade, allowed us to obtain levels that are below the "photon noise" of sky emission. These improvements allow astronomers to pursue ambitious observing programs of faint objects, including those related to star and planet formation.

In Part 3 of this thesis, we describe a new method of probing protoplanetary disks, by studying the shape of the polarization spectrum for a TTS circumstellar disk in the submillimeter waveband. We will first explain (Part 1) some theoretical ideas regarding the behavior of dust grains, both with respect to their method of alignment and with respect to the manner in which they can cause polarization. In Part 3 we present models of predicted dust grain polarization in T Tauri Star disks, both preliminary toy models developed at Northwestern and more sophisticated radiation transfer models developed by

our collaborators. We compare these with submillimeter polarimetric observations of DG Tau, a bright, young, and well-studied TTS. Polarization of DG Tau was previously observed at $850\,\mu$m (Tamura et al., 1999), and here we present the first $350\,\mu$m polarimetry of DG Tau, obtained using Northwestern's SHARP polarimeter at the Caltech Submillimeter Observatory (CSO) on Mauna Kea.

Whether observing star-forming regions or remnants of the early universe one faces the same primary challenge: measuring polarized fluxes that are 10^{-6} or less of the total incident flux. For star-forming dust and gas clouds, polarizations are often of order 10^{-2} of the total source flux, but very small (10^{-6}) compared to the atmospheric flux (for ground-based observations).

Measuring a small polarized signal in the presence of a large, unpolarized background is challenging. Noise from the background as well as time variations in the instrument and observing environment dominate the signal. Polarization modulation allows for encoding of the polarization signal, enabling a subsequent extraction of the signal from the more random data stream.

In Part 2 of this thesis, we describe the implementation of a novel polarization modulator, the dual Variable-delay Polarization Modulator, or dual-VPM. The dual-VPM operates in reflection instead of transmission, and fully modulates the linear polarization state using only small translational motions. These properties make the dual-VPM an attractive alternative to the conventional birefringent half wave plate (HWP) modulator for certain applications. We review the basic theory behind the dual-VPM and describe the development and characterization of this device.

We used Hertz, a polarimeter previously operated at the CSO, as a dual-polarization detector for our new dual-VPM polarimeter. This polarimeter, named "Hertz/VPM", was tested at $350\,\mu$m at the Submillimeter Telescope Observatory (SMTO), where we characterized the performance of the VPMs. Follow-up data were later collected at Northwestern University, and we present results from both sets of tests in Part 2.

Part 1

Preliminaries

We begin with a series of topics related to astrophysical polarimetry which will be useful for later parts of this thesis. We first discuss Stokes Parameters (Chapter 2), which are commonly used in polarimetry. In Chapter 3, we discuss the basic properties of star and planet formation. Later, in Chapter 4, we turn our attention to dust grains and polarized light, including polarization mechanisms and grain alignment. Finally, in Chapter 5, we look at basic data acquisition techniques for single-dish/bolometer systems; we conclude with an example which is relevant to our data collection, the SHARP polarimeter at the Caltech Submillimeter Observatory (CSO).

CHAPTER 2

Stokes Parameters

Full characterization of electromagnetic radiation requires knowledge of its amplitude and phase. For most astronomical observations (i.e., not obtained via interferometry), we are only able to measure radiation intensity. Therefore, it is necessary to devise a way to determine the original polarization state of the observed light from only intensity measurements. We are able to accomplish this through the use of *Stokes Parameters*. We will now define these parameters, following the convention of Jackson (1999).

2.1. Definition of Stokes Parameters

We start with a monochromatic plane wave (frequency ω), propagating in the direction $\mathbf{k} = k\hat{\mathbf{z}}$. The wave has an arbitrary polarization that can be broken into two linearly independent components that lie along the two other axes of an orthogonal basis ($\hat{\mathbf{x}}$, $\hat{\mathbf{y}}$, $\hat{\mathbf{z}}$):

(2.1)
$$\mathbf{E}(\mathbf{r}, t) = (E_x\hat{\mathbf{x}} + E_y\hat{\mathbf{y}})e^{i\mathbf{k}\cdot\mathbf{r}-i\omega t}$$

E_x and E_y are the complex amplitude components (i.e., they contain magnitude and phase information) in each direction. The complex coefficients E_x and E_y are defined as:

$$(2.2) \qquad\qquad\qquad E_x = a_x e^{i\delta_x}$$

$$(2.3) \qquad\qquad\qquad E_y = a_y e^{i\delta_y}$$

By this representation, the phase difference between E_x and E_y will determine the type of polarization. For example, if E_x and E_y have the same phase ($\delta_x - \delta_y = 0$), then the light is linearly polarized at an angle $\theta = \tan^{-1}(E_y/E_x)$ measured from the $\hat{\mathbf{x}}$ axis and a magnitude $\sqrt{E_x^2 + E_y^2}$. If E_x and E_y are out of phase, however, then the light is elliptically polarized. (Circularly polarized light is a special case of the latter, where $E_1 = E_2$ and $\delta_1 - \delta_2 = \frac{\pi}{2}$.)

For a linear polarization basis orthogonal to the direction of propagation, we define the Stokes Parameters (Jackson, 1999) to be:

$$(2.4) \qquad\qquad I = \mid \hat{\mathbf{x}} \cdot \mathbf{E} \mid^2 + \mid \hat{\mathbf{y}} \cdot \mathbf{E} \mid^2 = a_x^2 + a_y^2$$

$$(2.5) \qquad\qquad Q = \mid \hat{\mathbf{x}} \cdot \mathbf{E} \mid^2 - \mid \hat{\mathbf{y}} \cdot \mathbf{E} \mid^2 = a_x^2 - a_y^2$$

$$(2.6) \qquad U = 2Re[(\hat{\mathbf{x}} \cdot \mathbf{E}) * (\hat{\mathbf{y}} \cdot \mathbf{E})] = 2a_x a_y cos(\delta_y - \delta_x)$$

$$(2.7) \qquad V = 2Im[(\hat{\mathbf{x}} \cdot \mathbf{E}) * (\hat{\mathbf{y}} \cdot \mathbf{E})] = 2a_x a_y sin(\delta_y - \delta_x)$$

Here, I denotes the intensity of the wave. If we set our coordinate axes so that $\hat{\mathbf{x}}$ is the horizontal axis and $\hat{\mathbf{y}}$ is the vertical axis, we see that Q refers to the preponderance of horizontal polarization over vertical polarization. U and V give linear basis phase information, with U referring to how much "in phase" and V referring to how much "out of phase" the two polarization components are.

For example, consider the case where $Q = 0$. If the horizontal and vertical components are in phase, then U will be large and V will be small, and we have polarization that is oriented either +45 or -45° relative to the polarization axes; thus, U is said to be the preponderance of polarization with orientation of +45° over polarization at -45°. (By this convention for Q and U, the angle of polarization is defined to increase counterclockwise from the horizontal.) However, if the horizontal and vertical components are out of phase, then V will be large. V is a measure of circular polarization; it is the preponderance of right circular polarization (RCP) over left circular polarization (LCP). (This is suggested by the fact that V is a maximum when $\delta_x - \delta_y = \frac{\pi}{2}$, which, as stated before, denotes circular polarization.)

The incoming radiation is not fully coherent and varies in time. Thus, actual source measurements are denoted by the time averages of Equations 2.4–2.7.

The choice of basis ($\hat{\mathbf{x}}$, $\hat{\mathbf{y}}$, $\hat{\mathbf{z}}$) is arbitrary, as is the labeling of axes. For polarimetric measurements, the axes are often determined by the positioning of a wire grid, which separates light incident on the detector into orthogonal components. This can be referred to as the orthogonal components reflected (R) and transmitted (T), or, depending on the orientation or notation of the optical system, horizontal (H) and vertical (V).

2.2. The Poincare Sphere

The Poincare Sphere is a graphical representation of Stokes Parameters. The x, y, and z axes correspond to the parameters Q, U, and V, respectively (but they are not to be confused with the basis that describes the plane wave of the previous section). The radius of the sphere is the total intensity; the four quantities are related by:

$$(2.8) \qquad\qquad I^2 \geq Q^2 + U^2 + V^2,$$

where equality holds for fully polarized light. Completely polarized light lies on the surface of the Poincare sphere, while points that lie in the interior represent partially polarized light. Points representing linearly polarized light lie in the QU plane. We define the normalized Stokes Parameters as $q = Q/I$, $u = U/I$, and $v = V/I$. Dividing both sides of Equation 2.8 by I^2 gives us the equation of a unit sphere in terms of these normalized Stokes Parameters.
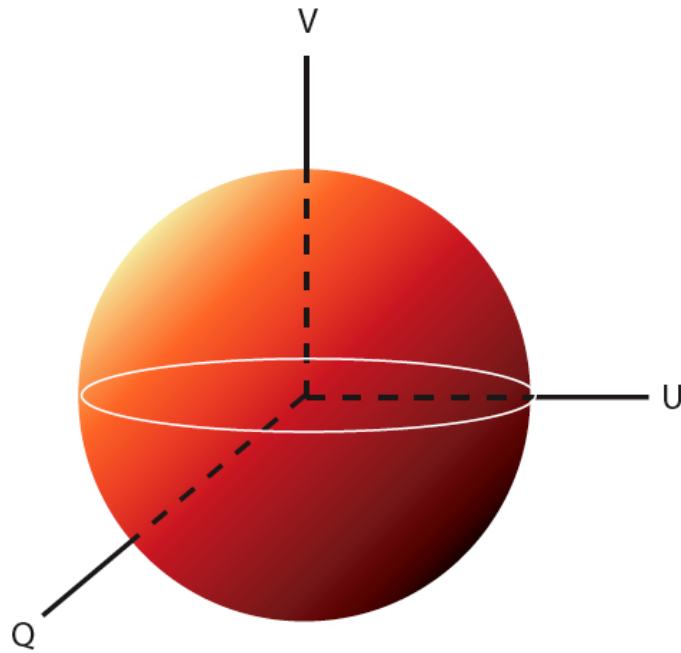
Figure 2.1. The Poincare Sphere. The Poincare sphere allows for graphical representation of Stokes parameters. Q, U, and V are the three axes, with $I^2 \geq Q^2 + U^2 + V^2$. Points on the surface of the sphere denote fully polarized light, while points inside denote partial polarization. Points lying in the QU plane represent linear polarization.

CHAPTER 3

Star and Planet Formation

Star formation occurs in interstellar molecular clouds. In regions of relatively higher density, atoms and molecules begin to attract via gravity, eventually resulting in a dynamical collapse to form a protostar. Protostars are very bright due to the high kinetic energy of the accreting material (this energy is released upon impact with the protostar), yet they are not visible at optical wavelengths due to extinction by the surrounding dust. Accretion continues in a protostar as its temperature and density rise, until nuclear fusion is able to balance gravity, and the star enters the main sequence.

In the following, we will describe properties of molecular clouds, the home of stellar nurseries. Then we shall look at the process of how stars and their surrounding protostellar disks form within a molecular cloud. We conclude with a summary of planet formation in circumstellar disks.

3.1. The Interstellar Medium

The interstellar medium is dominated by a combination of warm, low density hydrogen gas in its neutral atomic state (HI), warmer and even less dense ionized hydrogen (HII), and cooler, higher density molecular hydrogen (H_2) (Carroll & Ostlie, 1996). Hydrogen density in the ISM averages around 1 particle cm^{-3} (Spitzer, 1978), but with very large variations. In addition to hydrogen, other elements exist in the form of gas, with helium

being the next abundant (comprising ~20% of the gas), and relatively sparse amounts of oxygen, nitrogen, and various other elements and compounds.

Compared to hydrogen, dust is far less abundant in the ISM, with densities of only $100 \, \text{particles km}^{-3}$ (Karttunen et al., 1996). These particles are thought to exist mostly as graphite, silicates, and ice (Carroll & Ostlie, 1996; Spitzer, 1978; Karttunen et al., 1996) and typically have radii of less than $0.25 \, \mu\text{m}$ in the ISM. The dust to gas mass ratio in the ISM is roughly 0.01 (Spitzer, 1978).

3.2. Magnetic Fields and Turbulence in Molecular Clouds

Stars are formed within giant molecular clouds, which contain numerous smaller clumps of masses 10^3-$10^4 \, M_\odot$, radii 2-5 pc, and temperatures around 10 K. These clumps contain molecular cloud cores, some with protostars of various developmental stages detected as infrared sources (Shu et al., 1987).

For an average clump in the cloud, its associated critical mass needed for collapse, or Jeans mass, is only a few solar masses, which is much smaller than the mass of the clump itself (Shu et al., 1987). This implies large star formation rates; however, these rates are not actually observed. Thus, other forces must contribute to sustaining the cloud from collapse, thereby slowing the star formation rate. There are two phenomena that are considered possible sources of cloud support: magnetic fields and turbulence.

The magnetic field is closely tied to the gas present in the cloud. The Lorentz force causes moving ionized particles to spiral around magnetic field lines. The magnetic field also indirectly determines the flow of neutral particles in the cloud, due to their collisional coupling to the ionized particles. Depending on the strength of the magnetic field, motion

of particles perpendicular to the field lines can be greatly suppressed. Just as the motion of particles in a magnetic field is tied to the field, magnetohydrodynamic theory states that a perfectly conducting plasma requires a constant ratio of magnetic flux to column density. This "flux freezing" means that the magnetic field, in turn, moves with the particles in the cloud.

We now consider magnetic fields and flux freezing during star formation. As a gas cloud starts to gravitationally collapse, the neutral particles are slowed down, as they collide with the magnetically coupled ionized particles. This greatly slows, but does not stop, gravitational collapse. As infall continues, the magnetic field is slowly dragged in by the infalling gas. This pulls the field lines closer together; the resulting increase in magnetic energy density causes greater forces on the ionized particles, which in turn leads to higher collisional coupling with the neutral gas. In this way the magnetic field opposes the collapse of the star, and causes the star formation rate to drop dramatically.

Turbulence, on the other hand, causes a decrease in star formation rates on large spatial scales. Turbulence results in clouds forming and dispersing quickly. Since these cloud formation and destruction times are so short, only a few clouds can grow to sufficient sizes quickly enough to become self-gravitating (Crutcher, 2004).

There is much debate over which process is the more likely cause for the low star formation rates that we observe. Shu et al. (1987) argue that magnetic fields are the primary mechanism, due mainly to the dissipative nature of turbulent motion. Others insist that magnetic fields are too weak to prevent collapse, while still others such as Crutcher (2004) believe that turbulence and magnetic fields are equally important. Modeling and observations have been used to try to determine which is the dominant force, with evidence

supporting either side. In actuality, both phenomena probably play important roles in star formation, although further study is needed to provide a definitive answer.

3.3. Stages of Star Formation

The basic star formation process can be divided into four stages, each designated by a class number; Figure 3.1 illustrates the process. First, a clump in the molecular cloud starts to collapse under gravity. In the presence of a small initial spin, the clump rotates faster as the matter falls in to the core. Because of this, some of the infall material does not fall directly onto the central protostar; instead, it misses the star and falls towards the midplane. This effect creates a circumstellar disk of dust and gas. These dense systems, consisting of the protostar, its accretion envelope, and circumstellar disk, are designated as Class 0 objects. These objects are not visible at optical wavelengths due to the large amount of dust that surrounds the central star. Plots of their spectral energy densities (SEDs) show peaks in the far-infrared, corresponding to blackbody emission with $T = 15\text{-}30\,\text{K}$ (Cernicharo et al., 2000). Due to the high obscuration, Class 0 objects have only been observed at $\lambda > 25\,\mu\text{m}$. Violent ejecta in the form of large molecular and/or ionic outflows are a byproduct of the accretion, and act to help remove excess angular momentum in the system (Testi et al., 2002).

Class I objects are still fed by accretion, but have a smaller envelope and lower ejection rates than that of a class 0 protostar. The star and accretion disk are still embedded in an accretion envelope. Class I objects have SEDs that rise between 2 and $10\,\mu\text{m}$, peaking in the mid-IR (Stahler, 1991), and dropping off at longer wavelengths.

At a certain point in the evolutionary process, the accretion envelope (and ejecta) are greatly diminished, and the protostar is now visible at optical wavelengths. These class II objects, which include T Tauri Stars (TTSs), still retain their circumstellar disks. As a result, these objects often show an infrared excess caused by the emission from the dust and gas disk. Class II protostars have SEDs that peak in the near-IR and decrease in the mid-IR.

The final stage in protostellar formation occurs when the protostellar wind finishes blowing away the surrounding accretion envelope. At this point, there is little or no circumstellar material left, and only a very small infrared excess. These pre-main-sequence stars are labeled Class III objects.

3.4. Stages of Planet Formation

Study of our own solar system naturally causes one to question how it came into existence, and likewise if planets similar to those in our solar system can form around other stars. Since the evolutionary timescales of a solar system are much longer than one can observe, we must piece together the steps of planet formation by observing systems at various stages of formation.

Current theories hold that planet formation occurs in three main stages, determined by the range of grain sizes present and the process of larger particle formation (Beckwith et al., 2000). First, small dust grains, less than $1\,\mu$m in size, coagulate through collisions to form larger particles, up to $10\,$cm in size. Next, the dust grains grow from tens of centimeters to kilometers via gravitational attraction (not random collisions). Once smaller planetesimals have formed (on the order of a few kilometers), the third and final stage
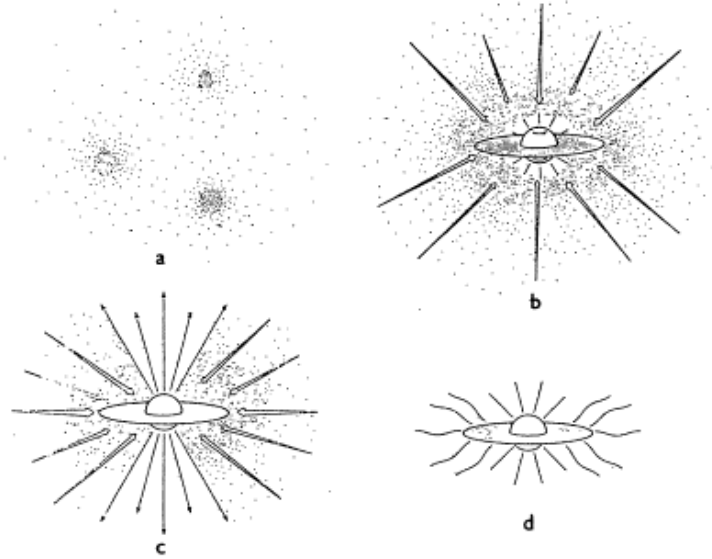
Figure 3.1. From Shu et al. (1987), stages of protostellar evolution. a) Relatively dense "core" forms within a molecular cloud. b) Free fall collapse results in a growing protostar with accretion disk and envelope. c) Protostellar wind blows away the surrounding accretion envelope. d) Protostar is now visible at optical wavelengths, and is surrounded by remaining circumstellar material, which eventually forms into planets.

occurs as the planetesimals grow to become protoplanets of $\sim 10^{-2}$ lunar mass (Thommes et al., 2003), and finally become either rocky, terrestrial planets or large gas giants. Figure 3.2 outlines this planet formation process (for the formation of a gas giant). We now describe each of these stages in more detail.

The start of planet formation begins with a disk of gas and dust, undergoing Keplerian rotation about the central star. Superposed on this organized motion is not only Brownian motion, but also turbulence in the disk. Dust randomly collides with other gas and dust; sometimes, dust particles collide and stick together (Natta et al., 2007). This aggregation continues until the dust grain becomes large enough to decouple its motion from the

collisions with the gas in the disk (Dominik et al., 2007). At this point, the dust starts to settle towards the midplane, a process referred to as *sedimentation*. As sedimentation occurs, dust grains are still aggregating. This process continues as dust particles grow up to the order $\sim 10\,\mathrm{cm}$ in size (Barrière-Fouchet et al., 2005). This first stage of planet formation is widely accepted, as there exists a wealth of compelling (albeit not definitive) observational evidence, as we shall see in section 10.2.

The second stage of planet formation requires grains to grow from centimeter-sized "pebbles" to large, kilometer-sized "boulders". However, the process to accomplish this cannot be a slow process of collisional aggregation and gravitational attraction. This is because, as a dust grain becomes large and starts to move relative to the surrounding gas it feels a relative "headwind" that slows the particle down. This causes the large grains to drift radially inward towards the star. In fact, large rocks on the order of $1\,\mathrm{m}$ should, in theory, all fall into the star, since they cannot grow to stable sizes ($\sim 1\,\mathrm{km}$) quickly enough (Weidenschilling, 1977). However, if that were to occur, there would be no planetesimal formation above this size.

It is not known for certain what supports growth up to $1\,\mathrm{km}$ in size. The prevailing theory (Youdin & Shu, 2002, and references therein) is based on gravitational instability, which states that, as particles settle to the midplane of the disk, the region builds to a high density, but with low temperature. If the temperature is low enough and the density high enough, a gravitational instability occurs that causes rapid accretion of grains onto larger particles. Model simulations (for example, Johansen et al., 2007) have been able to produce large objects on the order of kilometers by this process.
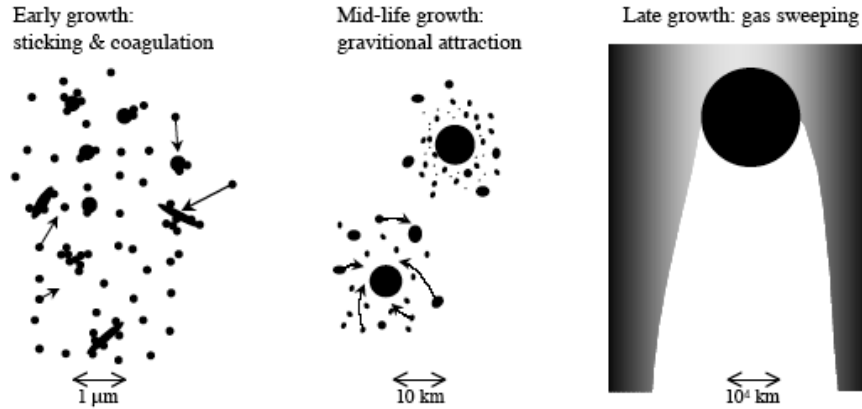
Figure 3.2. Three steps toward planet formation, taken from Beckwith et al. (2000). For each range of grain sizes, a different mechanism dominates grain/planetesimal growth. For the smallest grains (on the order of 0.1-100 μm), dust grains collisionally aggregate. As the grains grow larger (10 cm - 1 km), larger bodies are formed primarily by gravitational attraction. For large planetesimals (10^4 km), rocky cores form, then become gas giants. (This figure does not depict terrestrial planet formation.)

The final stage involves the growth of large planetesimals into protoplanets and then either a terrestrial planet or gas giant. This stage can actually be broken into smaller stages. First, *runaway growth* occurs when a smaller planetesimal collides with a larger one. If the velocity of the former is smaller than the escape velocity of the latter, then the two objects will stick together, making it a very fast protoplanet formation process (Wetherill & Stewart, 1989). However, this cannot continue indefinitely. As the protoplanet rapidly increases in size, it starts to influence the motion of surrounding planetesimals, and increases their random velocities. Thus, as the object grows larger, its collisional cross section decreases, causing a stage of slower *oligarchical growth* (Kokubo & Ida, 1998). Finally, the protoplanet either becomes a terrestrial planet or proceeds to become a gas giant. For gas giants, the rocky core begins to gravitationally attract gas

when the escape speed of the protoplanet becomes larger than the random speed of the gas (Lissauer & Stevenson, 2007). The protoplanet starts to "sweep out" a gap in the disk as it collects a large atmosphere.

As we shall discuss later in Part 3, we look to polarimetry for new observational evidence of the early stages of planet formation.

CHAPTER 4

Dust Grains and Polarized Light

In this chapter we discuss the different methods by which dust grains can cause polarization of light. Some of these polarization mechanisms require alignment of elongated grains by an external magnetic field, and for this reason we will also review the theory of magnetic grain alignment in this chapter.

4.1. Extinction, Emission, and Efficiencies

Dust grains interact with light through absorption, emission, and scattering. Dust grains absorb light (often optical light from parent stars) and reemit that light at longer wavelengths in the infrared, as dictated by their temperature. When light is scattered by dust grains, the direction of propagation is altered, resulting in an attenuation of the background source intensity.

To quantify the dimming effects of dust grains on incident light, we establish for each process an efficiency factor, $Q_{process}$. The efficiency can be interpreted as the deviation from a perfect absorber/emitter (i.e., a blackbody) or a perfect scatterer. The efficiency depends on the properties of the dust grains, such as size, shape, and composition, and the wavelength of incident light. By Kirchhoff's law, the absorption efficiency equals the emission efficiency.

If dust grains were perfect blackbodies, or perfect scatterers, the emission (or attenuation) of light would depend only on their geometric cross sectional area, A. However,

their deviation from ideal causes incident light rays (or light thermally emitted) to "see" a different cross section, or *optical cross section* $C_{process}$. The optical cross section is related to the geometric cross section A by:

$$(4.1) \qquad\qquad C_{process} = Q_{process}A$$

The term "extinction" refers to both scattering and absorption combined (van de Hulst, 1957). By conservation of energy, the total extinction cross section is:

$$(4.2) \qquad\qquad C_{ext} = C_{sca} + C_{abs}$$

The cross sections and efficiencies are used for modeling light propagation in protostellar environments, especially in star-forming clouds, and, as we shall see in Chapter 11, dusty protostellar disks. Thermal emission is distinct from extinction, and thus is not included in the equation above. However, as we stated above, Kirchhoff's Law states that the emissivity of a body must equal its absorptivity; thus, absorption and emission have the same efficiency.

4.2. Dust Grain Polarization Mechanisms

4.2.1. Polarization by Scattering

Light rays scattered by dust grains are redirected from their original trajectory to a new direction. Thus, when an observer views an object behind a scattering cloud, the total incident light detected by the observer is attenuated compared to the total flux emitted

by the background object in that direction. Scattering has an efficiency (Q_{sca}) that is dependent on both the grain composition and the relative sizes of the grain radius a and incident wavelength λ.

Mie scattering theory gives the solution for diffraction of a plane monochromatic wave by a homogeneous sphere of any size and any composition. Looking only at dependence on grain size, Mie theory gives the following rough approximations to the scattering efficiencies (Carroll & Ostlie, 1996):

$$
(4.3) \qquad Q_{sca} \sim
\begin{cases}
0 & \lambda \gg a \\
(a/\lambda) & \lambda \sim a \\
constant & \lambda \ll a
\end{cases}
$$

For $\lambda \gg a$, the above is only an approximation; a more accurate description is given by Rayleigh scattering, where, for small a, $Q_{sca} \sim (a/\lambda)^4$. As the equations show, dust grains scatter light more efficiently when the grain size is larger than the wavelength of the incident radiation.

We first consider what happens when polarized light is incident on a dust grain. The dust grain contains either numerous charged particles that are free to move along its surface, or bound charges that can oscillate about their lattice position. Either way, when polarized light is incident on the grain, the charges feel a force ($\mathbf{F} = q\mathbf{E}$) that causes them to oscillate along an axis parallel to the direction of polarization. The energy obtained from the light ray is then re-rediated by the electrons in a dipole radiation pattern. If we

view the grain along a line of sight parallel to the axis of this oscillation, we will see no radiation (Hecht, 1998).

We now consider the case of unpolarized incident light (Figure 4.1). Unpolarized light is equivalent to the superposition of many polarization states, as shown in the figure. Because of the existence of these states, viewing the dust grain at angles that are orthogonal to the direction of incident radiation will cause one component of polarization to be suppressed, as shown. Thus, light viewed at these angles is highly polarized, while forward scattered light remains unpolarized. The position angle of observed polarization is orthogonal to the plane of incidence. Polarization seen in reflection nebulae can be as high as tens of percent (for example Schmidt et al., 1978; Joyce & Simon, 1986; Yamashita et al., 1989).

4.2.2. Polarization by Selective Extinction

As seen in the previous section, polarization by scattering can occur regardless of grain geometry. In contrast, polarization by selective (or dichroic) extinction requires aligned, non-spherical grains. These grains are aligned by an external magnetic field such that the long axis of the grain is perpendicular to the magnetic field, as will be shown in Section 4.3.

Selective extinction can be attributed to selective absorption, selective scattering, or a combination of the two. Again, efficiencies are dependent on grain composition and grain size (a relative to λ, provided a is not much larger than λ). An elongated dust grain will have two extinction efficiencies, one for the long axis of the grain ($Q_{ext,l}$) and one for the short ($Q_{ext,s}$), with $Q_{ext,l}$ often larger than $Q_{ext,s}$. Thus, unpolarized light (split
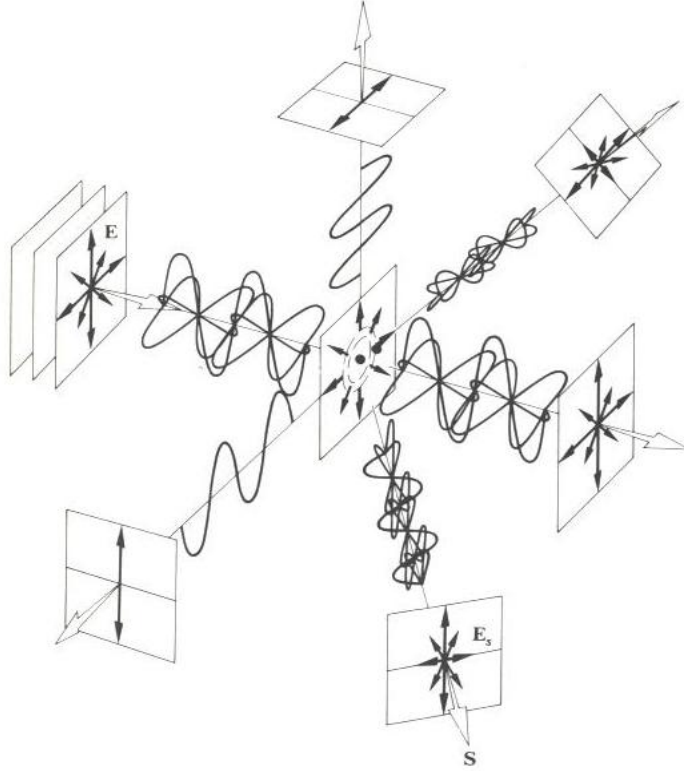
Figure 4.1. Schematic illustration of polarization by scattering, taken from Hecht (1998). Unpolarized light incident on a dust grain causes electrons to oscillate in various directions, all orthogonal to the direction of the incident ray. For viewing angles orthogonal to the direction of this ray, one component of polarization is suppressed, resulting in a net polarization.

into orthogonal components aligned with the grain axes) that is incident upon the dust grain will be attenuated (either scattered or absorbed) more along the long axis, while the component of light aligned with the short axis of the grain will have a higher intensity.

The percent polarization P for light is defined as (Spitzer, 1978):

$$(4.4) \qquad P = (I_{max} - I_{min})/(I_{max} + I_{min})$$

with I_{max}, I_{min} corresponding to light contributions from the short and long grain axes, respectively. Since the incident light is unpolarized, each orthogonal component of polarization is assumed to have one half of the total incident intensity. The intensity of each component that passes through the cloud and to the observer is given by $I = I_0 e^{-\tau_{ext}}$, where τ_{ext} is the extinction optical depth for that component. The optical depth is proportional to the optical cross section of the grains times the number density of the grains N and the length of the line of sight through the cloud L:

$$\tau_{ext} \propto C_{ext} N L.$$
(4.5)

A longer axis corresponds to a greater optical cross section, thus a larger optical depth corresponds to a smaller transmitted intensity (provided that the grains are not much larger than the wavelength). We thus substitute into Equation 4.4 to obtain (Hildebrand, 1988):

$$P_{ext} = \frac{e^{-\tau_{ext,s}} - e^{-\tau_{ext,l}}}{e^{-\tau_{ext,s}} + e^{-\tau_{ext,l}}} = tanh((\tau_{ext,s} - \tau_{ext,l})/2)$$
(4.6)

P_{ext} is usually small, on an order of a few percent, as mentioned above. Thus, Equation 4.6 reduces to:

$$P_{ext} = -\frac{(C_{ext,s} - C_{ext,l})NL}{2}$$
(4.7)

For polarization by selective extinction, we see a net polarization parallel to the short axis of the aligned grains, which is parallel to the external magnetic field. Note that, as shown in Equation 4.7, when more (aligned) grains are present in the cloud, the polarization of background starlight becomes higher.

4.2.3. Polarization by Thermal Emission

Dust grains absorb starlight and reemit at longer wavelengths, with the wavelength of maximum intensity, λ_{max}, determined by their temperature T (Wien's law):

(4.8)
$$\lambda_{max}T = 0.290 \, cm \, K$$

Typical temperatures for interstellar dust grains (10-20 K) correspond to wavelengths around 150-300 μm, while dust near a hot star (100-600 K) emits at 5-30 μm (Karttunen et al., 1996). In the ISM, dust grains are very small, typically $< 1 \, \mu$m. This size is very small compared to the wavelengths at which they will thermally radiate; thus, the emission efficiency Q_{em} is quite small. Q_{em} decreases as the grain size approaches zero, just as Q_{sca} does.

However, if the grains are elongated and aligned (again by an external magnetic field), the grains will be slightly more efficient for **E** parallel to the long axis of the grain than for **E** along the short axis; that is, $Q_{em,l} > Q_{em,s}$. We can approximate the intensity of light emitted by the grain along each axis to be related to the appropriate blackbody emission at that wavelength (I_{bb}) multiplied by its emission optical efficiency, $I_{em} = Q_{em}I_{bb}$. Thus,

the intensities used in Equation 4.4 are directly proportional to the efficiencies, and we obtain (Hildebrand, 1988):

$$(4.9) \qquad P_{em} = \frac{C_{em,l} - C_{em,s}}{C_{em,l} + C_{em,s}}$$

The net polarization is then perpendicular to (instead of aligned with) the magnetic field. Polarization caused by thermally emitting aligned grains is typically small, on the order of a few percent (Hildebrand et al., 1984).

We note that this equation only holds for an optically thin cloud. When $\tau_{em} >> 1$, light thermally emitted from grains located in the cloud interior will undergo selective absorption by grains closer to the observer (and emit radiation at the same time). Since the two processes create orthogonal polarizations, the net result is a cancellation of the polarization for the cloud. This is consistent with the fact that, as the cloud becomes optically thick, it starts to behave more similarly to a blackbody, which emits unpolarized light.

We conclude our discussion of polarization mechanisms by emphasizing that our treatment of polarization by thermal emission has been restricted primarily to small, ISM-sized grains. In this case, the grain size a is usually smaller than the wavelength λ. When we consider large grains (Chapter 11), we find that absorption efficiencies and absorption optical cross sections lose grain size dependence, which has consequences for the degree of polarization observed.

4.3. Grain Alignment

As mentioned above, polarization by selective extinction or by thermal emission can occur only when grains are preferentially aligned in some particular direction; otherwise, the random orientation of grains would cause a net cancellation of polarization. Although we do know that dust grains align with the surrounding magnetic field, the mechanism for grain alignment is still not fully understood. In the following sections, we present some common theories for grain alignment mechanisms.

In thermal equilibrium, dust grains experience rotation with energies $\frac{1}{2}kT$ along each rotational axis. To minimize rotational kinetic energy while conserving angular momentum, the grain will tend to rotate about its axis of maximum moment of inertia; that is, its short axis (Purcell, 1979). Thus the long axis will be preferentially perpendicular to **J**. What remains is to align **J** with the magnetic field **B**. We discuss two mechanisms that can do this.

4.3.1. Paramagnetic Relaxation

Consider a prolate spheroid dust grain (see Figure 4.2). If the dust grain is paramagnetic, it will feel an induced magnetic moment μ that is aligned with the external magnetic field B. If the grain is spinning, this magnetic moment will continually realign with the magnetic field. The process of realignment lags due to the spin of the dust particle. Since it is not instantaneous, the spinning grain will at any given moment have an induced moment that is slightly misaligned with the magnetic field. This misalignment will create a torque ($\tau = \mu \times \mathbf{B}$) that is antiparallel to the angular momentum **J** of the rotation, thus damping the rotational motion.
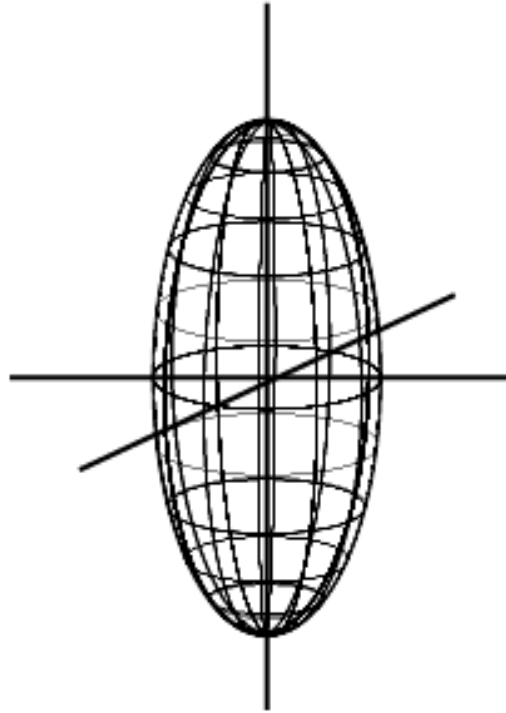
Figure 4.2. A prolate spheroid grain with principal axes of inertia. The grain will tend to rotate about the short axis of the grain. (This grain has two short axes and one long axis.)

For a dust grain spinning about its short axis, with the short axis oriented arbitrarily with respect to the magnetic field, rotation will be damped for those rotations with **J** orthogonal to **B**. The result is a dust grain rotating about an axis aligned with the surrounding field (Davis & Greenstein, 1951). The long axis of the grain is preferentially perpendicular to the magnetic field (see Figure 4.3).
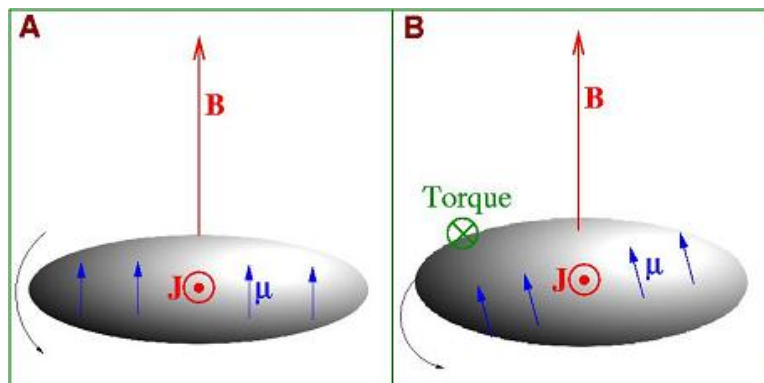
Figure 4.3. Paramagnetic relaxation. The magnetic moment of a spinning dust grain tries to align itself with the surrounding magnetic field. The delay in this alignment creates a torque, damping the rotation having **J** perpendicular to **B** and leaving only rotation with **J** parallel to **B**.

Although alignment via paramagnetic relaxation is possible, actual torques caused by induced paramagnetic drag are very small. Theories have been developed that increase the amount of torque caused by the induced magnetic moment, in order to attempt to make paramagnetic relaxation a viable grain alignment mechanism. For example, superparamagnetic materials, such as grains with ferrous elements (Lazarian, 2000, and references therein), experience a larger magnetic moment, and thus in turn feel a larger torque.

Another way to increase the torque needed for paramagnetic relaxation is through suprathermal rotation (Purcell, 1979). As mentioned above, bombardment by surrounding gas particles causes thermal rotation. In suprathermal rotation, hydrogen atoms collide with a dust grain and adhere to the surface. The surface of the grain contains a number of H_2 formation sites. The hydrogen atoms migrate to these sites, forming diatomic hydrogen. The energy released in this process kicks the molecule off of the surface of the grain, imparting angular momentum to the grain and increasing its spin. This increase

in angular speed means a larger drag angle between the magnetic field and the induced moment, thus increasing the induced torque caused by paramagnetic relaxation. However, it is not believed that the H_2 formation sites are stable over long timescales; thus, it is not believed that paramagnetic relaxation, even if supported by suprathermal rotation, could explain the observed degree of magnetic grain alignment (Lazarian, 2007, and references therein). Note that other mechanisms for inducing suprathermal rotation have been proposed (Purcell, 1979) but mostly these require stable grain surfaces and thus are problematic.

4.3.2. Radiative Torques

Another theory for the alignment mechanism of dust grains is radiative torques. In this scenario, we have a large collection of spinning dust grains that are each asymmetric under changes in parity. This asymmetry causes different absorption efficiencies for left- and right-handed circularly polarized radiation, that is, the grain "prefers" to absorb one type of polarization over the other (Draine & Weingartner, 1996). If the incident radiation is anisotropic, there is a net transfer of angular momentum from the absorbed photons to the grain. The dust grain will align such that its axis of rotation is either parallel or anti-parallel to the photon stream (see Figure 4.4, top).

Grains are believed to often contain a net charge, that, combined with the spin of the grain, creates a magnetic dipole moment μ. Similarly to paramagnetic relaxation, the presence of a magnetic field $\mathbf{B}$, will create a torque $\tau = \mu \times \mathbf{B}$ on the spinning grain, causing the grain to precess around the direction of the magnetic field. Depending on the original orientation of $\mathbf{J}$ with respect to $\mathbf{B}$, preferential alignment of either the long or
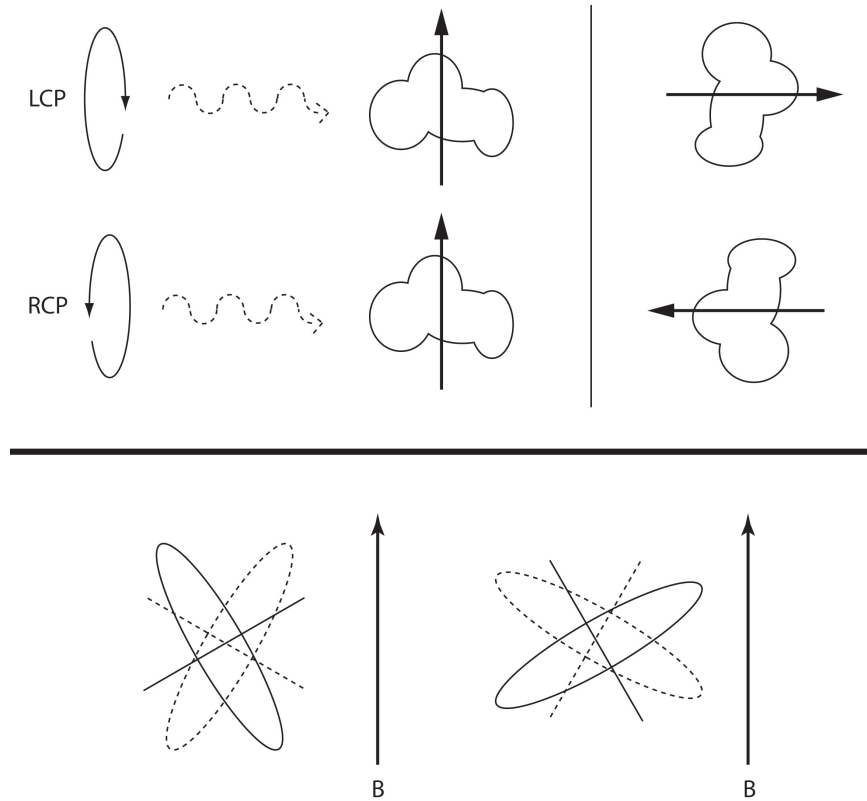
Figure 4.4. Dust grain alignment with **B** field via radiative torques. Top: Incoming light that is circularly polarized is incident on an asymmetric dust grain, causing a transfer of momentum and aligning the rotation axis according to the direction of photon flow. Bottom: Net charge on a rotating grain causes a precession of the rotation axis in the presence of a magnetic field **B**. Here we show this effect, using a line to indicate the orientation of **J** and an ellipse to show the orientation of the grain long axis. Dashed and solid symbols correspond to different snapshots during the precession. The net alignment of the grain can appear with either the long or short axis of the grain preferentially parallel to **B**, as we show at left and right, respectively.

short axis of the grain with $\mathbf{B}$ will occur (Figure 4.4, bottom). However, since photons are continually trying to align the rotation axes of the grains via the radiative torque mechanism, there is a competition between radiative torque alignment and precession. Computer simulations have shown that equilibrium is reached when the net alignment of $\mathbf{J}$ is parallel to $\mathbf{B}$, meaning the long axis of the grain is once again perpendicular to the magnetic field (Dolginov, 1972; Lazarian, 2007, and references therein).

4.3.3. Concluding Remarks

Despite the uncertainty in grain alignment mechanisms, simulations confirm that, in most cases, dust grains tend to align with their long axes preferentially perpendicular to an external magnetic field (Lazarian, 2007). Assuming that one can know with certainty that the polarization is due to aligned grains, and that one can furthermore determine whether the polarization is due to emission or absorption, then one can learn the direction of the ambient magnetic field. In star-forming clouds, where dust particles are small and polarization is certainly caused by thermal emission, astronomers have been able to make maps of the plane-of-sky magnetic field (Li et al., 2006; Crutcher, 2004). These maps have provided tests for theories and models that treat the role of magnetic fields in star formation.

Polarimetric studies of protoplanetary disks (Part 3) have the potential to provide information concerning the magnetic fields in these disks. This might help us to determine what role, if any, magnetic fields play in the planet formation process. More importantly, as we show in Part 3, the polarization properties of these disks may turn out to strongly depend on grain size. Thus, polarimetry of protoplanetary disks can potentially

place constraints on the grain size distribution and thus probe the initial phase of planet formation.

CHAPTER 5

Techniques for Far-IR/Submillimeter/Millimeter Polarimetry

5.1. Bolometer Arrays

Polarimetry at wavelengths from the far-IR through the millimeter using bolometer detectors has undergone a huge transformation since its inception in the 1980s. Detectors are improving in both sensitivity and pixel count, from one pixel for the first detectors to the current 384 pixels of the SHARC-II array (see Section 5.4). The optical efficiency, or fraction of incident power that actually reaches the detector, is improving as well, with current values as high as 70% (Dowell et al., 2003). Large telescopes have been built at sites with low atmospheric opacity, such as the South Pole and the Atacama desert. In the future, the airborne observatory SOFIA will allow us to carry out sensitive measurements in the far-IR, at wavelengths inaccessible from the ground.

Despite these advantages, however, polarimetric measurements at these wavelengths have their own set of challenges. First, to minimize detector noise, the bolometers must be cooled below $1\,\mathrm{K}$. This has been achieved through the use of cryogenic refrigerators, usually reaching ^{3}He temperatures of $0.3\,\mathrm{K}$. Polarimetry requires overcoming one other major obstacle: measuring polarized fluxes that are 10^{-6} or less of the total incident flux. As we noted in Chapter 1 interstellar clouds emit radiation having polarization of order 10^{-2} of the total source flux, but very small (10^{-6}) compared to the atmospheric flux. As another example, when measuring the polarization of the cosmic microwave background

(CMB) the polarized flux is a million times below the total CMB power. The polarized signature from inflationary physics is expected to be even lower (10^{-7} to 10^{-9}).

The challenges inherent in the observations of such relatively low polarized signals are being met with new technology combined with observational techniques in order to increase the overall signal to noise. We briefly discuss some of the methods employed.

Reduction of sky noise is accomplished by choosing locations with low amounts of precipitable water vapor. This includes mountaintops such as Mauna Kea in Hawaii, Mt. Graham in Arizona, the Atacama in Chile, and the South Pole. For this last site, temperatures are so cold that water vapor freezes (Lane, 1998).

5.2. Polarimetry

The easiest way to observe polarized light is to rotate a polarizing grid in front of a detector; this process, however, reflects a large portion of the incident light. Many polarimeters instead observe in dual-polarization mode; that is, looking at two orthogonal components of polarization simultaneously. For bolometer arrays, this means observing the reflected and transmitted light simultaneously, or making the detectors sensitive to $\pm Q$ or $\pm U$. By looking at both transmitted and reflected radiation, we can increase the signal to noise by a factor of $\sqrt{2}$. This also helps eliminate atmospheric noise.

Polarization modulation can help eliminate extraneous signals. Modulation refers to rotating the incoming polarization state. A polarization modulator is placed in front of the detector, usually at the input to the polarimeter. If the polarization is caused by an astronomical source (as opposed to the instrument), then as the modulator is moved, the polarization should change accordingly. In Part 2 we will compare and contrast

the commonly used half-wave plate (HWP) modulator with a new type of polarization modulator being developed at Northwestern University and Goddard Space Flight Center, the Variable-delay Polarization Modulator (VPM). For each "modulation" of the polarized signal (which can be thought of as a rotation of the polarization through some angle θ), we calculate the "polarization signal," defined below. The standard methods of polarization data acquisition for single-dish/bolometer observations are described in the next section.

5.3. Data Acquisition and Analysis

In this section we review the methods used to derive the polarization signal from a dual-polarization instrument for a single modulator position (Hildebrand et al., 2000). Removal of the proportionately large sky signal present in our observations requires fast switching of the telescope beam between two points: the source itself and an off-source (i.e., blank sky) point. The chopping frequency must be fast enough to overcome $1/f$ noise from the atmosphere and often ranges from 3-15 Hz. As the secondary is chopping between on and off source, data points are calculated by subtracting the voltage value of the "right" beam from that for the "left" beam. The subtraction of these voltage values results in one "demodulated" data point, or one "chop".

After a predetermined number of chops, we then "nod" the telescope. This consists of switching the source from the left beam to the right beam. The left beam now focuses on a new sky position (see Figure 5.1). This nodding technique reduces effects caused by temperature differentials across the primary mirror. We observe the object in a "left-right-right-left" $(l - r - r - l)$ pattern, which allows us to eliminate long-term linear progressions in the signal, for example, if the primary temperature were slowly drifting

53
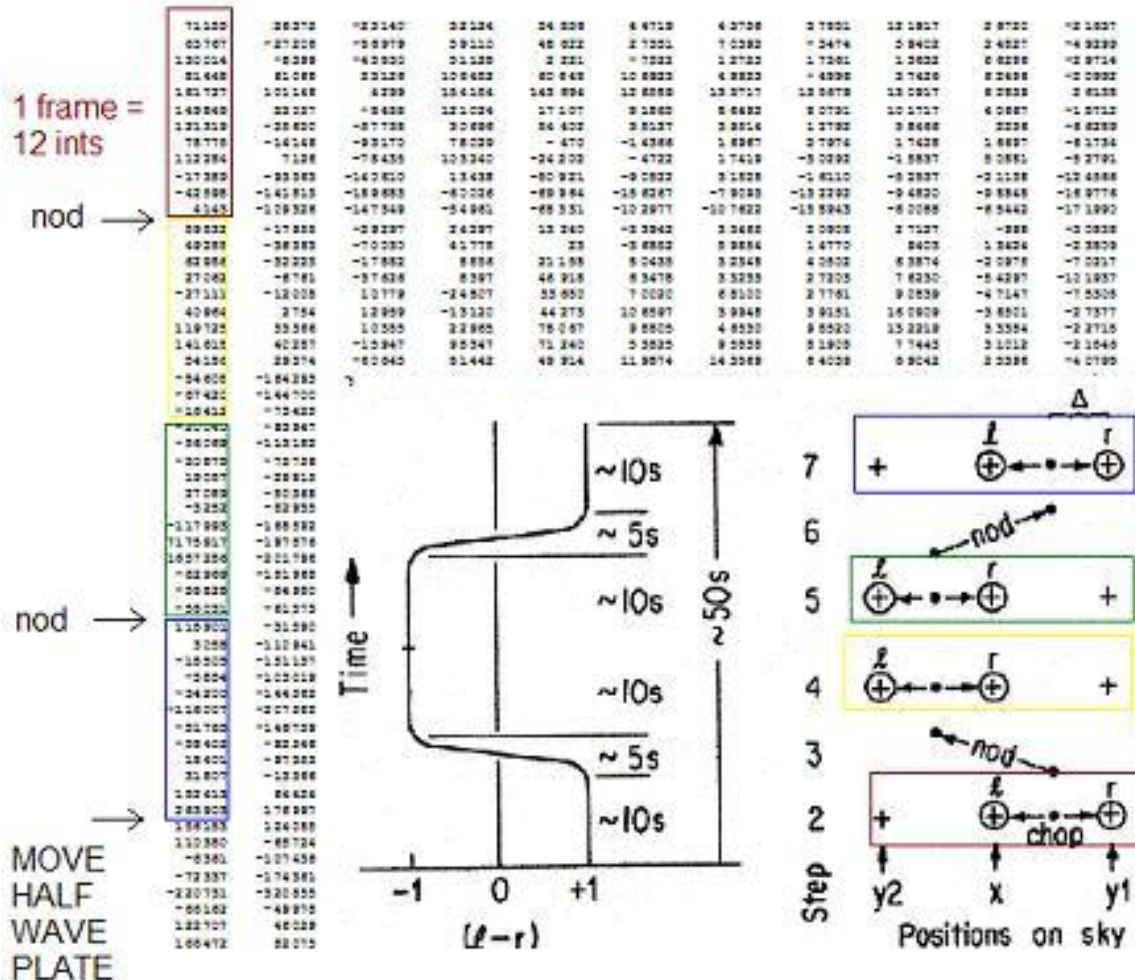
Figure 5.1. Example of data analysis process for single-dish/bolometer applications. Insert taken from Hildebrand et al. (2000). Each column of the sample data represents the output signal (voltage vs. time) of one bolometer, or pixel for either the R or T array. Each number in the column is one "int", or one demodulated (left-right) signal measurement. A number of ints, or *chops*, make up one nod. (In the case shown, 12 ints comprise one nod.) We then nod the telescope and take another set of ints/chops. After completing one "nod-pair" (l-r-r-l), we have collected all of the data for one position of the polarization modulator, here, a HWP.

with time. Each left or right position (i.e., "nod") in this "chop-nod" cycle contains an equal number of demodulated chop values; an average over all chops is computed for each nod, l_1, r_1, r_2 and l_2.

To observe dual polarization simultaneously, a polarizing grid is used to direct orthogonal linear polarization components into two detector arrays such that one array observes the reflected light and the other transmitted light. The intensity for one pixel in each array (reflected R or transmitted T) over one chop-nod cycle is calculated as:

(5.1)
$$R(or\ T) = (l_1 - r_1 - r_2 + l_2)/4$$

where the four terms refer to the averaged nod values as described above (r terms are subtracted, since they are negative values). The measured polarization signal S_{mod} for a given modulator position is:

(5.2)
$$S_{mod} = \frac{(R_{mod} - fT_{mod})}{(R_{mod} + fT_{mod})}$$

where f is the relative gain between the corresponding R and T pixels being measured $((\sum R)/(\sum T))$, averaged over all chop values for a full modulator cycle. Stokes parameters are then calculated from the S_{mod} values for one modulator cycle, in a manner determined by the type of polarization modulation used. This is discussed in more detail in Chapter 7.

5.4. The SHARP Polarimeter at CSO

SHARP (the SHARc-II Polarimeter) is a fore-optics insert that adds polarimetric capability to the SHARC-II camera that operates at the CSO telescope on Mauna Kea. SHARP splits incoming light into two orthogonally polarized beams that are re-imaged onto separate 12×12 arrays at each end of the SHARC-II detector array (which is 12×32). Note that SHARP is thus a dual-polarization instrument. The detectors in SHARC-II are ^{3}He cooled to 0.3 K. A rotating HWP resides just before the light-splitting optics, which here consists of a novel cross-grid design to minimize lost signal. SHARP sits at the Nasmyth focus of the telescope and operates at either 350 or 450 μm. SHARP is shown in Figure 5.2.

SHARP achieves a beam full-width half-maximum (FWHM) of $\sim 9''$ at 350 μm and $\sim 10''$ at 450 μm. The polarization efficiency is 93% at 350 μm and 98% at 450 μm. The instrumental polarization is below 1% for each waveband (Li et al., 2008). For good atmospheric conditions ($\tau_{230\,GHz} = 0.05$, target at 1.3 airmasses), and assuming an observing efficiency (integration time to observing time) of 50%, SHARP can observe a $\pm$ 1% polarization measurement of a 2.6 Jy point source in 5 h of integration time (Li et al., 2008).

The CSO is located near the 4,000 m summit of Mauna Kea in Hawaii. The telescope consists of a 10.4 m Leighton radio telescope (Phillips, 1997) with sensor adjustments that improve dish performance. The CSO includes a secondary mirror that we chop at ~ 1 Hz.

Figure 5.2. The SHARP Polarimeter at the Caltech Submillimeter Observatory (CSO). SHARP consists of four boxes that are mounted at the Nasmyth focus of the telescope. Light comes in through the elevation bearing (from the top left in this photo) into the top box, where it is sent down into the optics path. These optics split the light into orthogonal polarizations and add a linear displacement between the two beams, then sends the light into the SHARC-II camera (located at the top right of this photo).

Part 2

The Hertz-VPM Polarimeter

In the previous chapter, we discussed some of the basic observational techniques used to observe polarization of astronomical objects at submillimeter wavelengths. As mentioned previously, this is not trivial; care must be taken to maximize the received source flux and remove extraneous signals. Polarization modulation is a key element to any polarimeter design, and can be accomplished in a variety of ways. The most common method is to use a birefringent half-wave plate (HWP) to rotate the incoming polarization state. Despite the simplicity of its design, it becomes desirable to look to other technologies when one considers multi-wavelength operation and the durability that may be required for airborne or space-borne operation.

Part 2 of this thesis discusses the design, construction and testing of a new type of polarization modulator, the Variable-delay Polarization Modulator, or VPM. Chapters 6 and 7 compare the design and performance of the VPM to the widely used HWP, and discuss features that make the VPM a competitive alternative to the HWP. Chapter 8 discusses the experimental setup for the Hertz/VPM polarimeter. Finally, in Chapter 9 we shall see that the characterization of the dual-VPM system led to interesting discoveries concerning the performance of these modulators and its dependence on wire grid properties.

CHAPTER 6

The Half-Wave Plate and the Variable-delay Polarization

Modulator

The half-wave plate (HWP) is a device that is able to induce a half-wave phase delay between incident orthogonal polarization components. In this thesis (unless otherwise specified) we will use the term "HWP" to mean a birefringent device (for example, a quartz crystal) cut such that its optic axis is parallel to the front and back surfaces (orthogonal to the direction of light propagation), and whose thickness is chosen such that the plate will induce a 180° phase delay between orthogonal polarization components. A rotation of the HWP by an angle θ causes a rotation of the plane of polarization by a corresponding 2θ. The HWP can be summarized as a device that induces a fixed delay between orthogonal components, in effect rotating the polarization basis.

A "reflective HWP" can be constructed by rotating a polarizing grid in front of a mirror. Light incident upon the grid is separated into polarization either parallel or perpendicular to the grid wires. The former is reflected by the grid, while the latter is transmitted to the mirror, reflects and then recombines with the orthogonal counterpart (Fig. 6.1). For light with an incident angle of θ_{inc}, the induced path length difference l is given by:

$$l = 2d \cos \theta_{inc} \tag{6.1}$$
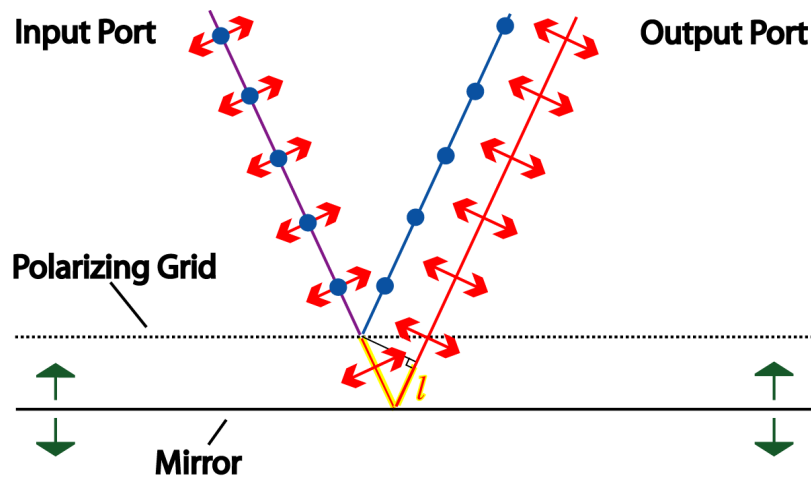
Figure 6.1. A "reflective half-wave plate". Light incident upon a wire grid is separated into orthogonal polarization components; the component parallel to the wire grid is reflected, while the perpendicular component is transmitted and reflected by a mirror, traveling an extra distance l. When the delay l is set equal to half of the wavelength, this device has the same functionality as a birefringent half-wave plate (HWP)

If we set this path length difference to $\frac{\lambda}{2}$, the device operates as a HWP in reflection. Rotation of the grid is physically equivalent to rotating a HWP. This device has been used for astronomical polarimetry at millimeter wavelengths (Shinnaga et al., 1999; Siringo et al., 2004).

Suppose that instead of maintaining a fixed distance between the grid and mirror surfaces, we now move the mirror back and forth, thus changing the physical path length difference between the orthogonal polarization components. By doing so, we fix the polarization basis and vary the phase delay; devices of this type have been denoted Variable-delay Polarization Modulators, or VPMs (Chuss et al., 2006b).

One VPM switched between half and full wave delays is equivalent to turning a HWP "on" or "off", that is, moving a HWP in and out of the beam. We can calculate the

necessary grid-mirror separation distances from Equation 6.1; for example, $350\,\mu$m light incident at $20°$ requires settings of 93 and $186\,\mu$m, respectively. However, if polarization incident on the VPM grids is either completely parallel or completely perpendicular to the grid, then the polarization will not be modulated, regardless of the separation distance.

This problem can be solved by placing two VPMs in series, with their grids rotated by $22.5°$ with respect to one another ($45°$ in Stokes space; see Figure 6.2). In this way any polarization not modulated by one VPM will be modulated by the other (Chuss et al., 2006a). The dual-VPM system can thus accurately reproduce the function of a rotating HWP (provided that the analyzer grid of the polarimeter in Figure 6.2 is not aligned parallel or perpendicular to the grid wires of VPM 2).

Single VPMs have been used for astronomical polarimetry at millimeter wavelengths in the form of a modified Martin-Puplett Interferometer (Battistelli et al., 2003). However, since only one VPM was used, another modulator (a double-fresnel rhomb) had to be incorporated. The dual-VPM modulation scheme has the advantage of requiring only small translational motions, rather than rotation, to obtain full modulation of all linear polarization states. This paper reports the first astronomical observations using a submillimeter polarimeter incorporating a dual-VPM modulator.

The VPM has several advantages over the HWP. The VPM, in contrast to the birefringent HWP, operates in reflection, and so avoids some of the drawbacks of dielectrics. Also, assuming near perfect performance over a large range of wavelengths, the wavelength of operation for the VPM can be easily tuned. In comparison, for multiwavelength operation the dielectric HWP requires multiple birefringent layers and complicated (and often costly) achromatic antireflective coatings. The VPM operates without a rotation
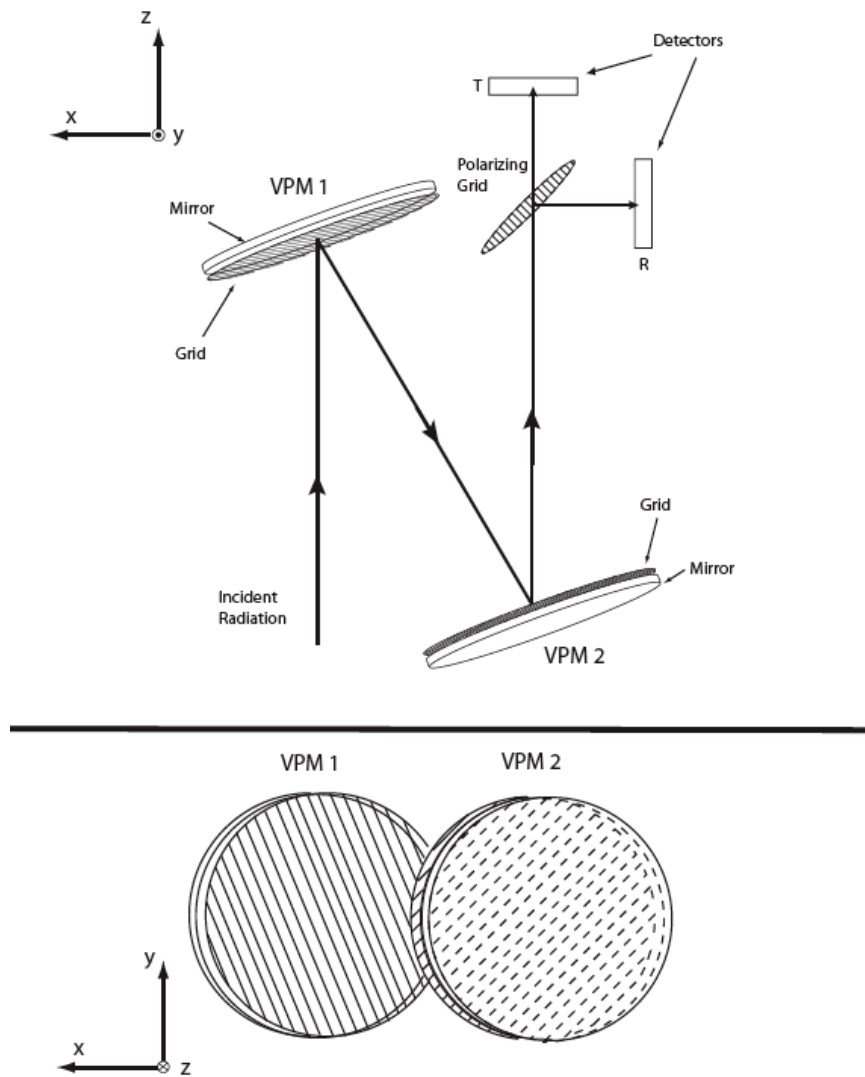
Figure 6.2. Two views of a schematic optical path for a polarimeter incorporating a dual-VPM modulator. The upper panel shows a top view while the lower panel shows the view "seen" by the incoming radiation. The radiation is reflected by two VPMs having their grid wires rotated by 22.5° with respect to one another, and is then incident upon a polarizing grid that splits the beam into orthogonal polarization components directed to detectors R and T (standing for reflected and transmitted). Note that the figure shown above is a general schematic, and is not representative of the actual grid settings and orientations used for the Hertz/VPM experiment.

bearing; the small motion of the mirror can be accomplished via piezoelectric motors and flexure bearings. Flexure bearings operate without friction and are generally considered to be the most durable of all non-levitating bearings. Finally, the freedom of a variable delay means that the VPM can also act as a quarter-wave plate. For broadband continuum work, the magnitude of astronomical circular polarization is often expected to be negligible; thus, measuring circular polarization can allow a check of the systematics of an experiment.

The VPM does have challenges in its construction, characterization and operation. The desire for high tolerances (we chose general tolerances below $10\,\mu$m) requires careful design. It also makes the device susceptible to large systematic vibrations. Also, error caused by non-parallel grid and mirror surfaces must be carefully minimized, requiring longer setup times than for the HWP. High grid efficiencies require flat and finely spaced wire grids, which can be expensive to produce. Finally, as we shall see in Section 9.2, VPM characterization is nontrivial. But first, we discuss basic polarization measurement techniques for the HWP and dual-VPM modulators.

CHAPTER 7

Comparison of Data Analysis Techniques

We refer back to Section 5.3 for basic bolometer/single-dish polarimetry techniques. Having obtained a polarization signal S_{mod} for each modulator position (Equation 5.2), we now apply specialized analysis methods for each respective polarization modulator.

We define one "HWP cycle" as a stepped rotation of the device through a set of angles spaced evenly over a 180° degree range. The polarization signal S_{mod} is plotted as a function of HWP angle, and a sine curve is fit to the data. The amplitude of the curve gives the degree of polarization P, and the phase of the curve gives the polarization angle ϕ. We follow a fitting procedure similar to that explained by Platt et al. (1991). That is, the polarization signal as a function of angle (S_θ) has the general form:

(7.1) $$S_\theta = A sin[4(\theta - \phi)]$$

where θ is the HWP angle. The amplitude A corresponds to the percent polarization and the offset ϕ gives the angle of polarization with respect to a coordinate system chosen relative to the experiment. This angle can then be traced back onto the sky to find the actual polarization angle. We modify the equation so as to take into account the arbitrary offset of the HWP zero relative to our experiment. We also adjust the sign of the HWP

angle so as to account for the number of reflections between the HWP and the point of measurement.

For a "VPM cycle", the VPM grid-mirror separations are switched between "on" and "off" positions in four different combinations (VPM 1-VPM 2): pos1: on-on, pos2: on-off, pos3: off-on and pos4: off-off. Here, "on" refers to a half-wave delay and "off" refers to a full-wave delay. Unlike the HWP, the resulting polarization signals do not correspond to a sine curve; instead, we calculate the normalized Stokes parameters as follows (Chuss et al., 2006b):

$$(7.2) \qquad\qquad q = (S_{pos2} - S_{pos1})/2$$

$$(7.3) \qquad\qquad u = (S_{pos4} - S_{pos3})/2$$

These equations are consistent with the convention that the time-reversed polarized light beams from the R and T detector arrays reach VPM 2 with polarization angles rotated by $\pm 45°$ with respect to the grid wires of VPM 2 (e.g., see Figure 6.2). This condition is necessary for full modulation of the polarization signal. For our experiment, R is sensitive to Stokes $-U$ and T is sensitive to $+U$. If the arrays were flipped in sensitivity, we would simply set q to $-q$ and u to $-u$.

After the determination of q and u (for the modulator used), P and ϕ then follow from Stokes definitions:

$$(7.4) \qquad\qquad P = \sqrt{q^2 + u^2}$$

$$(7.5) \qquad\qquad \phi = (1/2)\arctan(u/q)$$

Here we define ϕ as the angle (in radians) relative to the coordinate system of our optics plane. We note that P and ϕ are non-Gaussian; thus, the uncertainty in these quantities do not follow from normal propagation of errors. Instead, σ_P and σ_ϕ are given by:

$$(7.6) \qquad\qquad \sigma_P = (\sigma_q + \sigma_u)/2$$

$$(7.7) \qquad\qquad \sigma_\phi = (1/2)\arctan(\sigma_P/P)$$

The cycles described above were defined for a system with only one modulator installed. When both HWP and dual-VPM are present, as we shall see is the case with our Hertz/VPM polarimeter, the above definitions are still applicable, provided one modulator is held fixed while the other is cycled.

CHAPTER 8

Design of Hertz/VPM

Having described the theory behind the function of both the HWP and dual-VPM polarimeter and their respective analysis techniques, we now describe the physical implementation of the Hertz/VPM polarimeter. The Hertz/VPM polarimeter consists of the dual-VPM modulator and the Hertz polarimeter, formerly used at the CSO. An optics train, including the dual-VPM modulator, was built and used in front of Hertz. We tested the full Hertz/VPM system at (SMTO) on Mt. Graham in Arizona during April 16-24, 2006. The following year, we conducted a series of tests to further characterize Hertz/VPM in the lab at Northwestern University. Below we will outline the construction of the VPMs and the experiment carried out at both SMTO and the lab. This includes a description of the optics train as well as our use of the Hertz polarimeter.

8.1. VPM Construction

Our VPMs have four main elements: 1) an aluminum frame, consisting of a rectangular box with the top and back panels removed, 2) an optical quality mirror on a translation stage, mounted inside to the bottom of the frame, 3) a wire grid mounted to the front of the frame, and 4) a piezoelectric actuator, mounted in front of the frame, that controls mirror motion (Voellmer et al., 2006).

The mirror is composed of vapor-deposited aluminum on glass and rests on a moving stage mounted on a kinematic variant of a double-blade flexure linear bearing. The main
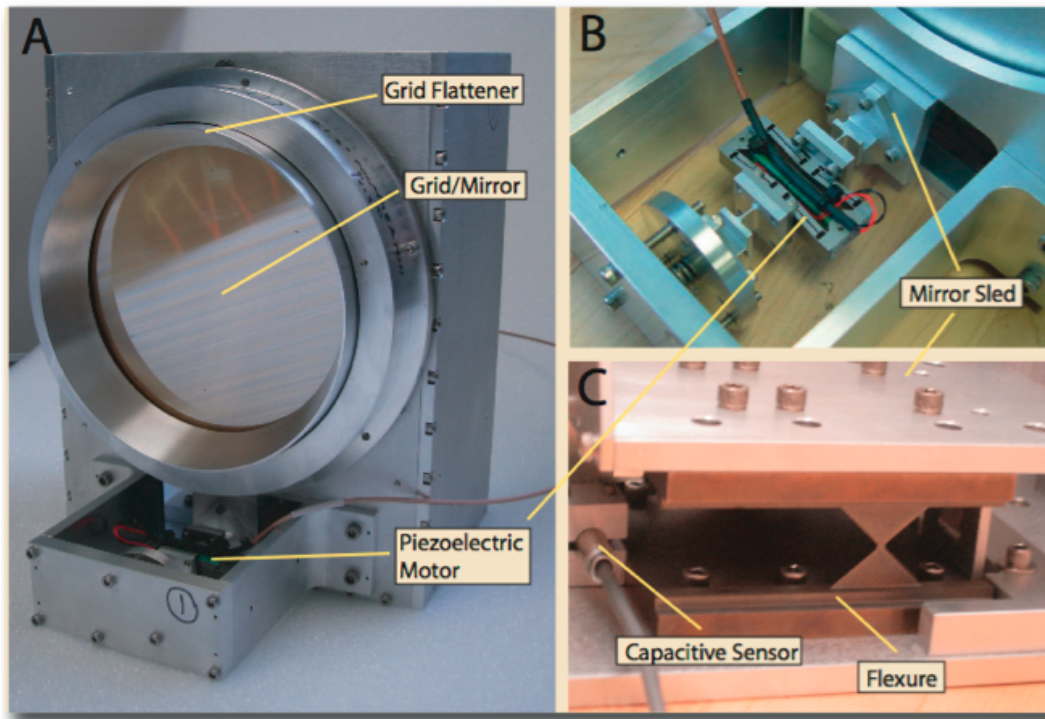
Figure 8.1. Views of one VPM. A: Front view. Wire grid is held to the front of the aluminum frame by rare earth magnets. Grid flattener increases planarity of wires. Its interior edge is milled to correspond with a 20° incident angle. B: View inside housing for piezoelectric actuator. The motor is surrounded by titanium flexures which magnify the piezo motion. The actuator is connected to two universal joint flexures to couple motion to the mirror and to absorb any twisting motion caused by misalignment. C: Back view under mirror mount, showing double-blade flexure and capacitive sensor. Sensor measures actual mirror-grid separation distance and sends this information to servo controller, completing control loop.

flexures are machined in an hourglass shape so as to improve the parallelism of the bearing during motion. This is shown in Figure 8.1. The parallelism of the mirror motion was measured to be $1.5\,\mu$m across the $150\,$mm diameter mirror surface over a $400\,\mu$m throw.

Commercial piezoelectric actuators (DSM) control the mirror motion. These motors rest perpendicularly to surrounding titanium flexures; elongation of the piezo pushes against these flexures, which subsequently magnify the motion (Figure 8.1). We measured

the reliable full throw for the piezos to be $400\,\mu$m. Crossed flexure universal joints are coupled to each end of the piezoelectric motor. The front universal joint is coupled to an adjustable plate on the front of the motor housing; this allows the user to define the actuator motion relative to the rectangular frame. The back universal joint is connected to the moving mirror stage via an L bracket. The universal joints act to prevent non-parallel motion of the actuator from affecting the mirror motion (Voellmer et al., 2006). A servo control amplifier controls distance to within $1\,\mu$m. The grid-mirror displacement is measured using a capacitive sensor mounted to the bottom of the aluminum frame.

Grid quality was of primary concern in the construction of the VPMs, as error in wire spacing and grid flatness can create grid inefficiencies. We used two 15 cm diameter freestanding grids for the experiment. Manufactured by Millitech, the grids consist of $25\,\mu$m diameter gold coated wires, with a nominal spacing of $63\,\mu$m. We measured an actual average grid spacing of $67.5\,\mu$m. The grids are rated to frequencies up to 1600 GHz (wavelengths down to $187.5\,\mu$m), with a nominal efficiency of 95% at this frequency.

We desire an rms grid flatness that is less than 1% of the operating wavelength. Obtaining straight and parallel wires requires them to be under considerable tension. This tension causes a "potato chip" effect, with the tension on the wires deforming the wire grid frame out of planarity. Due to this effect, we measured the wires in the grids to have an rms flatness of roughly $35\,\mu$m, equal to one tenth of our operating wavelength. To improve grid efficiency, we developed a grid flattener. The flattener has an optically flat end surface which rests against the stretched wire surface (Voellmer et al., 2006). Set screws bring the flattener into contact with the wires just until the wires are deflected, minimizing the stress on the flattener itself. The flattener was able to improve the rms

flatness to $\sim 2\,\mu$m. Figure 8.1 shows the flattener; the interior surface was machined at a 20° angle in accordance with the beam incident angle.

The grid is pulled toward the VPM frame with rare earth magnets embedded in the front plate, while three set screws in the grid mount push against the frame, establishing the grid-mirror parallelism. The set screws align with small divets located near the magnets on the front plate to establish repeatable rotational positioning of the wire grid.

Good parallelism between the mirror and grid surfaces is crucial to obtaining accurate phase delays and parallel polarization beams. To set and measure the parallelism, we used a commercial monocular microscope with $200\times$ magnification and mounted it on a linear translation stage with a micrometer, which in turn was mounted on a moveable base. This setup is shown in Figure 8.2. The aluminum mount for the microscope has mounting holes at two different heights, corresponding to different measurement locations along the edge of the grid.

To begin, we mount the grid to the front of the rectangular frame, aligning the set screws with the corresponding divets on the front surface. Adjustments are made with the set screws to move the grid close to the mirror surface, moving one screw at a time. A target separation distance is determined, calculated such that the mirror at its closest position is $50\,\mu$m from the grid. Using the microscope, the distance between the grid wires and their reflection is measured, and the set screws are adjusted until the separation distance equals the target distance.

We repeat this procedure for each of three points on the wire grid; usually two or three iterations around the circle are needed. The alignment process results in parallelism of roughly $5 \pm 3\,\mu$m.
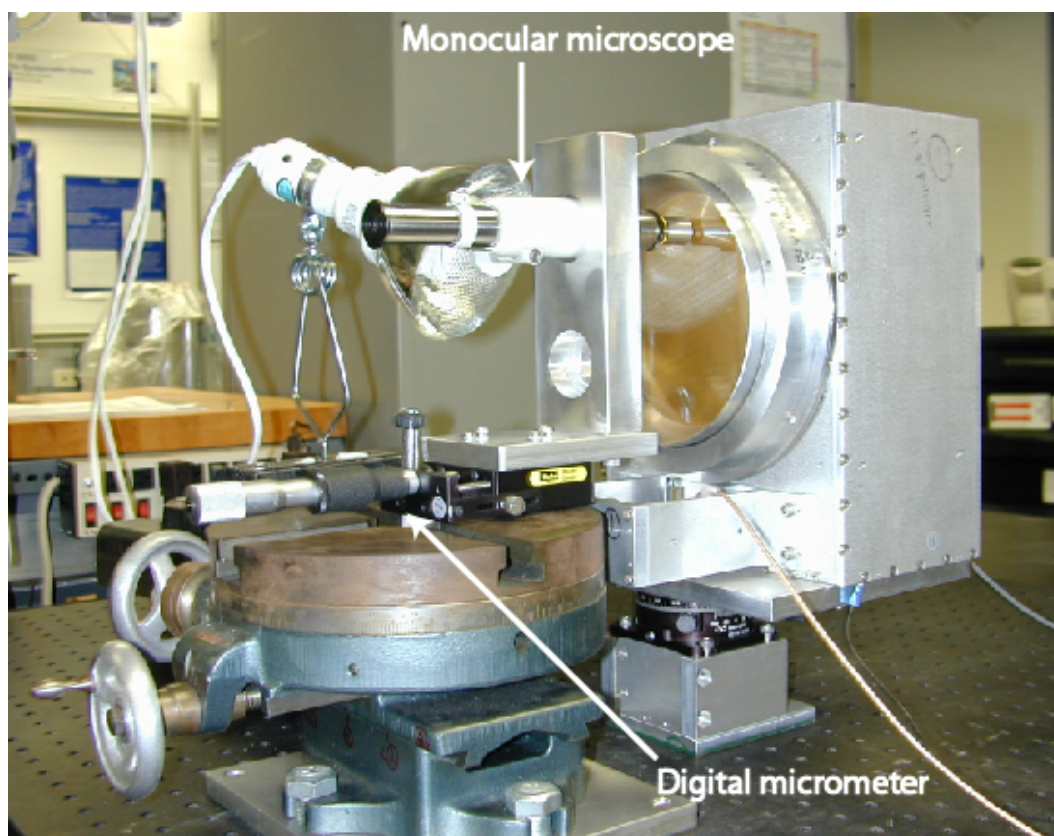
Figure 8.2. Microscope setup for grid-mirror parallelization measurements. The microscope is mounted on a bracket that is moved toward and away from the grid via a linear translation stage that incorporates a digital micrometer. Measurements are made at three points around the edge of the grid.

8.2. Optical Interface to Telescope

Mt. Graham is located near Safford, AZ, and is operated by the University of Arizona. The site rests at approximately 10,500 feet and has good submillimeter ($\tau_{230\,GHz} \leq 0.06$) nights roughly 10-15% of the time during the peak months of December-February, with a slightly lower percentage of good submillimeter nights in April. We now describe the constructed optics train, the Hertz polarimeter, and the control system for the experiment.
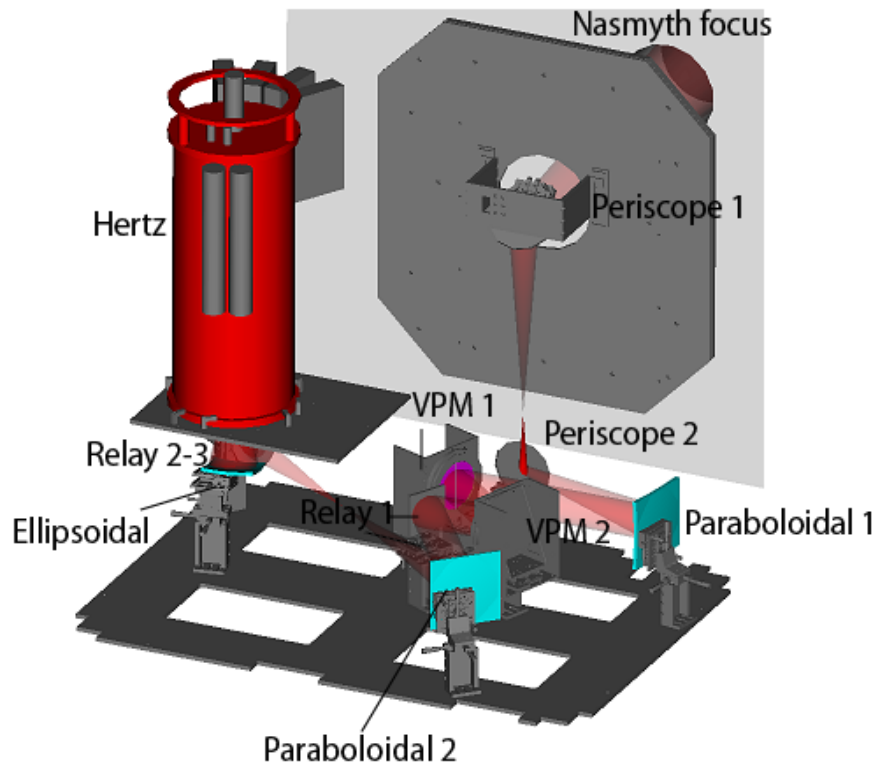
Figure 8.3. Optics path of Hertz/VPM experiment at SMTO. Optics sit at Nasmyth focus of telescope. Light is reflected down into the optics plane by two periscope mirrors. Light is collimated with a paraboloidal mirror, then passes through the VPMs before being refocused by the second paraboloidal mirror. After refocusing, a series of relay mirrors sends the light to an ellipsoidal mirror, which refocuses the light, this time to match the focal length of Hertz.

The Heinrich Hertz Telescope at the SMTO has a $10\,\mathrm{m}$ primary and operates between 0.3 and $2\,\mathrm{mm}$ wavelengths. The focal ratio at the Nasmyth focus is 13.8 (Baars et al., 1999). During our observations we chopped the secondary between two sky positions separated by $4'$ in cross-elevation at a rate of $3\,\mathrm{Hz}$.
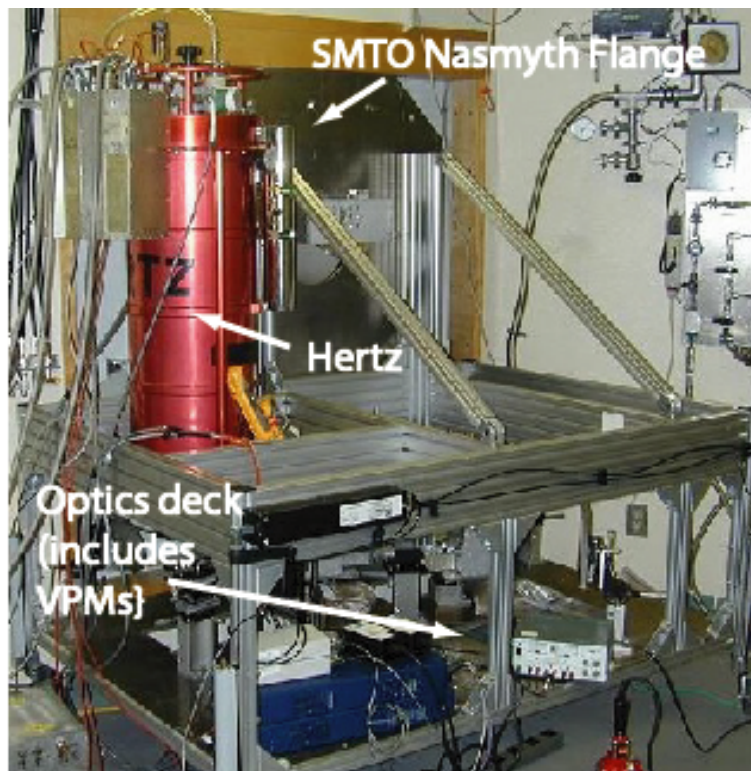
Figure 8.4. Photo of the Hertz/dual-VPM experiment at the SMTO. Optics bench mounts to wall via a large flange; the optics sit at the Nasmyth focus.

Figure 8.3 shows the optics path for the experiment. Light from the telescope is incident upon two flat periscope mirrors that bend the light down into the horizontal optics plane. The light is then collimated using an off-axis paraboloidal mirror before reaching the VPMs. VPM 1 has its grid wires rotated 22.5° counterclockwise from the horizontal, while the grid wires for VPM 2 are aligned horizontally. After passing through the modulators, the beam is then refocused using a second off-axis paraboloidal mirror. Next, a series of two additional relay mirrors sends the beam to an ellipsoidal mirror which refocuses the light to match the focal ratio of the polarimeter (4.48). Table 8.1 lists optics components and their properties. The optics were aligned in a two-step process; the first was a laser alignment of the optics carried out in the lab at Arizona. Second,

cold load tests were conducted at SMTO to ensure that the beam was centered on each optical element.

We define the Stokes parameter reference frame for Hertz-VPM by the convention described in Section 2, with $-Q$ aligned with the Earth's gravitational field. (Thus, $+Q$ is horizontal, $+U$ is 45° CCW from horizontal as viewed looking toward the incident beam, etc.) The input polarization is referenced to the input to the polarimeter, which we define to be just before the first paraboloidal mirror (see Figure 8.3).

In designing our dual-VPM system, one concern we faced regarding the optics was beam walkoff in the VPMs, the lateral translation between orthogonal components after they have passed through the mirror-grid system. Simple geometry shows that the total walkoff can sum to a significant fraction of the wavelength. We tried to minimize this effect in two ways. The first was to place each VPM as close as possible to a pupil, as lateral shifts at a pupil translate only to different incident angles at the focal plane. This angular displacement is directly proportional to the incident angle at the VPMs. Thus, to further minimize walkoff effects we made the incident angle as close to normal as possible. We chose this angle to be 20°, which allowed for sufficient beam clearance through the optics.

We also needed to position the wire grid for VPM 1 such that the actual grid angle "seen" by light incident at 20° was 22.5°. We determined the appropriate angle through the following calculation: assume a wire of length L in the wire grid makes an angle θ with the horizontal (Figure 8.5). We determine the new angle observed, θ', as seen from an incident angle of α (that is, when the wire is rotated by an angle α.)
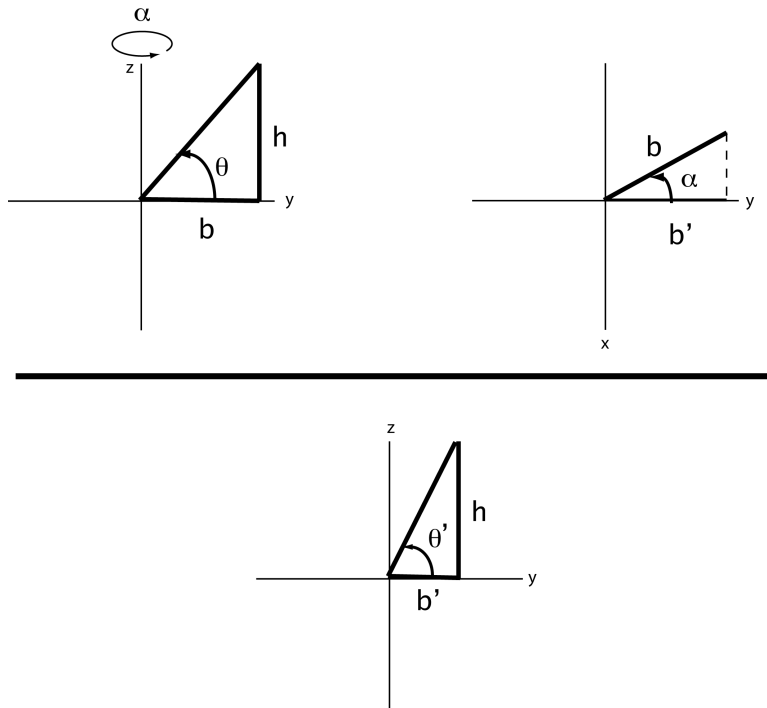
Figure 8.5. Change of grid angle due to non-normal angle of incidence. Rotation about the z axis by an angle α causes the light beam to "see" a truncated base b' due to projection effects, and thus a larger angle θ'. Therefore, we must adjust the original angle θ to compensate for this in order for the beam to "see" the appropriate grid angle.

With respect to the horizontal, the base and height of the triangle are b and h, respectively. Using simple geometry we have:

$$(8.1) \qquad \tan \theta = h/b \rightarrow h = b \tan \theta$$

Now, we rotate the wire and angle α about the z axis. If we were to then view the triangle, it would have a new base b', but the same height h. Therefore, the relation between h and the two new parameters is:

$$(8.2) \qquad\qquad \tan\theta' = h/b'$$

The bases b and b' are related through the rotation angle α:

$$(8.3) \qquad\qquad \cos\alpha = b'/b$$

Plugging in for h and b give:

$$(8.4) \qquad\qquad \tan\theta' = \tan\theta/\cos\alpha$$

If we wish to have light incident at $20\,^\circ$ see the VPM 1 grid at an angle $\theta' = 22.5\,^\circ$, then the actual grid angle θ should be $21.3\,^\circ$.

8.3. The Hertz Instrument

Hertz contains two 32-bolometer arrays (6×6 with the corners removed), cooled to $0.3\,\mathrm{K}$ via a Helium-3 refrigerator. An analyzer grid splits the incoming signal into two orthogonal linear polarizations and directs each to a detector array. This dual-polarization observing strategy results in a $\sqrt{2}$ increase in the signal-to-noise over signal polarization systems, and also aids in removing sky noise, which is correlated between arrays (Hildebrand et al., 2000). The polarimeter operates at $350\,\mu$m, with a relative bandwidth of $(\Delta\lambda)/\lambda = 10\%$. Hertz contains cold reimaging optics, using quartz lenses (Schleuning et al., 1997).

Table 8.1. Optics Elements of the Hertz/VPM Experiment and Their Properties

Element	f/# or focal length	Distance to next optic (mm)	notes
telescope	13.8	2410.6	
periscope 1	–	777	
periscope 2	–	526	
paraboloidal mirror 1	695 mm	620	off-axis paraboloid
VPM1	–	300	grid 22.5° CCW from horizontal
VPM2	–	225	grid horizontal
relay mirror 1	–	537	
paraboloidal mirror 2	695 mm	1161	off-axis paraboloid
relay mirror 2	–	225	
relay mirror 3	–	184	
ellipsoidal mirror	900 mm (input) 360 mm (output)	210	distance is to dewar window
Hertz	3.9/3.5	–	pupil lens/detectors

Hertz incorporates a quartz HWP, located at a cold pupil stop. Although we did not require this for polarization measurements carried out with the dual-VPM polarimeter, we used it for two purposes: first, by using the Hertz instrument in its original HWP-polarimeter mode, we were able to measure the linear polarization state at the output of the VPMs, providing a diagnostic of the dual-VPM modulator by itself. Second, as mentioned in Chapter 7, polarization observations with Hertz/VPM require that the time-reversed polarized light beams from the R and T detector arrays reach VPM 2 with polarization angles rotated by $\pm45°$ with respect to the grid wires of VPM 2 (e.g., see Figure 6.2). It was convenient to achieve this condition by rotating the HWP in Hertz rather than having to rotate the entire dewar.

We thus needed to determine the HWP angle that satisfied this criterion. At the SMTO, we accomplished this by placing a polarizing grid with horizontal wires in the optics train, directly after VPM 2. We then rotated the HWP until the signals were approximately equal in the R and T arrays. This angle was determined to correspond to an encoder reader of 96° (relative to an arbirary offset). We collected data at both 96° and the equivalent angle of 51° (which switches only the sign convention of the measured Stokes parameter, as seen in Chapter 7).

8.4. Control System

The control system is outlined in Figure 8.6. The main control computer sends commands to the other computers through a user-operated GUI. The main control computer communicates via TCP/IP with three computers: the telescope control computer, which controls the telescope motion and positioning, the data acquisition computer, which

records bolometer output to file along with header information, displays data onscreen, and controls the chopping secondary mirror, and the Ethernet Data Acquisition System (EDAS) which operates the modulators (HWP and VPMs).

The data acquisition computer receives, stores and displays data sent from the Hertz detector. Signals originate in Hertz as bolometer voltages that are amplified and then converted to a digital signal via an A/D converter. The data acquisition computer incorporates a custom-built Data Signal Processor (DSP) card. The computer records only the chopper-demodulated (i.e., on source – off source) signals. The DSP card performs the demodulation of the incoming data stream in synchronization with the chopper reference signal that it generates and sends to the secondary mirror controller. After demodulation, the data acquisition computer saves the demodulated data for each pixel to disk.

The EDAS (Intelligent Instruments) is a modular system computer that allows remote operation via an internet connection. Its use of flash memory eliminates the risk of hard drive failure. Three modules are connected to the EDAS main CPU and power modules: a serial port module, an analog output module (AO) and an analog input module (AI).

To move the VPM mirrors, a target position is sent by the main control computer to the EDAS, which sends that command (via binary serial communications) to the servo controller. The servo sends the actual position recorded by the capacitive sensor back to the EDAS (via binary serial) which relays it to the main control computer (via TCP/IP). To rotate the HWP, the EDAS sends serial commands to a stepper motor indexer, which controls the HWP motor. The EDAS measures the HWP positions by first applying an output voltage across a HWP encoder via the AO. The custom-built HWP encoder consists of a cryogenic rotary variable resistor mounted to the HWP. The output voltage
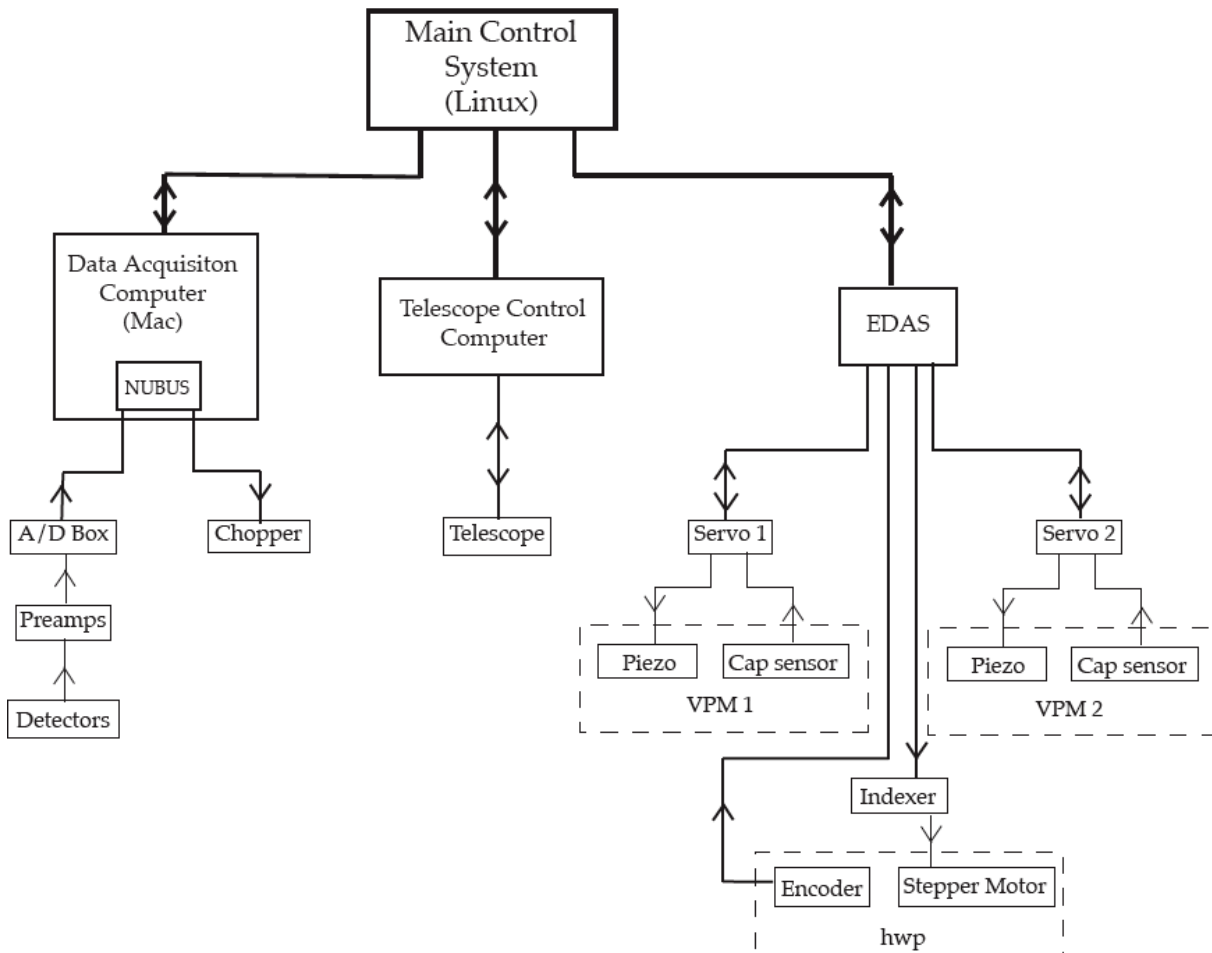
Figure 8.6. Diagram of the Hertz/VPM control electronics. Lines signify paths of communication between components; arrows signify direction. Main control computer communicates with three computers via TCP/IP connections. The data acquisition computer reads demodulated signals from detectors, synchronized by a chopping frequency sent to the secondary mirror. Telescope control computer operates telescope motion and positioning. EDAS controls both the VPMs and the Hertz HWP.

across the resistor is read by the AI module and is converted to a HWP angle via a simple

linear equation determined by previous measurements.

8.5. Laboratory Test Setup

Next we describe the setup we used to carry out testing of the Hertz/VPM polarimeter at Northwestern University. We simulated the telescope signal using a commercial blackbody source placed behind a rotating optical chopper. The blackbody was placed near the focal length of the first paraboloidal mirror. To facilitate the mounting and alignment of the blackbody, we removed the two periscope mirrors, replacing them with a flat mirror that kept the beam in the horizontal optics plane. A polarizing grid was placed between the blackbody and the chopper as needed. The grid was mounted on a rotating support, allowing us to vary the polarization state of the source. We rotated the grid to different angles corresponding to $\pm Q$ and $\pm U$ polarization states.

Some difficulty arose due to extraneous signals caused by the bolometer array viewing an image of itself reflected by the aluminum aperture plate of the blackbody. We were able to eliminate this effect by first rotating the blackbody, grid and chopper planes slightly from orthogonality to the beam, and then placing a new aperture, drilled from a piece of absorber, in front of the blackbody/grid/chopper system. The optics alignment achieved at Northwestern was not as accurate as for the SMTO tests. A careful laser alignment of the mirrors was carried out, but no cold load alignment was done. This may in part explain the measured efficiency of the system, as we discuss below.

As described above (Section 8.3), at SMTO we used an empirical procedure to determine the fixed HWP angle to be used for polarization measurements using dual-VPM modulators. Because this procedure was carried out before the relative gains f (Chapter 7) were determined, it was subject to significant uncertainties. Accordingly, for our lab measurements, we used a more accurate method. We rotated the calibration grid wires

to an angle 45° CCW from horizontal, or $-U$ input polarization. We collected HWP files (each modulator file consists of one cycle, as defined in Chapter 7) with VPM 2 set to a full wave delay, and with the VPM 1 grid removed. We then examined a plot of the polarization signal as a function of HWP angle. The location of the first peak equals the correct HWP angle. We measured this angle to be 80°, a difference of 16° from the previous setting (96°).

During lab testing in 2007, we collected many VPM files with the HWP set to the correct angle of 80°. Due to an inadvertent error, we also collected lab VPM files at a HWP angle of 68°. In Section 9.3 we will discuss how erroneous HWP angle settings affect our measurements.

8.6. Observations

To fully characterize the Hertz/VPM polarimeter, we took HWP and VPM files with different input sources (SgrB2, planets, blackbody source), either with or without a polarizing grid placed in the optics train. Data taken without polarizing grids were used to obtain photometry maps and instrumental polarization (IP) measurements. Data taken with a polarizing grid installed were used to characterize VPM performance and determine system polarization efficiency.

We present SMTO data collected only on the last night of the run (April 24), as it was the only night of the run with low atmospheric opacity ($\tau_{230\,GHz} \leq 0.06$) and stable observing conditions. Data taken in the lab were collected over a two week period in October 2007.

CHAPTER 9

Results

9.1. Photometry of Sagittarius B2

SgrB2 is a giant molecular cloud located 100 pc from the Galactic Center. Its dense cores are known to be centers of massive star formation; these regions have been mapped polarimetrically (Novak et al., 1997). Figure 9.1 shows a smoothed photometric map of SgrB2 taken with the Hertz/VPM polarimeter. Total integration time was 90 minutes (15 VPM files). The files were combined, correcting for changing parallactic angle. No flat-fielding was done. The fluxes are normalized to unity at the peak.

The map shows two peaks, separated by approximately 54″. This agrees with previous observations (Goldsmith et al., 1990). Based on the design of the system, we assume the beam size to be similar to that of Hertz at the CSO (20″) (Dowell et al., 1998). Given the relative faintness of the source, we consider our map to be evidence that our system has reasonable optical coupling.

9.2. VPM Interferograms and Asymmetry in Grid Performance

At the SMTO, we observed Saturn through a polarizing grid mounted horizontally with respect to the optics plane. We took HWP files with the VPMs set to various combinations of grid-mirror separation distances. The data were fit using a 2-VPM transfer function model (Chuss et al., 2006b). This model allowed us to fit for the source polarization, small offsets in the grid-mirror separation of each VPM, and rotational errors in the alignment
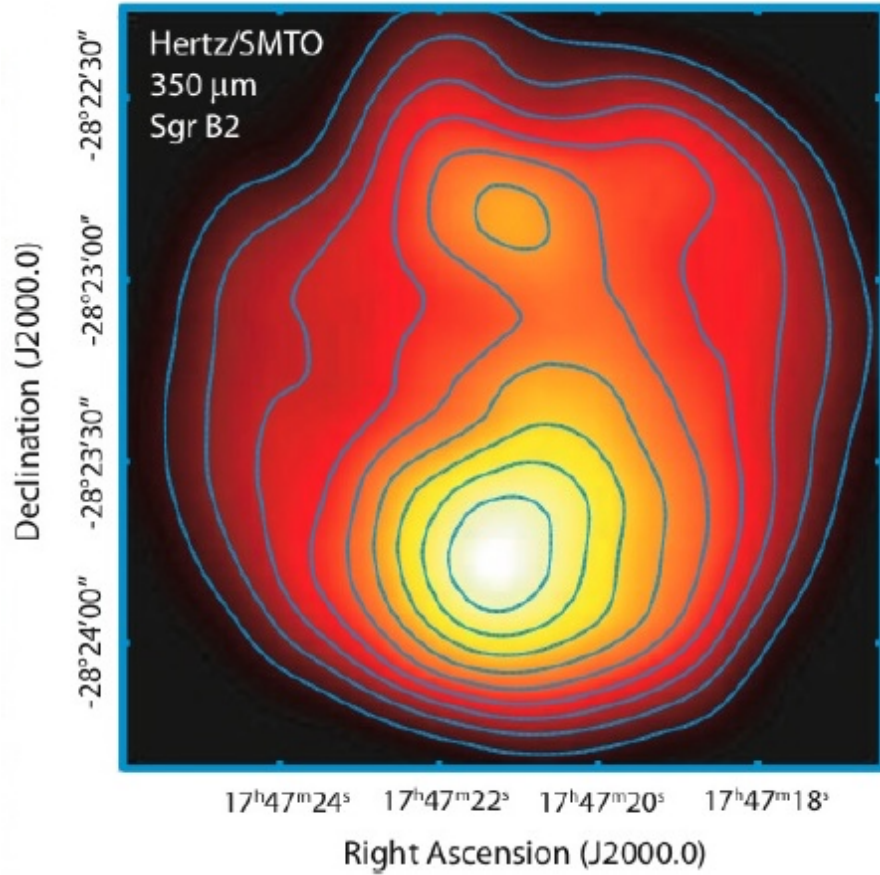
Figure 9.1. $350\,\mu$m photometric map of SgrB2, created from VPM files taken with the Hertz/dual-VPM polarimeter. Files were added and smoothed with no flat fielding. Two peaks are shown, $\sim 54''$ apart, which agree with previous results at this wavelength (Goldsmith et al., 1990). The beam size is $20''$.

of the VPM grids. Though the data exhibited the same qualitative features of the model, the apparent phase delays of the VPMs did not match the delays one expects given the geometry, wavelength and reported grid-mirror separation.

We isolated this problem in the lab by studying the polarization properties of a single VPM. Using the laboratory setup described earlier, we removed the grid from the front of VPM 1 and sent polarized light oriented -45° with respect to the horizontal axis $(-U)$

into VPM 2, whose grid axis is aligned horizontally to the optics plane. We then stepped the grid-mirror separation distance from 50 to 450 μm, roughly two full wavelength cycles of polarization modulation, acquiring a HWP file at each position.

For ideal grid performance and monochromatic radiation, we expect a unity-amplitude sine modulation of u with extrema located at the theoretical spacings (for $\lambda = 350\,\mu$m) of (n+ 1/2)*186 μm (VPM "on") and n*186 μm (VPM "off"). Figure 9.2 plots normalized Stokes u versus grid-mirror separation distance for VPM 2; each point plotted represents a HWP file taken at one VPM setting. The solid curve represents the theoretical performance of an ideal VPM, taking into account both the observed system efficiency and decoherence due to the finite bandwidth of the system (see Section 8.3). For illustrative purposes, we applied an arbitrary offset to align the curve with the first valley of the lab data. We notice an asymmetry between the ascending and descending portions of the curve. Although the separation between adjacent peaks (or adjacent valleys) is roughly 186 μm, the peak-valley separations are smaller than predicted. We also observe an efficiency well below unity; a discussion of possible causes of the observed efficiency is deferred until Section 9.3.

Models exist in the literature for wire grid performance. We have used the results of Houde et al. (2001) to attempt to reproduce the aforementioned asymmetry observed in our experimental results for the normalized Stokes u parameter as a function of the grid-mirror separation. We ran a simulation of the corresponding theoretical response of our VPM. The model used the wire radius a and spacing d of our experiment, and conductivity values σ that corresponded to aluminum-coated glass mirrors and gold plated wires (see Section 8.1).
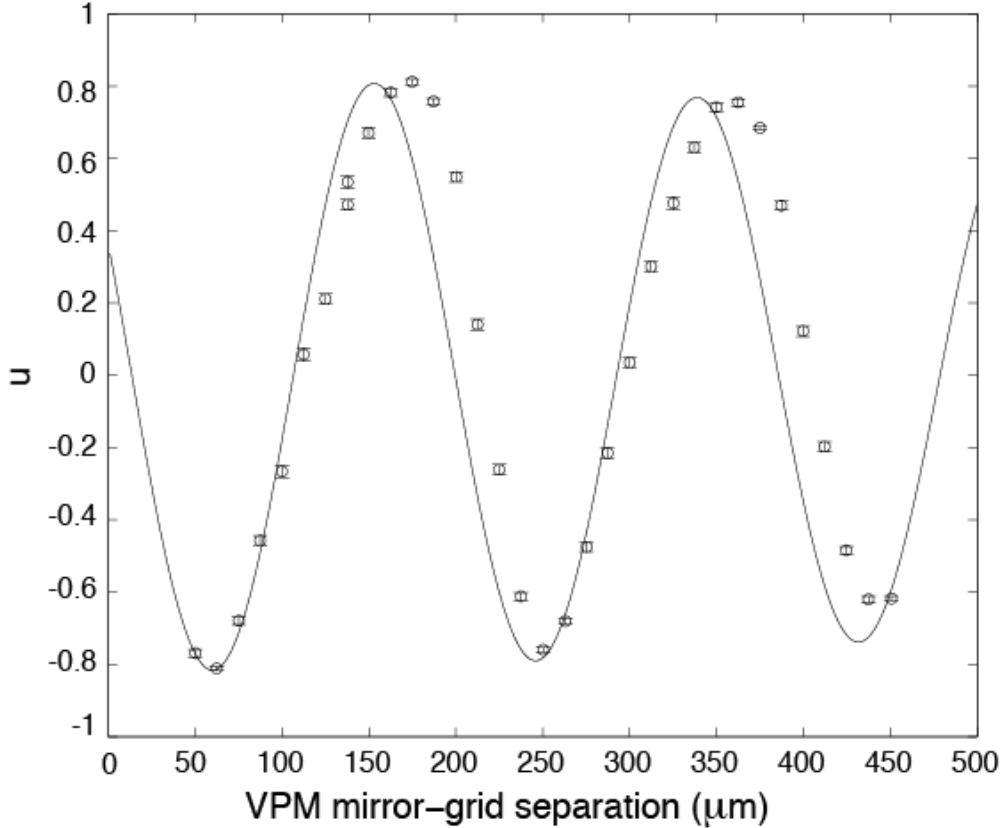
Figure 9.2. Interferogram plotting normalized Stokes parameter u versus mirror-grid separation for VPM 2. Input light is assumed to be 100% polarized at an angle of -45° with respect to the $+x$ axis (relative to VPM 2). The solid line is the signal expected for a geometric phase delay with a 10% bandwidth decoherence. This idealized curve has been modified to match the amplitude and phase of the first valley of the observed data. The data do not match this simple geometrically-motivated model; there is an asymmetry in the observed data, with the peak-valley separation distances being significantly different from 93 μm, the predicted value for ideal grids. A more detailed model that includes the phase response of the grid is required to reproduce the observed instrumental performance.

The dashed line in Figure 9.3 represents the behavior of an idealized grid that completely reflects light with polarization parallel to the grid and completely transmits light

polarized perpendicular to the grid. Note that this plot is consistent with a pure sinusoid. The solid line of Figure 9.3 shows the simulated plot of Stokes u versus grid-mirror separation distance for a narrow bandwidth "reflecting polarizer." Similar to the lab data, the model shows an asymmetry in the data curve. The difference between the ideal and predicted curves is a function of the grid parameters a and d and the operating wavelength, λ. Increasing the wavelength by a factor of 10 in the model eliminates the observed asymmetry. In our case, $\lambda/a = 350/12.5 = 28$. This is somewhat outside of the strict applicability of the model Houde et al. (2001) ($\lambda/a > 40$), which is the likely cause of the remaining discrepancy between the model and observed data. (We can ignore the spike at the maximum, which is a feature of the low bandwidth of this model, and is broadened out for Hertz/VPM.) However, the general trend is observed.

It is important to note that even though we find that the actual phase delay differs from the geometric prediction, the effect described here does not affect the utility of the VPM. It simply indicates that a more detailed model is required to map the grid-mirror separation into phase. For the purposes of this work, the interferogram in Figure 9.2 can be used to "tune" our VPMs. Our interferogram shows that, for the VPM grids used, operating at $350\,\mu$m, the peaks and valleys are not at the theoretical values of 93 and $186\,\mu$m. Presumably, adjustments to the mirror-grid separation distances so that the full- and half-wave conditions are met will increase the polarization efficiency of the system. After locating the proper full- and half-wave delays for VPM 2, we then set the device to a full-wave delay (i.e., turned "off"), and repeated the interferogram measurements, this time slowly stepping VPM 1. The proper half- and full-wave settings are $75\,\mu$m and $210\,\mu$m for VPM 1, and $62.5\,\mu$m and $175\,\mu$m for VPM 2. We took data both at these
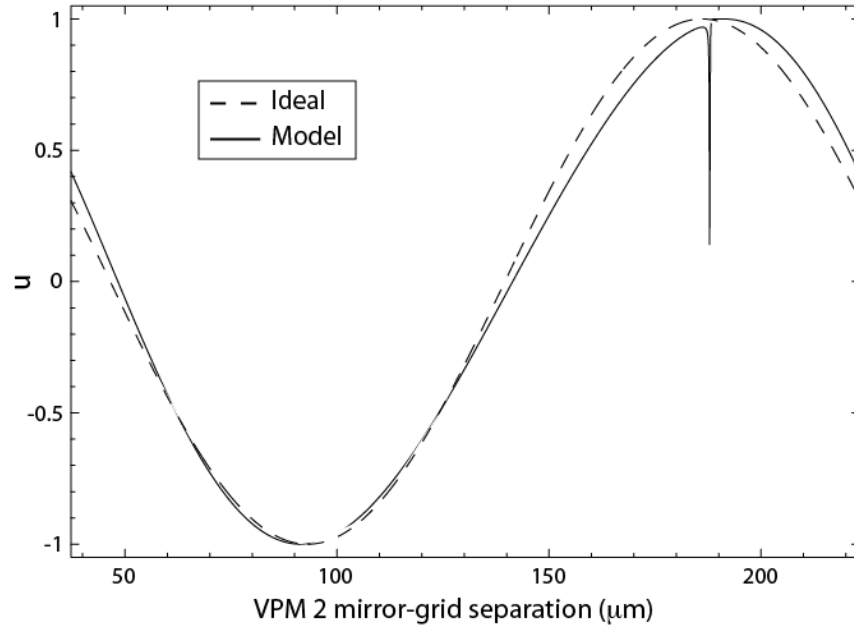
Figure 9.3. VPM Interferogram obtained using a model that treats wire grid performance (Houde et al., 2001). The solid curve shows the model predictions (u versus grid-mirror separation distance) for the case of grid parameters, wavelength, and incident polarization that match our experiment. The model employs a very narrow bandwidth and assumes regular wire spacing. The spike in the solid curve would be expected to be washed out by the large relative bandwidth of Hertz, and indeed is not observed in Fig. 9.2. The dashed curve shows the idealized sinusoidal interferogram that would be expected for the case of ideal grid and geometric phase delay. In the long wavelength limit, the model curve approaches the idealized curve.

observed separation distances and other settings related to the theoretical separations, which were later used for comparison.

9.3. Efficiency Measurements from Grid Tests

As suggested by the interferogram plot in the previous section, there are sources of polarization inefficiency in the experiment. We now discuss a series of grid measurements taken to isolate the causes of polarization efficiency losses.

Some sources can be found within Hertz; namely, its HWP and polarizing grid. In the lab, we collected HWP files taken with a polarizing source grid and with both VPM grids removed. We took files for four polarizing grid angles, corresponding to input polarization of $\pm q$ or $\pm u = -1$. With this configuration, we measured an average efficiency of 93%. Previous measurements for the Hertz polarimeter give an efficiency of 95% (Dowell et al., 1998); this drop of 2% may be attributable to the quality of the source polarizing grid, which has not been measured.

There are two main factors that contribute significantly to the efficiency measurements of the Hertz/dual-VPM system: the HWP offset angle setting and the VPM separation distance settings. We compare five groups of data from SMTO and lab data taken under three different conditions: incorrect HWP and VPM settings (groups 1-3 in the table), incorrect HWP setting and correct VPM settings (group 4), and correct HWP and VPM settings (group 5). The parameters for these groups are given in Table 9.1. There are three groups that fall under the first set of conditions listed above; two taken at SMTO and one in the lab. The determination of the HWP offset angle settings were discussed previously in Sections 8.3 and 8.5. We note that for group 2, the HWP angle is closer to (80-45 =) 35° than our proper offset angle of 80°; thus, our determination of Stokes q and u for this group is the opposite convention, as explained in Chapter 7. Also note that for

group 4, the difference between half and full wave delays was $93\,\mu$m, but the grid-mirror separations were offset from the theoretical $93/186\,\mu$m positions.

For SMTO grid data, we took nine VPM files (four for group 1, five for group 2) of Saturn with a polarizing grid installed before the first paraboloidal mirror. For each of these two groups, files were taken at one polarizing grid angle (horizontal wires, or $-Q$ input polarization). For the lab data, group 3 had six files taken at each of four polarizing grid angles ($\pm Q, \pm U$), while groups 4 and 5 had two files taken at each angle.

For each VPM file we calculated normalized Stokes q and u by the method outlined in Chapter 7. Figure 9.4 shows the input polarizations and the average efficiency for each group. In addition to plotting the efficiencies, we calculated the total efficiency for each group by averaging over all files in a group, regardless of whether that file was a measure of Q or U-like polarization. Averages were calculated with equal weighting and are listed in Table 9.1.

Figure 9.4 shows the efficiency measurements for incoming polarization at four different grid angles: $0°$ and $90°$ ($-Q$ and $+Q$ polarization), $45°$ and $135°$ ($-U$ and $+U$ polarization). Points that lie on the unit circle represent 100% input polarization, which we assume is the efficiency of the polarizing grid. As can be seen, an incorrect HWP or VPM position affects the polarization efficiency, which means that we can accept our Mt. Graham results with only a multiplicative adjustment to compensate. It is important to note, however, that there are variations in the polarization efficiency as one travels around the Stokes plane. For example, q polarization efficiency is higher than u efficiency for groups 3 and 5, but the reverse is true for group 4. This phenomenon is not fully understood; however, it is evident that using the proper modulator settings results in an

Table 9.1. Modulator Settings and Measured Efficiencies for Datafile Groupings

Group	HWP angle (°)	VPM1 delay (μm)		VPM2 delay (μm)		location	efficiency
		half	full	half	full		
1	96	93	186	93	186	SMTO	$54.3\% \pm 2.6\%$
2	51	93	186	93	186	SMTO	$53.8\% \pm 1.2\%$
3	68	100	193	82	175	lab	$47.7\% \pm 15.6\%$
4	68	75	210	62.5	175	lab	$52.3\% \pm 1.8\%$
5	80	75	210	62.5	175	lab	$85.7\% \pm 1.0\%$
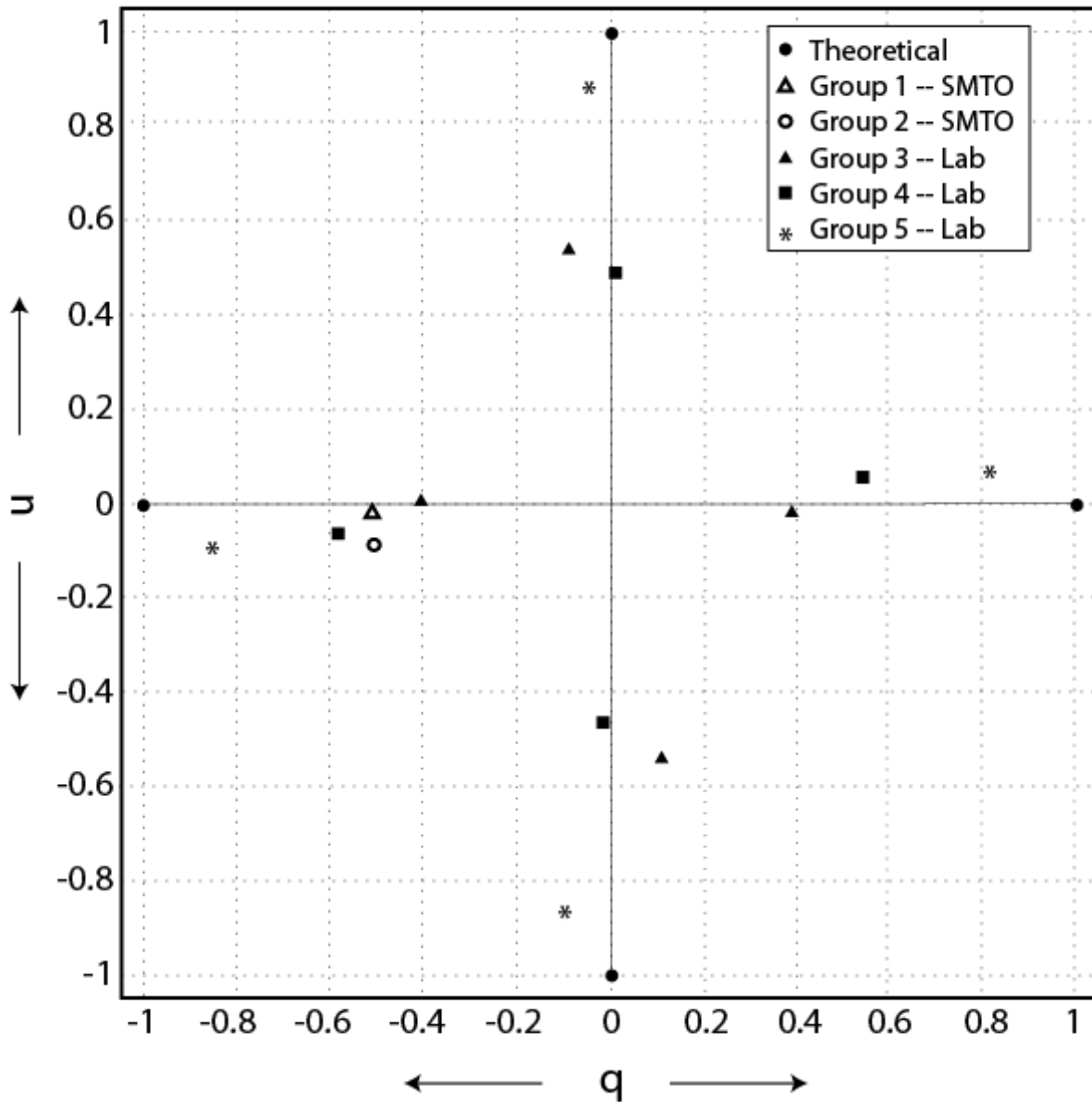
Figure 9.4. Polarization efficiency of Hertz/VPM polarimeter. Circles on axes represent 100% input polarization. Points plotted represent average values calculated for each group. In qu space, points are rotated away from axes; in real space, polarization angles are within 3° of theoretical values. Overall efficiencies increase as HWP and VPMs are moved to their proper settings. For group 2, $u \to -u$ and $q \to -q$, as described in Chapter 7 and Section 9.3

overall increase in polarization efficiency. The polarization efficiency ranges from 40% to a maximum of roughly 85% for group 5, where the HWP and VPMs are set to their optimal positions. Polarization efficiency at the SMTO (groups 1 and 2) was measured to be 54%.

Even when the VPMs are set to the proper half- and full-wave delays, we still see only a maxiumum efficiency of 85%; for perfect efficiency, we should expect a polarization closer to 93%. We do not know the cause of this net dual-VPM efficiency loss. Possible causes might include poor optical alignment in the lab or efficiency losses due to the polarizing grid, as mentioned above.

The polarization points do not line up along the axes, but rather appear rotated slightly about the origin. In physical space, all measured polarization angles are within 3° of the expected values. We believe this error to be due to cumulative alignment errors.

9.4. Instrumental Polarization

We observed Jupiter with no polarizing grid on the last night of observations at SMTO. The planet is assumed to be unpolarized (Clemens et al., 1990); hence any detected polarization should be attributed to the instrumental polarization (IP) of the full Hertz/VPM system. We collected 15 VPM files with settings the same as for group 1 of the efficiency measurements and 14 files with the settings of group 2.

Similar to the polarized grid files, we calculated the normalized q and u values for each VPM file. Averages were calculated for each group with equal weighting, and the q_{ave} and u_{ave} values were combined to give a percent polarization P and angle ϕ. We calculated raw values for q, u and P, then recalculated these values by a gain factor g of

$1/(polarization\ efficiency)$, with the polarization efficiency given by the values calculated in the previous section.

We measured raw IP values of $0.29 \pm 0.06\%$ and $0.28 \pm 0.1\%$ for groups 1 and 2, respectively. The polarization angles (ϕ) were -15 $\pm$ 6.6° and 4.8 $\pm$ 10.9° with respect to the optics plane. Multiplication by the appropriate gain factors gives adjusted IP values of $P = 0.54 \pm 0.1\%$ for group 1 and $P = 0.53 \pm 0.2\%$ for group 2.

Oblique reflections induce polarization oriented perpendicularly to the plane of incidence (Renbarger et al., 1998). For SMTO, this polarization should be dominated by the effects of the first three mirrors: the tertiary and two periscope mirrors. The latter have incident angles of 45°, and will each induce horizontal polarization with respect to the optics plane. Induced polarization from the tertiary will vary with the elevation angle of the object, but will have some component that will enter the VPM optics along the horizontal axis. Thus, it seems reasonable that this should cause, at least in part, the horizontal IP that we have measured.

An IP of less than 1% is comparable to that of many polarimeter systems currently or previously used, such as Hertz (Dowell et al., 1998). In the future, we hope to characterize the nature of the Hertz/VPM IP more thoroughly.

9.5. Summary

The dual-VPM system is an alternative to the commonly used HWP. This modulator, which operates in reflection with only small linear translations, is able to simulate the action of a rotating HWP. The inherent properties of the dual-VPM modulator provide

numerous benefits: high durability, easy multiwavelength operation, and capability of observing circularly polarized light.

Maximization of the dual-VPM system performance requires a full characterization of the performance of the grid-mirror system. The VPM grid properties, in particular wire diameter and spacing, are important contributing factors to whether or not the grid will act ideally for a particular wavelength. If wire grids are to be used at wavelengths shorter than those for which they are optimized, inteferograms can be used to determine proper spacing for half- and full-wave phase delays.

Despite these challenges, we found that the Hertz/dual-VPM polarimeter, as described above, operated with an instrumental polarization of less than 1%. Thus, the new device appears to be robust and is a competitive alternative for polarization modulation. They are a viable option for mm/submm/IR astronomy applications, including numerous experiments currently under development, including CMBpol and the HAWC polarimeter for SOFIA.

Part 3

Multiwavelength Polarimetry of T Tauri Stars

In Section 3.3 we discussed the basic steps of star formation, starting from a molecular cloud and finishing with a protostar and surrounding circumstellar disk. We now turn our attention to the disk itself, in an attempt to understand planet formation. As stated in the introduction, our motivation is to understand the very first stages of planet formation, namely, grain size growth in circumstellar disks (see also Section 3.4). In studying systems similar to that of our Sun, we hope to gain insight not only into planet formation for low-mass stars in general, but also for the specific case of our solar system.

We start with a presentation of the basic properties of class II evolutionary objects, T Tauri Stars (TTSs), in Chapter 10. In Chapter 11 we review simple toy models that we used to predict TTS polarization across the submillimeter band, and then we compare with more recent, more sophisticated models. In Chapter 12, we present the first $350\,\mu$m polarimetric observations of DG Tau, and we compare our results with a previous observation at $850\,\mu$m and with model predictions.

CHAPTER 10

Properties of T Tauri Stars

10.1. General Properties

T Tauri Stars (TTSs) are class II protostars (see Chapter 3) of masses $\leq 2 \, M_\odot$, often surrounded by an accretion envelope and a circumstellar disk of gas and dust (Stahler & Palla, 2004). The accretion envelope is decreased in density compared to earlier stages of star formation (class 0 and class I), making the protostar just visible at optical wavelengths. These objects are often noted for their large infrared excesses, due primarily to the dust disk.

T Tauri Stars can be organized into two main groups: classical T Tauri Stars (cTTSs), and weak-lined T Tauri Stars (wTTSs). Classical TTSs have relatively strong Hα emission, forbidden and other emission lines, and optical veiling of absorption lines. Weak-lined TTSs lack these properties, and can even lack an infrared excess; it is possible that wTTSs may actually be transitional or class III protostars; their (K-L) magnitudes, relative to cTTSs, suggest a similarity to main sequence stars. We continue our discussion only dealing with cTTS systems (although some statements may also be applicable to wTTSs).

A sample of TTS surveys gives an average age range of 10^5-10^6 years. Young TTSs have large optical jets that extend from the poles, that is, perpendicular to the plane of the disk. These outflows help remove excess angular momentum from the system, facilitating

further accretion onto the protostar (Testi et al., 2002). As TTSs evolve, however, the process of accretion slows down and their envelopes and optical jets diminish.

We now turn our attention to the disks surrounding T Tauri Stars, which are believed to be sites of planet formation. We discuss both photometric and polarimetric observations of these objects. The wealth of data collected has become the motivation for observing the polarization of these disks in the submillimeter regime.

10.2. Infrared-Radio Spectral Energy Distribution

As discussed previously in Section 3.3, the shape of the spectral energy distribution (SED) of a protostellar object can determine its stage of evolution. Furthermore, model fitting the infrared-radio SED data can constrain both the total mass of the disk and the sizes of the dust grains in the disk.

Information about the size of the grains can be determined from β, the *dust opacity index*. The dust opacity index is defined by:

$$\kappa_\nu \propto \nu^\beta \tag{10.1}$$

where ν is the frequency and κ_ν is the *particle mass opacity*, which is the ratio of the optical depth to the column density in g/cm^2. Hildebrand (1983) has shown observationally that for small, ISM-sized grains ($\sim 0.1\,\mu$m), $\beta \sim 2$ at submillimeter wavelengths, which is in accord with theoretical expectations (Beckwith et al., 2000). However, numerous surveys of TTS disks at these wavelengths (Beckwith & Sargent, 1991; Adams et al., 1990; Mannings & Emerson, 1994; Rodmann et al., 2006, see Figures 10.1 and 10.2) have
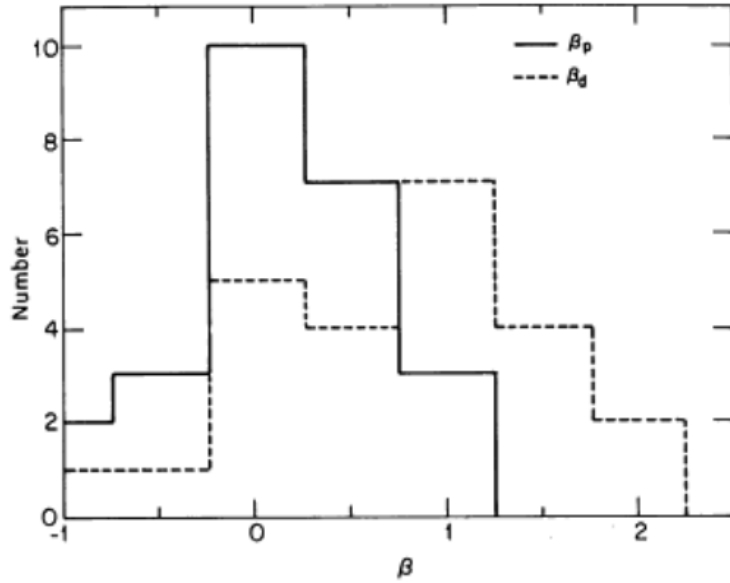
Figure 10.1. Survey of protostellar objects taken from Beckwith & Sargent (1991). Histogram plots number of protostars for each bin of opacity index β. As can be seen, most protostellar objects have $\beta < 2$, suggesting grains substantially larger than ISM-sized grains. Histograms are plotted for two methods of obtaining β: β_p represents a power-law fit to the far-IR SED, and β_d represents the result obtained from disk modeling.

found $\beta < 2$, which suggests that the grain size is increasing (Beckwith et al., 2000, and references therein). To understand why, note that κ_ν is proportional to Q_{abs} (Chapter 4). Like Q_{scatt}, the absorption efficiency decreases with λ for $\lambda \gtrsim a$ (section 4.2.1) but has a relatively flatter wavelength dependence for $\lambda < a$. Thus κ_ν itself will have a flatter wavelength dependence (lower β) for particles having sizes comparable to or larger than the wavelength.

Despite this evidence for large grains in TTS disk environments, the data are not definitive. There are two main methods used to calculate the dust opacity index. The
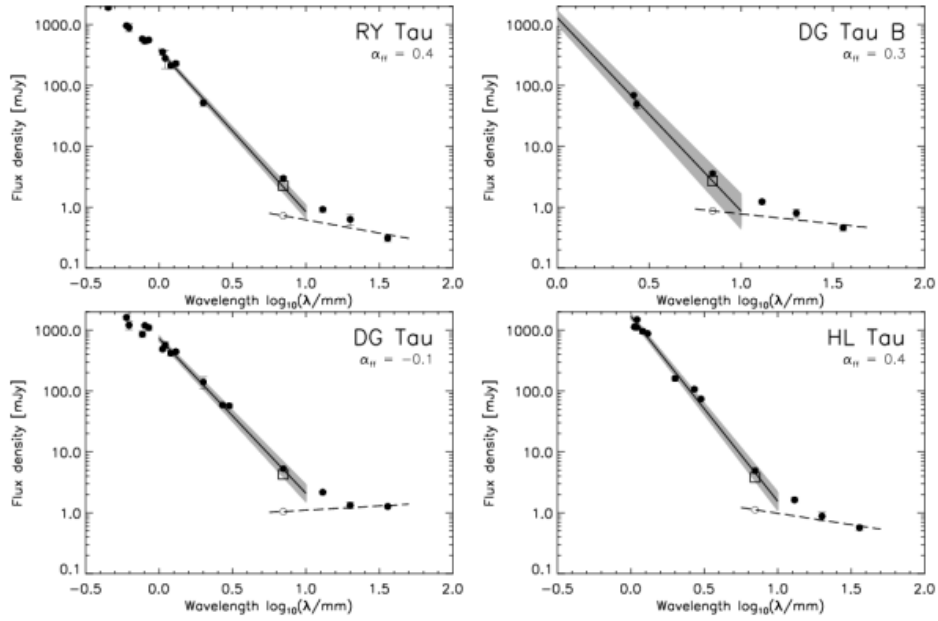
Figure 10.2. Plot from Rodmann et al. (2006) showing flux as a function of wavelength for various TTS systems. Line shows fit to data, with shaded region corresponding to error in slope. Points at longer wavelengths were used to determine the free-free contribution to the 7 mm flux, which was subtracted from that data point before determining the slope.

first is to obtain a power-law fit to the submm/mm flux data ($F_\nu \propto \nu^\alpha$). In the Rayleigh-Jeans limit, the flux of the disk is proportional to the particle mass opacity and the square of the frequency:

$$(10.2) \qquad\qquad F_\nu \propto \nu^2 \kappa_\nu$$

From before, $\kappa_\nu \propto \nu^\beta$, so setting this equal to the above gives $\beta = \alpha - 2$. However, this method works only for optically thin systems; if the optical depth τ of the disk is too

high, or the disk temperature too low, the predicted β will be underestimated (Beckwith & Sargent, 1991).

The second method used is to model the disk to match the observed SED (Figure 10.1). However, these models depend strongly on the optical depth of the disk, and contain degeneracies between optically thin and optically thick disks. Therefore, although the evidence for grain growth in these environments is compelling, it is not definitive. We look for another method to constrain grain size in the disks.

10.3. Polarimetry

Near-infrared spectropolarimetry has been used to determine characteristics of dust grains in circumstellar disks. In this wavelength regime, two polarization mechanisms are expected to dominate: selective extinction and scattering. Kobayashi et al. (1999) looked at three protostars at various stages of stellar evolution: L1551 IRS 5 (Class I), HL Tau (Class I-II transitional object), and T Tau (Class II, binary system).

By looking at the near-IR polarization spectra, they were able to determine how the spectrum changed with the evolving protostellar environment. For Class I protostars, the star itself is not directly visible in the optical; these objects tend to have a high (5-20%) and flat optical/near-IR polarization spectrum that is determined by the source geometry; scattering is the dominant polarization mechanism for these objects. However, there is also a prominent $3.1\,\mu$m polarization peak in the spectrum, corresponding to the ice-band absorption line; this polarization may be caused by selective extinction.

As the protostar evolves, the spectrum remains high and flat at optical wavelengths, but starts to decrease from the optical to the infrared. This is due to the star becoming

visible in the NIR, so the total flux is increasing relative to the polarized flux. Flux at longer wavelengths decreases still, as the total flux to polarized flux ratio continues to increase. At these wavelengths, the polarization is caused by selective extinction of the starlight by the dust grains in the disk. As the star becomes a later stage Class II object, the star becomes visible at all wavelengths in the optical/near-IR and polarization by scattering is no longer a major component of the observed polarization. Instead, polarization is caused by selective extinction of starlight.

Polarimetry of TTS disks in the millimeter and submillimeter wavebands has proved far more difficult. The first such measurements (for HL Tau and GG Tau at 1.1 and 0.8 mm) were nondetections (Tamura et al., 1995). Only one paper reporting polarization detections in the submillimeter has been published: Tamura et al. (1999) observed two TTS systems, DG Tau and GM Aur, using the SCU-POL $850\,\mu$m polarimeter at the James Clerk Maxwell Telescope (see Figure 10.3). They measured $\sim 3\%$ polarization for each disk, with the direction of polarization oriented perpendicular to the disk in both cases.

Previous studies of polarization at submillimeter wavelengths were for star-forming clouds, with polarization produced by thermally emitting aligned grains. Tamura et al. (1999) invoked this same mechanism as the cause of the polarization that they observed in DG Tau and GM Aur. Because polarization by thermal emission results in a polarization direction orthogonal to the magnetic field, they interpreted their result as indicative of a toroidal magnetic field. They did not consider alternative polarization mechanisms such as scattering or selective extinction (Section 4.2).
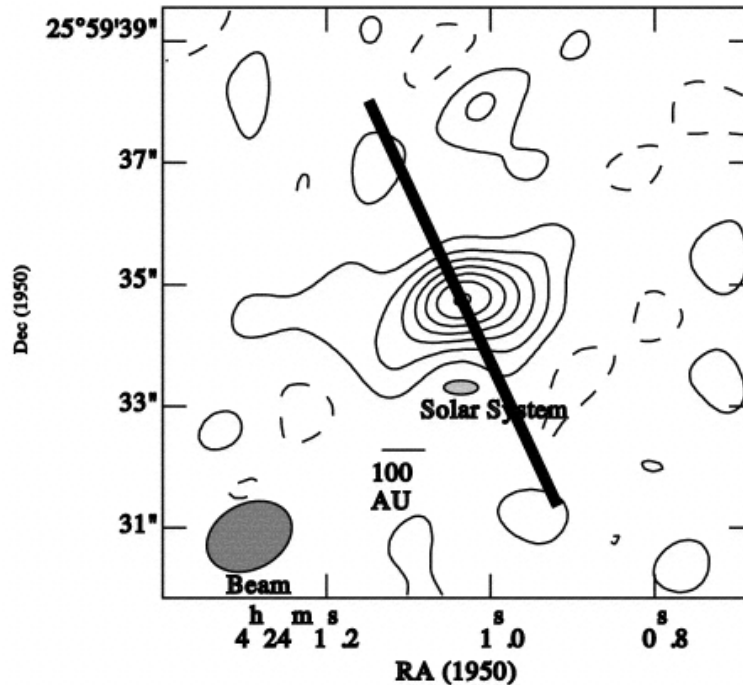
Figure 10.3. DG Tau polarimetery at 850μm by Tamura et al. (1999), taken with the SCUBA polarimeter. Polarization was measured to be roughly 3%, and is consistent with an orientation orthogonal to the disk. Result is superimposed over 2 mm continuum image; contour levels are -3, -1.5, 1.3, and 3σ, with a 1σ level of 11 mJy beam^{-1}. Superimposed images are from Kitamura et al. (1996).

In the next chapter, we will consider an alternative polarization mechanism that might explain the result of Tamura et al. (1999). We will also show that once the correct polarization mechanism is determined definitively via future observational and theoretical studies, the submm/mm polarization spectrum may provide strong constraints on grain size. Such observations will then provide a new way to probe these protoplanetary disks that will complement existing photometric and polarimetric studies. In Section 12.1, we present the first empirical information concerning the submillimeter polarization spectrum of a TTS source.

CHAPTER 11

Models for Dust Grains in Circumstellar Disks

Motivated by the Tamura et al. (1999) result, we want to know how much polarization we should expect to observe if the polarization of the disk emission were due to scattering rather than thermal emission. Note that the scattering hypothesis predicts polarization perpendicular to the disk, as observed. Beyond that, we wanted to determine the degree of polarization caused by each mechanism in a TTS disk, for wavelengths currently available for observations. Not only would these calculations determine the feasibility of polarization detections at these wavelengths, but, more importantly, if the shape of the polarization spectra were to depend on the polarization mechanism, this could provide an observational method of distinguishing between the two.

When we began our work, there were no available models for polarization of TTS disk emission. Thus, we developed toy models to obtain a basic understanding of polarization in protoplanetary disks. We first present these models, which were used to predict the amount of polarization likely to be seen in a protoplanetary disk across the submillimeter (and millimeter) waveband, as caused by large ($> 1\,\mu$m) dust grains in TTS disks. Later in this chapter we summarize current models that calculate more thoroughly the mechanism, magnitude and spatial distribution of the polarization.

11.1. Toy Models for Polarization by Scattering

Our first toy model (Krejny et al., 2006) was an attempt to estimate the polarization across the submm/mm spectrum as caused by scattering by large dust grains. We determined this by first calculating the fraction f of the thermal radiation from a typical grain scattered at least once before escaping the disk. We set the percent polarization P of this scattered light to 30%, or $P = 0.3f$. We assumed a uniform, cylindrical disk and estimated the scattered fraction as $f = 1 - e^{-\tau}$, where τ is the scattering optical depth computed for a line-of-sight passing through the disk and orthogonal to the plane of the disk:

$$\tau = nC_{sca}\Delta l \tag{11.1}$$

Here n is the number density of dust in the disk, C_{sca} is the scattering cross section (defined in Chapter 4), and Δl is the path length through the height of the disk. The scattering cross section is calculated from the efficiency, which we approximated using the $m = \infty$ plot from Figure 7.1 of Spitzer (1978), which assumes perfect scattering particles (i.e., no absorption). Figure 11.1 plots efficiency versus fractional wavelength for perfect scattering and a variety of particle types. We will use these curves again for additional models, described below.

The fraction of scattered light f calculated by the toy model overestimates the polarization for disks that have high optical depth. This is because for high τ a typical scatterer "sees" a more nearly isotropic illumination, and thus the scattered radiation has little net polarization. Certainly the polarization is reduced to levels far below the toy
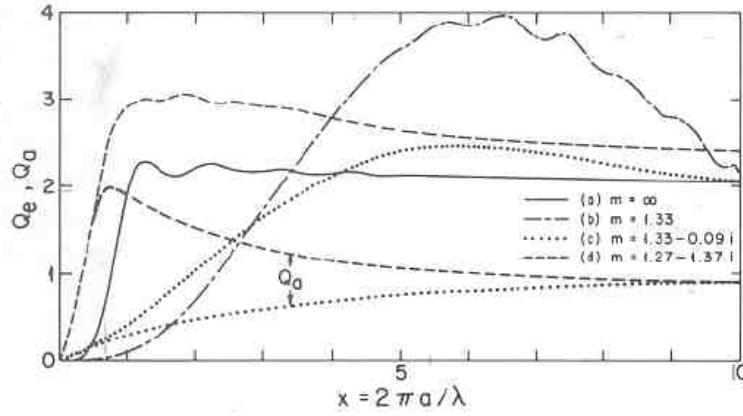
Figure 11.1. Extinction (Q_e) and absorption (Q_a) efficiencies as a function of inverse wavelength for dust grains of different complex refractive indices, from Spitzer (1978). Our toy models employ these curves. Scattering efficiency was calculated by subtracting Q_{abs} from Q_{ext}. The grains are spherical with radius a.

model value $0.3(1 - e^{-\tau})$. We simulated this effect by altering the P vs. τ curve such that, after the optical depth reaches unity, we let P drop linearly, reaching zero for $\tau = 2$.

$$
(11.2) \qquad P = \begin{cases} 0.3(1 - e^{-\tau}) & 0 < \tau < 1 \\ -0.1892\tau + 0.3784 & 1 < \tau < 2 \\ 0 & \tau > 2 \end{cases}
$$

The coefficients in the middle interval were chosen to make the function continuous at $\tau = 1$ and $\tau = 2$. In our model the spherical grains are of uniform size; we produce unique models for sizes varying between $0.1\,\mu$m to 1 cm. These are shown in Figure 11.2, where one sees that for a significant fraction of possible sizes we predict strong structure in the polarization spectrum. Although these models are not very realistic, they suggest

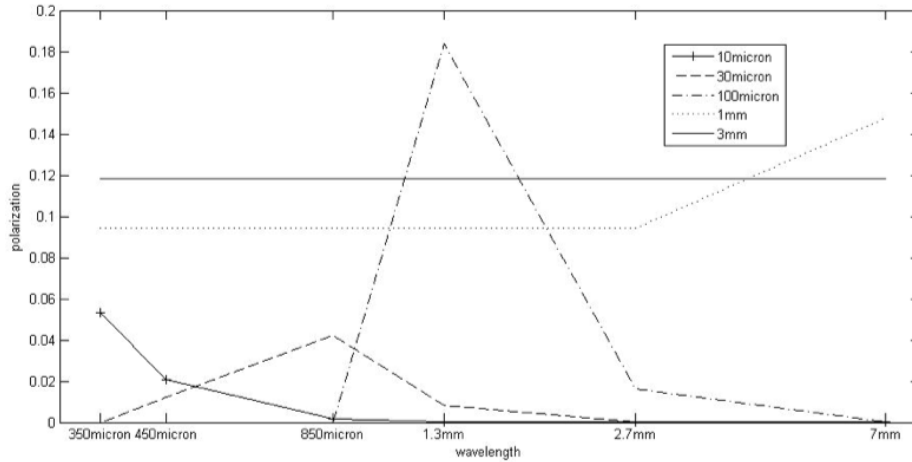Figure 11.2. Toy model predictions for polarization by scattering, with disk diameter $D = 200\,\mathrm{AU}$, gas and dust disk mass $M = 0.1\,\mathrm{M_\odot}$, and dust to gas mass ratio $A = 0.01$. Note that the assumed disk thickness does not affect the measured polarization for our model. Plots for different grain sizes are shown. We obtain wavelength dependent scattering efficiency data from a simple grain model (Spitzer, 1978, previous figure). At $850\,\mu$m, a degree of polarization similar to that seen by Tamura et al. (1999) can be produced by grain sizes larger than $10\,\mu$m. Note that although $3\,$mm grains produce a high, flat polarization spectrum, the other grain sizes all show structure in their respective polarization spectra.

that optical depth effects and polarization by scattering can give rise to characteristic polarization spectra that depend on particle size.

The wavelengths plotted in Figure 11.2 (and for the other toy models presented) represent the wavelengths available for observation with current telescopes that have sufficient sensitivity for these measurements. 350 and $450\,\mu$m are observable with the SHARP polarimeter (Li et al., 2008), $850\,\mu$m and $1.3\,$mm with the Submillimeter Array (SMA), and $7\,$mm at the Very Large Array (VLA). The $2.7\,$mm point is included for reference, and may soon be possible with CARMA.
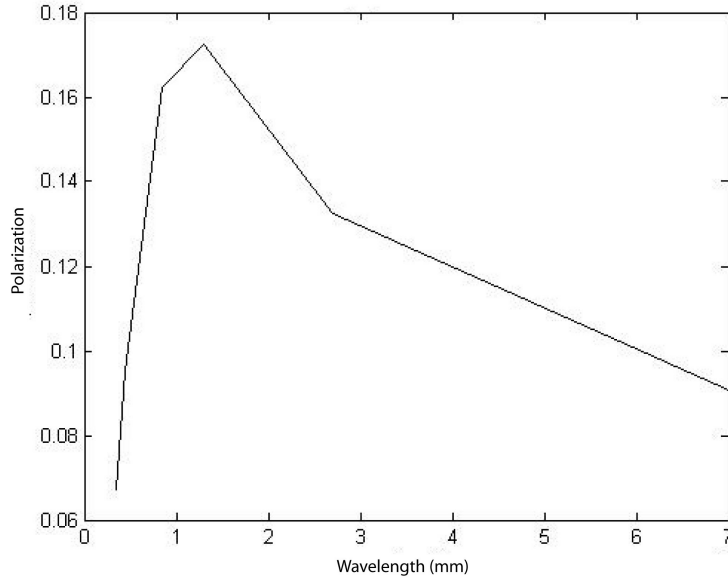
Figure 11.3. Polarization spectrum for a distribution of purely scattering grains ($m = \infty$). A peak is still seen in the spectrum, caused mostly by optical depth effects. The dust grain distribution is taken from Chiang et al. (2001).

For our next round of models, we incorporated a distribution of grain sizes as discussed in Chiang et al. (2001), having $N \sim r^{-3.5}$, where r is the grain radius. We included grain sizes ranging from $0.1\,\mu$m to $1\,$cm. The distribution is such that most of the surface area is tied up in the smaller grains, while most of the mass is in the larger grains. We implemented the grain size distribution by performing the following calculations for a series of bins, with each bin containing a range of sizes. The bins were distributed logarithmically. We used a number density of particles with radii between r and $(r + dr)$ as determined above, and then determined the mass of each bin, normalized to the total disk mass. The optical depth was then calculated for each bin. Finally, all of the τ values
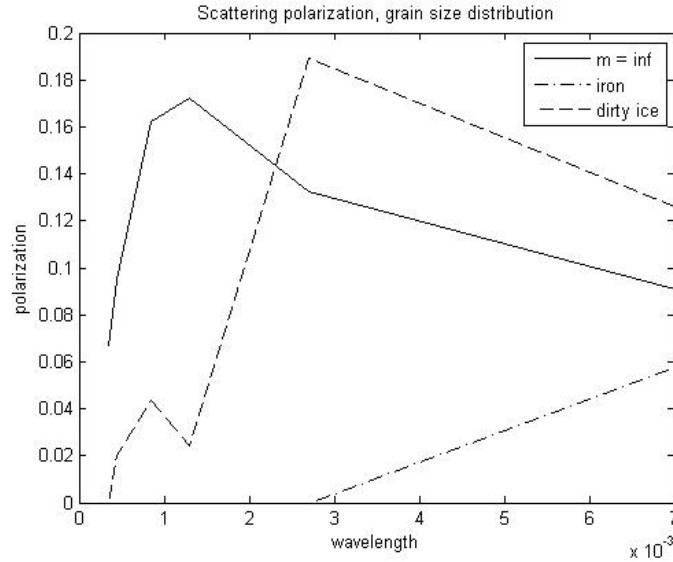
Figure 11.4. Polarization by scattering for both perfect scatterers ($m = \infty$ and grains with absorptive properties. Absorption acts to dampen polarization by scattering at shorter wavelengths. The secondary peak for dirty ice at $850\,\mu$m is due to artifacts of our scattering efficiency approximation, and should be ignored.

were added to determine the total optical depth for the disk. Looking at only purely reflective grains, we again found significant structure in the polarization spectrum (see Figure 11.3).

We then looked at different indices of refraction, such as $m = 1.27 - 1.37i$ ("iron") and $m = 1.33 - 0.09i$ ("dirty ice"). The scattering and absorption efficiencies were approximated by a series of straight line fits to several sections of the curves of Figure 11.1. The polarization was set to zero when the total absorption optical depth was found to exceed unity. This can have a major effect on the short-wavelength end of the polarization spectrum. Results are shown in Figure 11.4. However, significant structure remains in the polarization spectra, and for the case of "dirty ice", the mid-band peak was not lost.

11.2. Toy Model for Polarized Thermal Emission

Hildebrand et al. (1999) observes structure in the polarization spectrum below a factor of two, for small, thermally emitting aligned dust grains in the ISM. The observations by Hildebrand et al. (1999) were obtained for molecular cloud envelopes, which are optically thin. For extension to grain sizes and opacities expected for a circumstellar disk, we developed a toy model to predict polarization by large, thermally emitting aligned grains in a disk.

In this emission model (Figure 11.5), we obtained approximate absorption efficiencies for the grains along both long (r_l) and short (r_s) axes by calculating the efficiencies for two spherical grains, one with radius r_l and one with radius r_s. The long to short axis ratio was 1.2. The polarization was calculated as in Section 4.2.2, then halved to simulate spinning prolate grains. To avoid an unrealistically large line-of-sight optical depth, we set the disk inclination angle to $45\,^\circ$.

As seen in Figure 11.5, the polarization is strongly wavelength dependent. However, the shape of the graph lacks the characteristic polarization peak predicted by most of our scattering models. A comparison is shown in Figure 11.6.

These toy model results suggest that scattering can make a non-negligible contribution to the polarization observed in TTS disk emission. Furthermore, these results also suggest that it may be possible to (a) determine the dominant polarization mechanism in the disk, and (b) constrain the grain size, based on the shape of the polarization spectrum. These results were used by our group as the basis for two successful SHARP/CSO observing proposals. We always anticipated that more sophisticated models would be required to interpret our observations. Such a model is described in the following section.
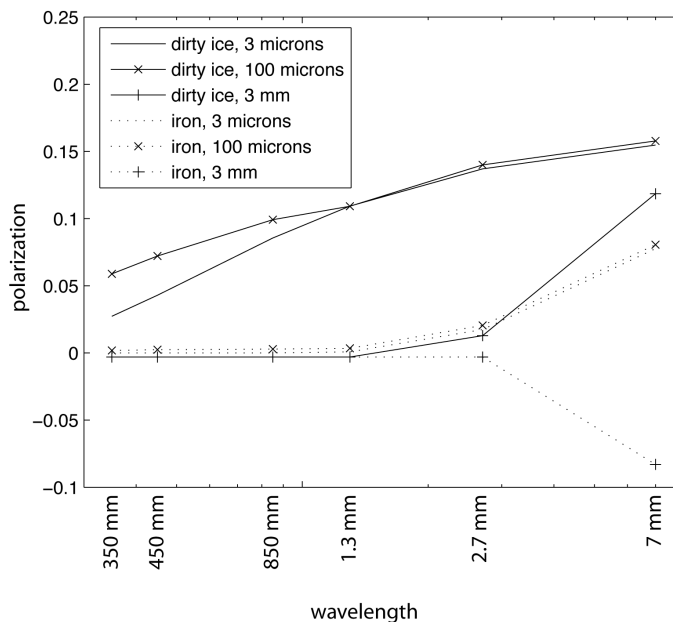
Figure 11.5. Spectrum predictions for polarization by thermally emitting large grains. Each curve represents a single size and type of dust grain; there is no grain size distribution. Polarization is calculated as in section 4.2.2, with the emission coefficients approximated for each axis of the grain by their spherical counterparts. Note that there is no peak in the polarization spectrum; rather, there is a gradual increase with increasing wavelength. The negative polarization point for 3 mm iron grains is due to a decrease in the emission efficiency, as approximated by the plot in Figure 11.1. Curves have slight vertical offset for clarity.

11.3. The Cho and Lazarian Model

The TTS disk model by Cho & Lazarian (2007) is the first published work to predict polarization by aligned grains in a protoplanetary disk for large grain radii. Their model was developed to achieve the following: 1) determine the size range of grains aligned by radiative torques and their location in the disk, 2) assuming alignment of all of the grains, calculate the polarization created by thermal emission, 3) determine how an unresolved disk and disk inclination affect the total polarization, and 4) determine the effects of
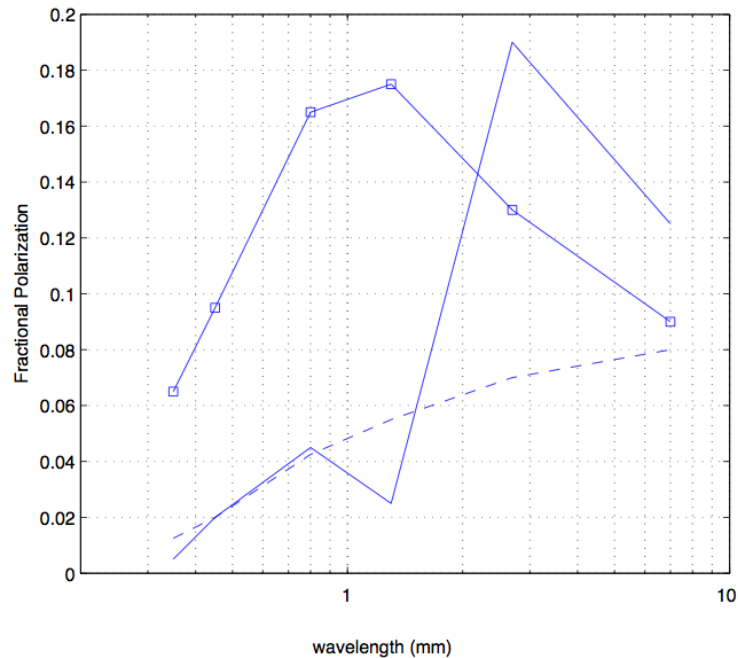
Figure 11.6. Toy model summary; shown are spectra for scattering (solid lines) and polarized emission (dashed line) from TTS disks. For scattering models, the grain size distribution is taken from the model of Chiang et al. (2001), which includes large grains. The emission model assumes relatively small grains of uniform size ($3\,\mu$m). For convenience, indices of refraction are taken from Spitzer (1978). Specifically, we used models a (solid line with boxes; purely scattering grains) and c (lines without boxes, solid and dashed; dirty ice); see Figure 11.1.

scattering on polarization. Before we discuss their results, we first present a summary of model parameters.

The disk is in hydrostatic and radiative equilibrium, and is permeated by a regular, toroidal magnetic field. The authors assume a flared disk that consists of two layers, a surface (on the top and bottom of the disk) and an interior. The surface is directly heated by the star, and the dust grains in the surface layer emit isotropically; half of the radiation escapes, the other half is emitted into the disk interior. The disk interior is

isothermal, and cooler than the disk surface. The surface grains radiate at a temperature that causes peak radiation at mid-IR wavelengths, while the interior grains radiate mostly in the far-IR/submm bands.

The overall grain size distribution for the disk ranges from 0.1-1000 μm, following the parameters of Mathis et al. (1977). The larger grains (up to 1000 μm) are found exclusively in the interior, while the surface grain sizes only reach 1 μm. The surface layer grains consist of silicates at small radii (< 6 AU), and silicates with ice beyond that radius. The interior features the same types of dust grains, but the ice boundary occurs at a much smaller radius (0.8 AU). The disk radius ranges from twice the stellar radius to 100 AU. The central star has a radius of 2.5 $R_\odot$, and temperature $T = 4000$ K. The disk height is four times the scale height.

11.3.1. Radiative Torques and Grain Alignment

Cho & Lazarian (2007) first determine the radiative torque efficiency Q_{RT} for large grains by scaling up previous efficiency results for smaller grains. The efficiency for small grains is given by:

$$(11.3) \qquad Q_{RT} \sim \begin{cases} O(1) & \lambda \sim a \\ (\lambda/a)^{-3} & \lambda > a \end{cases}$$

Since Cho & Lazarian are approximating the efficiencies for large grains, they conservatively set $Q_{RT} \propto 0.1$ when $\lambda \sim a$, and then have the alignment efficiency begin to decline when $a \geq 10\lambda$. Besides the wavelength of the incident radiation, other factors

that affect whether grains of a given radius are aligned or unaligned are the radiation intensity and the gas density.

With these approximations for the alignment efficiency, the authors were able to determine the size and distribution of aligned grains in the disk. No grains were aligned at $r < 1\,\mathrm{AU}$; at small radii, only the small surface grains were aligned. Large grains start to align at larger radii, and almost all grains are aligned at $r > 10\,\mathrm{AU}$.

11.3.2. Polarization of Thermally Emitting Aligned Grains

Cho & Lazarian (2007) next calculated the predicted polarization for a face-on disk with thermally emitting aligned grains when all of the grains are aligned. (The values obtained from the model were averages of polarization magnitude over the entire disk.)

Cho and Lazarian found that the following three properties affected the degree of polarization. First, when the grain size is small ($2\pi a/\lambda < 1$), polarization is due to thermal emission, as determined by their optical cross sections. The degree of polarization is given in terms of the emission efficiencies (Section 4.2.3):

$$P = (Q_{em,l} - Q_{em,s})/(Q_{em,l} + Q_{em,s}) \tag{11.4}$$

However, if the grain becomes too large ($2\pi a/\lambda > 1$), then polarization does *not* occur. This is because the ratio of the long and short optical cross sections ($C_{em,l}/C_{em,s}$) approaches unity. For example, when $\lambda = 850\,\mu\mathrm{m}$, that means that grains with $a > 100\,\mu\mathrm{m}$ do *not* contribute to the polarization, regardless of whether or not they are aligned.

Finally, increasing the optical depth of the disk reduces the net polarization. This is consistent with the disk tending to behave as a blackbody, as shown in Chapter 4. In the Cho and Lazarian model, the disk interior becomes optically thick for $\lambda < 100\,\mu$m, while the surface layer remains optically thin.

Because of the different temperatures of the disk surface and interior, each region dominates the polarization at different wavelengths. The hotter surface grains dominate the mid-IR polarization, while the interior dust grains dominate polarization in the FIR/submm. Also, as the wavelength increases, the polarization observed is created by dust grains at larger radii.

11.3.3. Resolution and Inclination Effects on Polarization

The above analysis assumes that the disk is resolved; however, current telescope sensitivities and angular resolutions are not sufficient to make resolved polarimetric measurements. Thus, Cho and Lazarian model the predicted net polarization for an unresolved disk at various inclination angles i (Figure 11.7). At $i = 90$, the interior of the disk is invisible because light from it is blocked by the outer part of the disk. For a face-on disk ($i = 0$), assuming a toroidal magnetic field and aligned, thermally emitting grains, the polarization across the disk will cancel to zero.

11.3.4. Polarization by Scattering

We limit our discussion to the first three paragraphs of the authors' discussion of polarization by scattering, as that is their only treatment of polarization in the far-IR/submm. It is known that Q_{sca} is very low when $2\pi a/\lambda \ll 1$, but this condition does not hold for
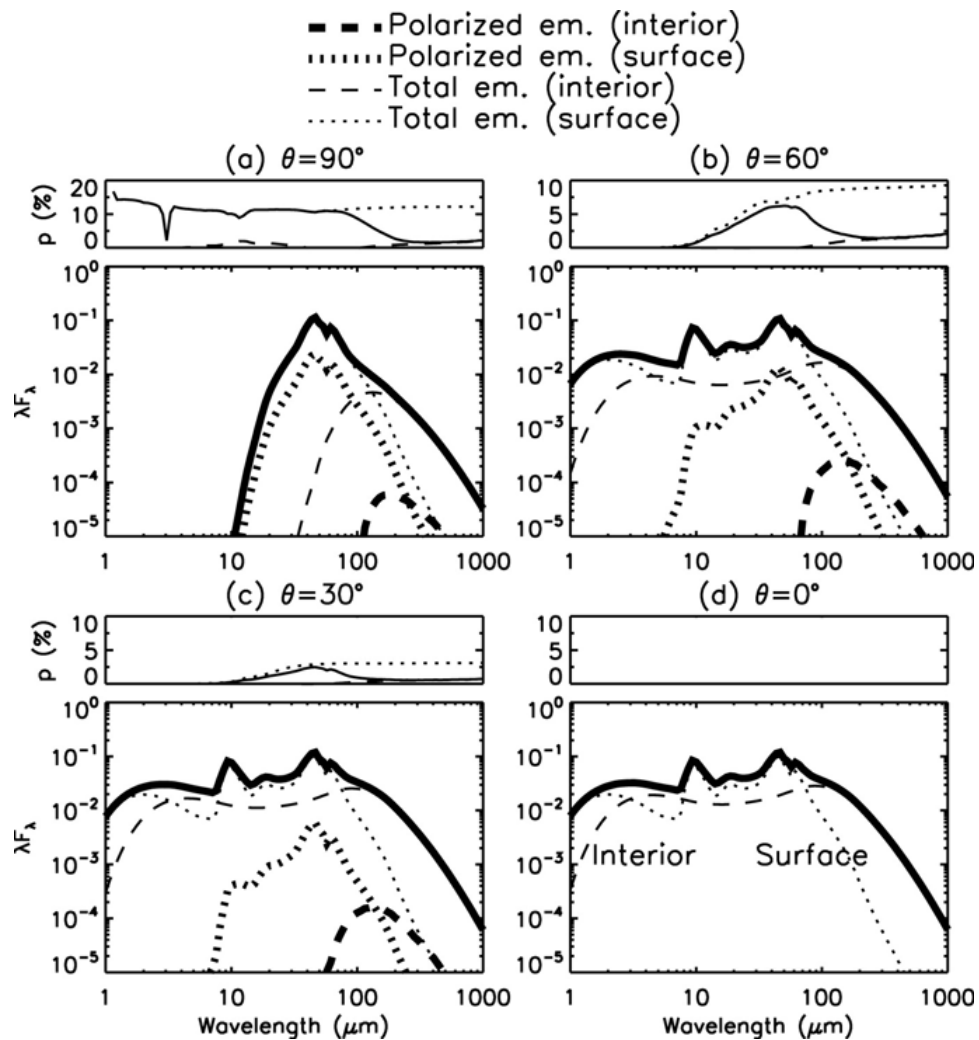
Figure 11.7. Cho & Lazarian (2007) model predictions for the polarization spectrum at four different disk inclination angles. The lower boxes plot polarized and total emission of the disk surface and interior, while the top box plots the degree of polarization. The total polarized emission is denoted by a thick solid black line, while the degree of polarization created by the entire disk (surface + interior) is denoted by a thin solid black line. As the inclination angle drops to 0°, the polarization spectrum reduces to zero, due to the cancellation of the radially symmetric polarization pattern in the disk.

large grains in the FIR/submm regime. Using the grain distribution given by Chiang et al. (2001), the authors tried to estimate whether polarization by scattering dominates polarization by thermal emission. In their calculation, they chose a point in the midplane of the disk, and calculated both the flux from thermally emitting dust grains $B_\lambda \kappa_{abs}$, and the scattered flux, $J_\lambda \kappa_{sca}$. The polarization for each mechanism is proportional to these quantities. Figure 11.8 plots the ratio of scattered flux to thermal emission as a function of disk radius. For submillimeter wavelengths, the ratio of scattered flux to emission is less than unity, except at small radii. However, results from Section 11.3.2 indicate that polarization at these wavelengths is dominated by the outer part of the disk. The authors thus conclude that polarization by scattering is not dominant.

This is the opposite of what was suggested by our toy models (Figure 11.6). However, the model of Cho & Lazarian (2007) is more sophisticated in disk structure and alignment efficiency calculations. Also, our toy model results were based on scattered light being 30% polarized, which is not always realistic.
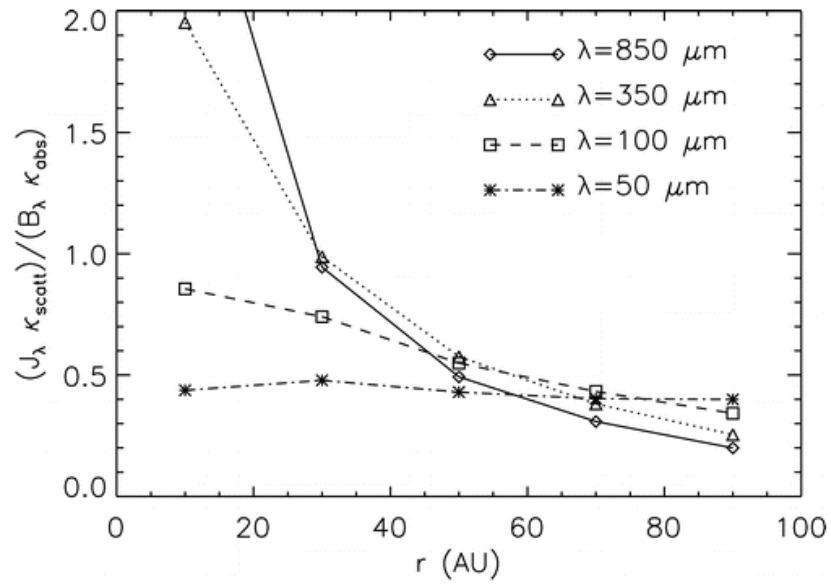
Figure 11.8. Comparison between polarization by scattering and emission, from Cho & Lazarian (2007). Values are plotted as a function of disk radius. Values less than unity signify that thermal emission dominates the flux seen. Values in the submillimeter ($\lambda = 350, 850\,\mu$m) are less than 1, except at the smallest radii. In Section 11.3.2, we learned that polarization at these wavelengths is dominated by the largest disk radii; we thus conclude that polarization by scattering is not dominant in this regime.

CHAPTER 12

Submillimeter Polarimetric Observations of TTS Disks

Our preliminary toy models suggested that polarization from scattering by large grains could produce observable percent-level polarizations and definite structure in the polarization spectrum. The more sophisticated Cho & Lazarian (2007) models suggest, on the contrary, that thermal emission is the dominant polarization mechanism in the submillimeter waveband. We now present two unresolved polarization observations of the T Tauri Star DG Tau. We will give a brief introduction to our observational program, and then describe the measurements and interpret them in the context of the Cho & Lazarian (2007) model.

12.1. Selection Criteria for TTS Targets

Several criteria were used to select objects for observation. Most importantly, the object had to be sufficiently bright across the entire submm/mm waveband. Due to sensitivity limitations of the three telescopes initially planned for our study (CSO, VLA, SMA), this dramatically reduced the number of viable candidates.

The main difficulty in finding high-flux TTSs to observe is that the older stars, having lost their accretion envelope, are significantly less bright. The object must also be without a large accretion envelope, since, for an unresolved object, this could confuse the source of polarization. If the TTS does have an accretion envelope, we must be able to rule the envelope out as a source of polarization at a given wavelength. Younger stars, such as

HL Tau, are brighter, but it becomes difficult to determine whether the flux is due to the accretion envelope or the disk itself.

Also, the disk could not be face-on; since we are unable to resolve the disk, a face-on disk would cause an average polarization of zero (for both emission by magnetically-aligned grains as well as scattering). Thus, we looked for disks that were edge-on or close to edge-on.

It was also necessary to eliminate binary systems; GG Tau was one such candidate; its two stars were surrounded by a circumbinary disk. Although this is an interesting system that deserves further study, we decided that it broadened the scope of our survey too much to be included at this time.

DG Tau is the only object that met all of our selection criteria. Observations show that DG Tau is sufficiently bright across all of the available wavelengths (Adams et al., 1990; Beckwith & Sargent, 1991; Rodmann et al., 2006). At 7 mm, there was concern that the flux may be contaminated by free-free emission. However, Rodmann et al. (2006) extrapolated from 6 cm data to show that the free-free emission at this wavelength is negligible. Also, despite the presence of a large accretion envelope, Tamura et al. (1999) were able to determine from a comparison of large and small beam 2 mm measurements that the 850 μm flux was also caused primarily by emission from the disk rather than from the envelope.

12.2. DG Tau

DG Tau is located in the Taurus-Auriga star formation cloud, at a distance of $d = 140$ pc (Beckwith et al., 1990). It has a mass of $0.6\,\mathrm{M_\odot}$ and luminosity of $1.7\,\mathrm{L_\odot}$. It is a

younger TTS, with an age of approximately 3 x 10^5 yr (Tamura et al., 1999). DG Tau has a prominent optical jet at PA = 226° (Mundt & Fried, 1983), and shows forbidden-line emission, making it a classical T Tauri Star.

Disk models created to reproduce the SED suggest a disk radius of 75 AU and mass of $0.03\,M_\odot$ (Kitamura et al., 1996). There is a large ^{13}CO gas disk with a major axis of $r \sim 1000$ AU, perpendicular to the optical jet (Kitamura et al., 1996). The dust disk has been measured at 2 mm (Kitamura et al., 1996) to have a radius of 109 ± 22 AU, at an inclination of 70° (with 90° signifying an edge-on disk). The dust disk is *not* orthogonal to the outflow axis; it is misaligned by almost 30°.

12.3. Observations and Analysis

We obtained polarization data for DG Tau at $350\,\mu$m using SHARP, our CSO polarimeter (see section 5.4). The resolution of SHARP at $350\,\mu$m is $\sim 9''$, which means that the disk is not resolved. Observations were made during February 12-14, August 9, and August 13, 2007. Table 12.1 lists observing information. DG Tau was observed in chop-nod mode, as described in Section 5.3. Data were collected in groups of dithers, with one dither consisting of four HWP cycles (see Chapter 7), each cycle having a slightly different pointing offset. Each cycle had a duration of eight minutes.

We use the (in-house designed) software programs SHARPINTEG and SHARPCOMBINE to analyze the data. SHARPINTEG carries out the "chop-nod" analysis. SHARPCOMBINE establishes its own grid, with pixel sizes that are half the size of the SHARC-II detector pixels (one "plot pixel" $= \sim 2.3'' \times 2.3''$). The SHARPINTEG data are aligned (to account for dithering and sky rotation) and plotted against this grid. For each point

Table 12.1. SHARP 350 μm Observations.

Date	Files Taken	τ range
Feb. 12, 2007	11	0.0332-0.0350
Feb. 13, 2007	26	0.0558-0.0661
Feb. 14, 2007	14	0.0623-0.0737
Aug. 9, 2007	4	0.0653-0.0658
Aug. 13, 2007	16	0.0467-0.0486

on the SHARPCOMBINE grid, SHARPCOMBINE smoothes and interpolates I, Q, and U values, using the SHARPINTEG output points lying near the given grid point. For this purpose, a smoothing kernael with Gaussian shape, $9''$ FWHM, and $9''$ diameter was used. For each of the three SHARPCOMBINE output maps, we set an annulus around the central star and a (straight) average was calculated over the annulus pixels. The inner radius of the annulus was chosen to be twice the kernel diameter; this ensured that data used for the central SHARPCOMBINE pixel would not contribute to any annulus pixel. The outer radius was chosen to give a total number of pixels that was 10 times that of the kernel; larger choices resulted in inclusion of parts of the SHARPCOMBINE map having lower sampling, resulting in larger noise levels. The annulus had a total sky coverage corresponding to that of one 12×12 subarray.

The "DC offsets" were then subtracted from the corresponding I, Q, and U values measured at the position of the source. Normalized Stokes parameters (q and u) were then calculated. Errors were propagated from the short-time-scale errors determined from each nod.

We note that a small amount of flux from the star, $\sim 2\%$, was found to be contaminating the annulus. However, this flux is consistent across all Stokes parameters. If only
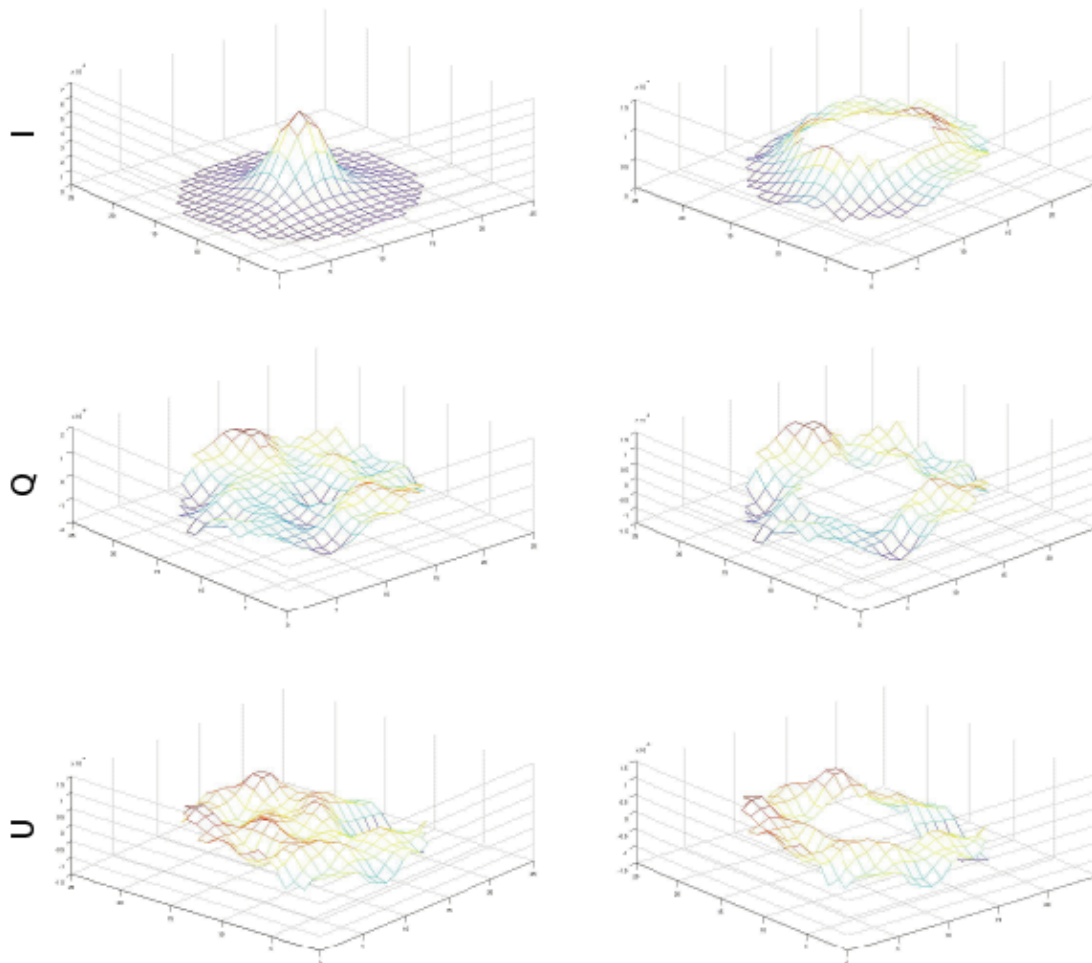
Figure 12.1. DG Tau Stokes maps and corresponding annuli for I, Q, and U. A straight average was calculated over each annulus and that value was subtracted the corresponding value measured at the position of the source. These new DC-offset subtracted values were then combined to calculate normalized Stokes q and u.

0.98 of the flux for each Stokes parameter remains after the DC offset subtraction, then this factor should cancel out upon determination of the normalized q and u.

We ran this process a second time, but with the data grouped into seven temporal bins. Again, Stokes maps were created and DC values derived from annuli were subtracted

from the maps for each of the bins. This was done in order to determine the reduced chi squared (χ^2_{red}) of the q and u data, and may be compared to results obtained without the DC offset subtraction. We found that the offset subtraction lowered χ^2_{red} from 1.5 and 1.6 to 0.9 and 0.8 (q and u, respectively).

The q and u values obtained via the two methods (averaging of all files vs. binning) are consistent. We adopt the values of the first method as our final result, which give $q = -0.0086 \pm 0.0060$ and $u = -0.0012 \pm 0.0061$.

12.4. Interpretation

The measured q and u values give a percent polarization of $P_{350\,\mu m} = 0.9 \pm 0.6\%$. This is not a detection, so we do not provide an angle determination. Tamura et al. (1999) report $850\,\mu$m polarization of $P_{850\,\mu m} = 2.95 \pm 0.89\%$. In comparison to the Tamura measurement, the percent polarization measurements agree within 2σ. However, if we look at the polarizations plotted in Stokes space, we find something more interesting.

Figure 12.2 plots the Tamura et al. (1999) $850\,\mu$m measurement together with our $350\,\mu$m measurement in Stokes space. The circles denote 1 and $2\,\sigma$ error bars. As can be seen in the plot, the Stokes parameters do not agree within $2\,\sigma$. The yellow portion of the plot represents the locus of points that are consistent with polarization oriented orthogonal to plane of the disk. The $850\,\mu$m point is consistent with polarization orthogonal to the disk, which Tamura et al. (1999) interpreted as due to thermally emitting dust grains aligned by a toroidal magnetic field. Our $350\,\mu$m measurement is barely consistent with this polarization orientation, and is consistent within 2σ with zero. If we assert, following Tamura et al. (1999) and Cho & Lazarian (2007) that the submillimeter polarization is
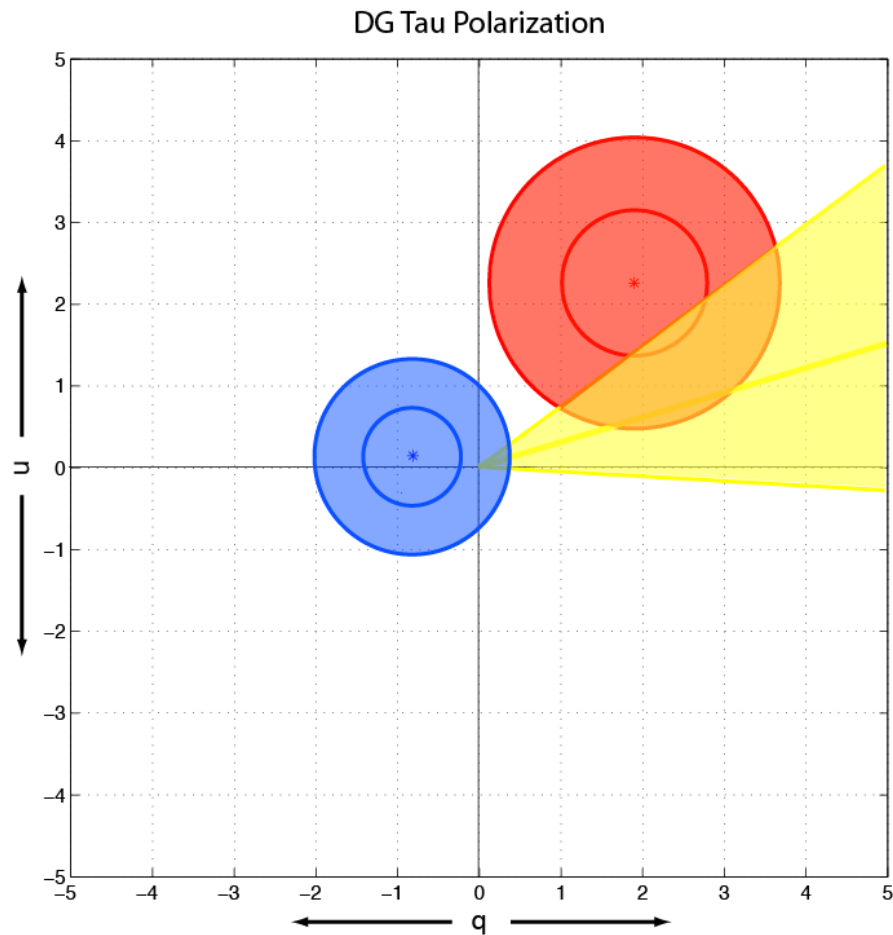
Figure 12.2. Plot in Stokes space of Tamura $850\,\mu$m polarization (red) and SHARP $350\,\mu$m measurement (blue). Stokes q and u and plotted in percent. Circles signify $1\,\sigma$ and $2\,\sigma$ errorbars. The two measurements do not agree within 2σ, which is highly suggestive that there is structure in the polarization spectrum. The yellow region denotes the locus of points that correspond to polarization orientated orthogonally to the plane of the disk (within PA errors). The $850\,\mu$m point appears consistent with this orientation; the $350\,\mu$m measurement is consistent with zero.

oriented perpendicular to the plane of the disk, then it is highly likely that we are seeing a substantial drop in the polarization from longer to shorter submillimeter wavelengths.

We compare this result to the submillimeter polarization spectrum predicted by Cho & Lazarian (2007) for an unresolved disk viewed at a 60° inclination angle (Figure 11.7, top right panels); this inclination angle is similar to that for DG Tau. Their model predicts a slight drop in percent polarization between the two wavelengths, but not to the extent that we have inferred.

We look for an explanation for the disagreement between the Cho and Lazarian model and the observations. One difference between the model and the actual disk is the disk mass; the model disk mass, taken from Chiang et al. (2001) is $M_d = 0.014\,M_\odot$, while the mass of the DG Tau disk lies in the range 0.02-0.06 $M_\odot$ (Kitamura et al., 1996; Beckwith & Sargent, 1991; Mannings & Emerson, 1994). Increasing the mass of a disk increases the optical depth along any line of sight through the disk. It was shown in Section 4.2.3 that as the optical depth increases, emission from dust grains in the back of the disk becomes selectively extincted by dust grains lying in front of them along the line of sight, a process we shall refer to as *polarization self suppression*, or PSS. We now try to determine if PSS is a significant effect in a TTS disk, and, more importantly, if PSS could affect the slope of the polarization spectrum in the $350\,\mu$m to $850\,\mu$m range.

To see a drop in polarization from $850\,\mu$m to $350\,\mu$m, the PSS effect should have a wavelength dependence. We recall in Section 10.2 that the frequency dependence of the mass opacity is $\kappa_\nu \propto \nu^\beta$. The mass opacity is defined as the optical depth divided by the mass column density along the line of sight:

$$(12.1) \qquad\qquad\qquad \kappa_\nu = \frac{\tau}{NL m_{particle}}$$

where N is the number density, L is the length of the cloud along the line of sight, and $m_{particle}$ is the average mass of a dust grain in the cloud. Since τ is the only quantity in the above equation that has any wavelength dependence, we conclude that $\tau \propto \nu^{\beta}$ as well.

For TTS disks, we have seen that β is often less than 2 in the submillimeter but is rarely, if ever, negative. This implies that, for a given line of sight and a given dust distribution, τ decreases with increasing wavelength. Thus, the PSS effect should be more significant for our $350\,\mu$m measurement than for $850\,\mu$m.

Now we must determine if PSS can create the factor of $\sim$ 2-3 drop in polarization that we have observed in the disk of DG Tau. It would be interesting to change the optical depth of the Cho & Lazarian (2007) model by increasing the disk mass to match that of DG Tau. Without rerunning their simulation, however, we can obtain some information about the PSS effect by looking through the model disk along different lines of sight.

Figure 12.3, taken from Cho & Lazarian (2007), plots the degree of polarization versus inclination angle for a selection of far-IR/submm wavelengths. This plot only considers polarization for the disk interior; for now we shall neglect the surface layer. We see that the ratio of 100 and $850\,\mu$m polarization (P_{100}/P_{850}) at an inclination $i = 70°$ is roughly $\frac{1}{7}$. It is reasonable to ask whether this large drop in polarization from $850\,\mu$m to $100\,\mu$m is caused by PSS, or is an intrinsic feature of the disk. In Section 11.3 we discussed the distribution of aligned grains in the disk; it is in principle possible that this drop in polarization could result from the fact that the grains that produce polarization at the shorter wavelength live in warmer regions closer to the star, and are thus less aligned and produce lower polarization.
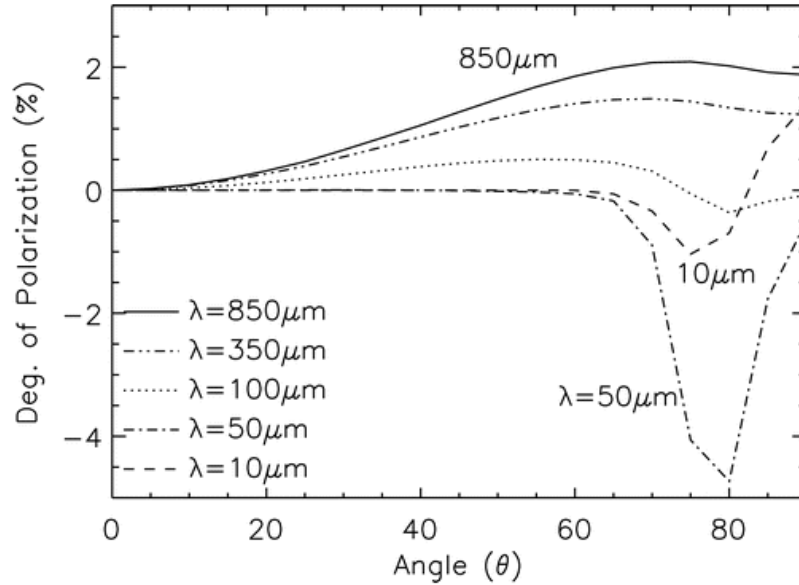
Figure 12.3. Cho and Lazarian (2007) model plot of percent polarization P versus inclination angle for selected wavelengths. Polarization is from disk interior only (interior dominates polarization in submillimeter waveband). The ratio of $(850\,\mu\text{m}/100\,\mu\text{m})$ polarization increases drastically with increasing viewing angle, while the ratio for $(850\,\mu\text{m}/350\,\mu\text{m})$ changes only slightly.

This issue is resolved when we compare the polarization ratio to values at lower inclinations. For $i = 30°$, $(P_{100}/P_{850}) \sim 1/3$. If the polarization were an intrinsic effect, then, for decreasing inclination angle, the polarization for each wavelength should decrease by an equal factor. This is because the polarization cancellation for an unresolved disk is worse for small inclination angles, and because this is a purely geometric effect, unrelated to optical depth. Thus, this polarization cancellation should affect the polarization observed at all wavelengths equally, and the polarization ratio should not change with inclination. However, we see that the ratio of polarization changes significantly with inclination angle.

We conclude that the significant change in polarization between $100\,\mu$m and $850\,\mu$m for $i = 70°$ (for the disk interior) is due in large part to PSS.

This effect is not as dramatic at longer wavelengths. The polarization ratio $850\,\mu$m$/350\,\mu$m is roughly 1.5 at $i = 70°$, but only decreases to 1.3 at $i = 30°$. This is presumably because PSS is less important for longer wavelengths. However, as discussed above, the disk mass used by Cho and Lazarian differs from the presumed DG Tau value by a factor of 1.4-4.0. If one were to repeat the work of Cho & Lazarian (2007) using a disk mass that is higher than the one they used by a factor in this range, it is plausible that the model would then predict a drop in polarization from $850\,\mu$m to $350\,\mu$m that is greater than a factor of two, thus matching the observations.

In the above arguments, we have neglected the surface layers, which do emit polarized light. However, for submillimeter wavelengths ($\lambda > 350\,\mu$m), the surface layers do not contribute significantly to the total polarization.

12.5. Summary

We presented toy models to predict polarization of T Tauri Star disk emission. These models suggest that polarization by scattering must be considered when modeling the predicted polarization detected in these objects. In contrast, the more sophisticated model of Cho & Lazarian (2007) indicates that thermal emission by aligned large grains, not scattering, is the dominant polarization mechanism.

We presented $350\,\mu$m polarimetry of DG Tau obtained using the SHARP polarimeter, and compared this to polarization previously measured at $850\,\mu$m. We find evidence for a drop in the polarization toward the shorter submillimeter wavelength. The magnitude of

this drop is larger than that predicted by the model of Cho & Lazarian (2007), but can be plausibly explained as an effect of the larger optical depth of DG Tau in comparison with the optical depth of the model disk. This conclusion suggests that submillimeter spectropolarimetry may provide an additional probe of optical depth in protoplanetary disks, which is related to grain size and planet formation.

Although polarization by scattering is now considered to be not dominant in this waveband, the modeling is at an early stage and it is possible that scattering may yet be partially responsible for the polarization structure that we observe. In the future, astronomers will obtain more polarization data at many different wavelengths, to fill in the spectrum, and these data should provide insight into both the grain size distribution and the polarization mechanism in the protoplanetary disk environment.

CHAPTER 13

Conclusions and Future Plans

Technology for submillimeter astronomy is undergoing a period of explosive growth. Bolometer systems are featuring larger arrays with more sensitive detectors. In the years ahead, interferometers will provide dramatic resolution and high sensitivities as well. Both types of telescopes are appearing in better locations, with dry air greatly reducing atmospheric noise effects. The operation of airborne observatories such as SOFIA will expand our capabilities to the otherwise unobservable far-infrared.

This thesis deals with two of the effects of these developments. First, as sensitivity and resolution increase, supporting technology in polarimetery must likewise improve, in durability, precision and multi-wavelength operation. The Hertz/VPM is a new development in the field of polarization modulation that aims to meet those requirements. Second, improvements in technology enable us to view fainter objects across the entire waveband. The study of relatively faint T Tauri Star disks has recently become possible on reasonable timescales, and polarization observations with instruments such as SHARP hint at the possibility of how submm/mm spectropolarimetry can probe the dust populations of these objects.

The Hertz/VPM polarimeter has been tested to characterize the dual-VPM system, a novel polarization modulator that operates in translation instead of rotation. The instrument was operated at $350\,\mu$m, both at the SMTO on Mt. Graham and in the lab at

Northwestern U. We find that the instrument operates with low instrumental polarization (IP) and a high efficiency.

In our characterization of the system, we discovered that the properties of the wire grids used for the VPMs (wire diameter and spacing) greatly influence the performance of the dual-VPM modulator. These properties cause a shift in the location of the proper half- and full-wave delays needed for polarization modulation. Despite this complication in the characterization of the device, compensation for this effect is easily achieved by locating the proper mirror-grid displacement settings using interferogram measurements. We discovered that measurements made at different VPM settings resulted in an overall loss in efficiency of the system. (A similar loss of efficiency was caused when the HWP located in the Hertz detector was rotated away from a configuration that properly aligned the detectors with the last VPM.)

Compiling efficiency data taken in the lab, we found that, with proper HWP settings and VPM separation distances (appropriate for our grids), the total efficiency of the system is 85%. This corresponds to a roughly 7% efficiency drop due to the dual-VPM system. Although a part of that drop may be caused by properties of the calibration grid, we consider the more likely cause to be a less accurate alignment of the optics train in the lab.

In the future, we plan to repeat efficiency and IP measurements in the lab at Northwestern, this time with more rigorous alignment. We also plan to return Hertz/VPM to Mt. Graham, but with new spectral filters, so that we can see how the same VPM grids perform at $850\,\mu$m. If the interferograms obtained show mirror-grid separation settings

to be closer to the theoretical calculations for this wavelength, this will confirm that grid properties are important to the operation of the instrument.

In this thesis, we presented $350\,\mu$m polarization data for the T Tauri Star DG Tau. TTSs are low mass protostars with prominent circumstellar disks that create an infrared "excess" in the stellar spectral energy distribution. SED modeling of the submm/mm slope is highly suggestive of grain growth, although the analysis is prone to the degeneracies of the models, mainly due to uncertainty of the optical depth of the disk.

The Tamura et al. (1999) $850\,\mu$m polarization measurement provided the motivation for spectropolarimetry as a method to probe the interiors of protoplanetary disks. By adding our $350\,\mu$m measurement, we present the first exploration of the submillimeter polarization spectrum of protoplanetary disk emission.

The toy models developed were a first attempt to try to predict polarization by scattering and thermal emission at these wavelengths. Although crude, they promoted the feasibility of observing polarization across the waveband, and were used to obtain observing time at the Caltech Submillimeter Observatory. We later turned to more sophisticated thermal emission and scattering models. Although the conclusion of these newer models was contrary to our toy models–namely, that thermal emission, and not scattering, was the dominant polarization mechanism at these wavelengths–the newer models still predicted polarization that matched the Tamura et al. (1999) measurement.

Although our $350\,\mu$m measurement is not a polarization detection, comparison with the $850\,\mu$m measurement in Stokes space strongly suggests significant structure in the polarization spectrum. Such structure is not evident in the Cho and Lazarian models. It is plausible, however, that if we were to increase the total disk mass in the model to

match that of DG Tau, we should be able to replicate the observed drop as an optical depth effect. In the future, spectropolarimetry of TTS disks could place constraints on the optical depth of the disks, and therefore could also place constraints on the grain size distribution in the disk.

We hope to use DG Tau observations to place constraints on future models. At this point, better models are needed. We note, however, that both the 350 and 850 μm data points were difficult measurements, and should be verified. Another way to confirm the slope of the polarization spectrum would be to observe DG Tau at 450 μm; if the measurements presented are correct, we would likely see a percent polarization that is intermediate between the two previous measurements. On a longer time scale, we wish to continue observations across the disk emission spectrum, which would include millimeter observations, to further constrain disk models.

References

Adams, F. C., Emerson, J. P., & Fuller, G. A. 1990, "Submillimeter photometry and disk masses of T Tauri disk systems," *ApJ*, **357**, 606.

Baars, J. W. M., Martin, R. N., Mangum, J. G., McMullin, J. P., & Peters, W. L. 1999, "The Heinrich Hertz Telescope and the Submillimeter Telescope Observatory," *PASP*, **111**, 627.

Barrière-Fouchet, L., Gonzalez, J.-F., Murray, J. R., Humble, R. J., & Maddison, S. T. 2005, "Dust distribution in protoplanetary disks. Vertical settling and radial migration," *A&A*, **443**, 185.

Battistelli, E. S., DePetris, M., Lamagna, L., Maoli, R., Melchiorri, F., Palladino, E., Savini, G., Mauskopf, P. D., & Orlando, A. 2003, "Far infrared polarimeter with very low instrumental polarization," in *Polarimetry in Astronomy. Edited by Silvano Fineschi . Proceedings of the SPIE, Volume 4843, pp. 241-249 (2003).*, ed. S. Fineschi, volume 4843 of *Presented at the Society of Photo-Optical Instrumentation Engineers (SPIE) Conference*, 241–249.

Beckwith, S. V. W., Henning, T., & Nakagawa, Y. 2000, "Dust Properties and Assembly of Large Particles in Protoplanetary Disks," *Protostars and Planets IV*, 533.

Beckwith, S. V. W. & Sargent, A. I. 1991, "Particle emissivity in circumstellar disks," *ApJ*, **381**, 250.

Beckwith, S. V. W., Sargent, A. I., Chini, R. S., & Guesten, R. 1990, "A survey for

circumstellar disks around young stellar objects," *AJ*, **99**, 924.

Carroll, B. W. & Ostlie, D. A. 1996, *An Introduction to Modern Astrophysics*, Addison-Wesley Publishing Company.

Cernicharo, J., Noriega-Crespo, A., Cesarsky, D., Lefloch, B., González-Alfonso, E., Najarro, F., Dartois, E., & Cabrit, S. 2000, "Windows Through the Dusty Disks Surrounding the Youngest Low-Mass Protostellar Objects," *Science*, **288**, 649.

Chandrasekhar, S. & Fermi, E. 1953, "Magnetic Fields in Spiral Arms." *ApJ*, **118**, 113.

Chiang, E. I., Joung, M. K., Creech-Eakman, M. J., Qi, C., Kessler, J. E., Blake, G. A., & van Dishoeck, E. F. 2001, "Spectral Energy Distributions of Passive T Tauri and Herbig Ae Disks: Grain Mineralogy, Parameter Dependences, and Comparison with Infrared Space Observatory LWS Observations," *ApJ*, **547**, 1077.

Cho, J. & Lazarian, A. 2007, "Grain Alignment and Polarized Emission from Magnetized T Tauri Disks," *ApJ*, **669**, 1085.

Chuss, D. T., Benford, D. J., Moseley, S. H., Staguhn, J. G., Voellmer, G. M., Wollack, E. J., Krejny, M., Novak, G., Drouet d'Aubigny, C. Y., Golish, D. R., Kulesa, C., Walker, C. K., & Loewenstein, R. F. 2006a, "The Hertz/SMT Submillimeter Polarimeter," in *Bulletin of the American Astronomical Society*, volume 38 of *Bulletin of the American Astronomical Society*, 1076–+.

Chuss, D. T., Wollack, E. J., Moseley, S. H., & Novak, G. 2006b, "Interferometric polarization control," *Appl. Opt.*, **45**, 5107.

Clemens, D. P., Kane, B. D., Leach, R. W., & Barvainis, R. 1990, "Millipol, a millimeter/submillimeter wavelength polarimeter - Instrument, operation, and calibration," *PASP*, **102**, 1064.

Crutcher, R. M. 2004, "What Drives Star Formation?" *Ap&SS*, **292**, 225.

Cudlip, W., Furniss, I., King, K. J., & Jennings, R. E. 1982, "Far infrared polarimetry of W51A and M42," *MNRAS*, **200**, 1169.

Davis, L. J. & Greenstein, J. L. 1951, "The Polarization of Starlight by Aligned Dust Grains." *ApJ*, **114**, 206.

Dolginov, A. Z. 1972, "Orientation of Interstellar and Interplanetary Grains," *Ap&SS*, **18**, 337.

Dominik, C., Blum, J., Cuzzi, J. N., & Wurm, G. 2007, "Growth of Dust as the Initial Step Toward Planet Formation," in *Protostars and Planets V*, eds. B. Reipurth, D. Jewitt, & K. Keil, 783–800.

Dowell, C. D., Allen, C. A., Babu, R. S., Freund, M. M., Gardner, M., Groseth, J., Jhabvala, M. D., Kovacs, A., Lis, D. C., Moseley, Jr., S. H., Phillips, T. G., Silverberg, R. F., Voellmer, G. M., & Yoshida, H. 2003, "SHARC II: a Caltech submillimeter observatory facility camera with 384 pixels," in *Millimeter and Submillimeter Detectors for Astronomy. Edited by Phillips, Thomas G.; Zmuidzinas, Jonas. Proceedings of the SPIE, Volume 4855, pp. 73-87 (2003).*, eds. T. G. Phillips & J. Zmuidzinas, volume 4855 of *Presented at the Society of Photo-Optical Instrumentation Engineers (SPIE) Conference*, 73–87.

Dowell, C. D., Hildebrand, R. H., Schleuning, D. A., Vaillancourt, J. E., Dotson, J. L., Novak, G., Renbarger, T., & Houde, M. 1998, "Submillimeter Array Polarimetry with Hertz," *ApJ*, **504**, 588.

Draine, B. T. & Weingartner, J. C. 1996, "Radiative Torques on Interstellar Grains. I. Superthermal Spin-up," *ApJ*, **470**, 551.

Goldsmith, P. F., Lis, D. C., Hills, R., & Lasenby, J. 1990, "High angular resolution submillimeter observations of Sagittarius B2," *ApJ*, **350**, 186.

Hall, J. S. 1949, "Observations of the Polarized Light from Stars," *Science*, **109**, 166.

Hecht, E. 1998, *Optics*, Addison-Wesley Publishing Company, third edition.

Hildebrand, R. H. 1983, "The Determination of Cloud Masses and Dust Characteristics from Submillimetre Thermal Emission," *QJRAS*, **24**, 267.

— 1988, "Magnetic fields and stardust," *QJRAS*, **29**, 327.

Hildebrand, R. H., Davidson, J. A., Dotson, J. L., Dowell, C. D., Novak, G., & Vaillancourt, J. E. 2000, "A Primer on Far-Infrared Polarimetry," *PASP*, **112**, 1215.

Hildebrand, R. H., Dotson, J. L., Dowell, C. D., Schleuning, D. A., & Vaillancourt, J. E. 1999, "The Far-Infrared Polarization Spectrum: First Results and Analysis," *ApJ*, **516**, 834.

Hildebrand, R. H., Dragovan, M., & Novak, G. 1984, "Detection of submillimeter polarization in the Orion nebula," *ApJ*, **284**, L51.

Hiltner, W. A. 1949, "Polarization of Light from Distant Stars by Interstellar Medium," *Science*, **109**, 165.

Houde, M., Akeson, R. L., Carlstrom, J. E., Lamb, J. W., Schleuning, D. A., & Woody, D. P. 2001, "Polarizing Grids, Their Assemblies, and Beams of Radiation," *PASP*, **113**, 622.

Jackson, J. D. 1999, *Classical Electrodynamics*, John Wiley & Sons, third edition.

Johansen, A., Oishi, J. S., Low, M.-M. M., Klahr, H., Henning, T., & Youdin, A. 2007, "Rapid planetesimal formation in turbulent circumstellar disks," *Nature*, **448**, 1022.

Joyce, R. R. & Simon, T. 1986, "Polarimetry of the infrared reflection nebulae in Cepheus A and S140," *AJ*, **91**, 113.

eds. Karttunen, H., Kroger, P., Oja, H., Poutanen, M., & Donner, K. J. 1996, *Fundamental Astronomy*, Springer, third edition.

Kitamura, Y., Kawabe, R., & Saito, M. 1996, "Imaging of the Compact Dust Disk around DG Tauri with 1 Resolution," *ApJ*, **465**, L137+.

Kobayashi, N., Nagata, T., Tamura, M., Takeuchi, T., H., Kobayashi, Y., & Sato, S. 1999, "Near-Infrared Spectropolarimetry of Three Prototype Low-Mass Young Stellar Objects in the Taurus Dark C loud," *ApJ*, **517**, 256.

Kokubo, E. & Ida, S. 1998, "Oligarchic Growth of Protoplanets," *Icarus*, **131**, 171.

Krejny, M., Chuss, D. T., Novak, G., Voellmer, G. M., Wollack, E. J., Walker, C. K., Jackson, M., Benford, D. J., Staguhn, J. G., Moseley, Jr., S. H., Kulesa, C., Drouet d'Aubigny, C. Y., Golish, D. R., & Loewenstein, R. F. 2006, "The variable-delay polarization modulator," in *Millimeter and Submillimeter Detectors and Instrumentation for Astronomy III. Edited by Zmuidzinas, Jonas; Holland, Wayne S.; Withington, Stafford; Duncan, William D.. Proceedings of the SPIE, Volume 6275, pp. 62751N (2006).*, volume 6275 of *Presented at the Society of Photo-Optical Instrumentation Engineers (SPIE) Conference*.

Lane, A. P. 1998, "Submillimeter Transmission at South Pole," in *Astrophysics From Antarctica*, eds. G. Novak & R. Landsberg, volume 141 of *Astronomical Society of the Pacific Conference Series*, 289–+.

Lazarian, A. 2000, "Physics of Grain Alignment," in *Cosmic Evolution and Galaxy Formation: Structure, Interactions, and Feedback*, eds. J. Franco, L. Terlevich, O. López-Cruz,

& I. Aretxaga, volume 215 of *Astronomical Society of the Pacific Conference Series*, 69–+.

— 2007, "Tracing magnetic fields with aligned grains," *Journal of Quantitative Spectroscopy and Radiative Transfer*, **106**, 225.

Li, H., Dowell, C. D., Kirby, L., Novak, G., & Vaillancourt, J. E. 2008, "Design and initial performance of SHARP, a polarimeter for the SHARC-II camera at the Caltech Submillimeter Observatory," *Appl. Opt.*, **47**, 422. URL http://ao.osa.org/abstract.cfm?URI=ao-47-3-422.

Li, H., Griffin, G. S., Krejny, M., Novak, G., Loewenstein, R. F., Newcomb, M. G., Calisse, P. G., & Chuss, D. T. 2006, "Results of SPARO 2003: Mapping Magnetic Fields in Giant Molecular Clouds," *ApJ*, **648**, 340.

Lissauer, J. J. & Stevenson, D. J. 2007, "Formation of Giant Planets," in *Protostars and Planets V*, eds. B. Reipurth, D. Jewitt, & K. Keil, 591–606.

Mannings, V. & Emerson, J. P. 1994, "Dust in discs around T Tauri stars: Grain growth?" *MNRAS*, **267**, 361.

Mathis, J. S., Rumpl, W., & Nordsieck, K. H. 1977, "The size distribution of interstellar grains," *ApJ*, **217**, 425.

Mundt, R. & Fried, J. W. 1983, "Jets from young stars," *ApJ*, **274**, L83.

Natta, A., Testi, L., Calvet, N., Henning, T., Waters, R., & Wilner, D. 2007, "Dust in Protoplanetary Disks: Properties and Evolution," in *Protostars and Planets V*, eds. B. Reipurth, D. Jewitt, & K. Keil, 767–781.

Novak, G., Dotson, J. L., Dowell, C. D., Goldsmith, P. F., Hildebrand, R. H., Platt, S. R., & Schleuning, D. A. 1997, "Polarized Far-Infrared Emission from the Core and

Envelope of the Sagittarius B2 Molecular Cloud," *ApJ*, **487**, 320.

Phillips, T. 1997, "Recent Results from the Caltech Submillimeter Observatory," in *The Far Infrared and Submillimetre Universe.*, ed. A. Wilson, volume 401 of *ESA Special Publication*, 223–+.

Platt, S. R., Hildebrand, R. H., Pernic, R. J., Davidson, J. A., & Novak, G. 1991, "100-micron array polarimetry from the Kuiper Airborne Observatory - Instrumentation, techniques, and first results," *PASP*, **103**, 1193.

Purcell, E. M. 1979, "Suprathermal rotation of interstellar grains," *ApJ*, **231**, 404.

Renbarger, T., Dotson, J. L., & Novak, G. 1998, "Measurements of Submillimeter Polarization Induced by Oblique Reflection from Aluminum Alloy," *Appl. Opt.*, **37**, 6643.

Rodmann, J., Henning, T., Chandler, C. J., Mundy, L. G., & Wilner, D. J. 2006, "Large dust particles in disks around T Tauri stars," *A&A*, **446**, 211.

Schleuning, D. A., Dowell, C. D., Hildebrand, R. H., Platt, S. R., & Novak, G. 1997, "HERTZ, A Submillimeter Polarimeter," *PASP*, **109**, 307.

Schmidt, G. D., Angel, J. R. P., & Beaver, E. A. 1978, "Photoelectric polarization maps of two bipolar reflection nebulae," *ApJ*, **219**, 477.

Shinnaga, H., Tsuboi, M., & Kasuga, T. 1999, "A Millimeter Polarimeter for the 45-m Telescope at Nobeyama," , **51**, 175.

Shu, F. H., Adams, F. C., & Lizano, S. 1987, "Star formation in molecular clouds - Observation and theory," *ARA&A*, **25**, 23.

Siringo, G., Kreysa, E., Reichertz, L. A., & Menten, K. M. 2004, "A new polarimeter for (sub)millimeter bolometer arrays," *A&A*, **422**, 751.

Spitzer, L. 1978, *Physical Processes in the Interstellar Medium*, John Wiley and Sons.

Stahler, S. W. 1991, "The early life of stars," *Scientific American*, **265**, 48.

eds. Stahler, S. W. & Palla, F. 2004, *The Formation of Stars*, Wiley-VCH, first edition.

Tamura, M., Hough, J. H., Greaves, J. S., Morino, J.-I., Chrysostomou, A., Holland, W. S., & Momose, M. 1999, "First Detection of Submillimeter Polarization from T Tauri Stars," *ApJ*, **525**, 832.

Tamura, M., Hough, J. H., & Hayashi, S. S. 1995, "1 Millimeter Polarimetry of Young Stellar Objects: Low-Mass Protostars and T Tauri Stars," *ApJ*, **448**, 346.

Testi, L., Bacciotti, F., Sargent, A. I., Ray, T. P., & Eislöffel, J. 2002, "The kinematic relationship between disk and jet in the DG Tauri system," *A&A*, **394**, L31.

Thommes, E. W., Duncan, M. J., & Levison, H. F. 2003, "Oligarchic growth of giant planets," *Icarus*, **161**, 431.

van de Hulst, H. C. 1957, *Light Scattering by Small Particles*, John Wiley and Sons.

Voellmer, G. M., Chuss, D. T., Jackson, M., Krejny, M., Moseley, S. H., Novak, G., & Wollack, E. J. 2006, "A kinematic flexure-based mechanism for precise parallel motion for the Hertz variable-delay polarization modulator (VPM)," in *Optomechanical Technologies for Astronomy. Edited by Atad-Ettedgui, Eli; Antebi, Joseph; Lemke, Dietrich. Proceedings of the SPIE, Volume 6273, pp. 62733P (2006).*, volume 6273 of *Presented at the Society of Photo-Optical Instrumentation Engineers (SPIE) Conference*.

Weidenschilling, S. J. 1977, "The distribution of mass in the planetary system and solar nebula," *Ap&SS*, **51**, 153.

Wetherill, G. W. & Stewart, G. R. 1989, "Accumulation of a swarm of small planetesimals," *Icarus*, **77**, 330.

Yamashita, T., Sato, S., Nagata, T., Gatley, I., Hayashi, S. S., & Fukui, Y. 1989, "Infrared reflection nebulae around GL 490 and R Monocerotis - Shell structure and possible large dust grains," *ApJ*, **336**, 832.

Youdin, A. N. & Shu, F. H. 2002, "Planetesimal Formation by Gravitational Instability," *ApJ*, **580**, 494.